EXPERIMENTAL AND NUMERICAL STUDIES OF AEROSOL PENETRATION THROUGH SCREENS

A Dissertation

by

TAE WON HAN

Submitted to the Office of Graduate Studies of
Texas A&M University
in partial fulfillment of the requirements for the degree of

DOCTOR OF PHILOSOPHY

May 2007

Major Subject: Mechanical Engineering

EXPERIMENTAL AND NUMERICAL STUDIES OF AEROSOL PENETRATION THROUGH SCREENS

A Thesis

by

TAE WON HAN

Submitted to the Office of Graduate Studies of
Texas A&M University
in partial fulfillment of the requirements for the degree of

DOCTOR OF PHILOSOPHY

Approved by:

Chair of Committee,	Andrew R. McFarland
Committee Members,	John S. Haglund
	Sridhar Hari
	Yassin A. Hassan
Head of Department,	Dennis L. O'Neal

May 2007

Major Subject: Mechanical Engineering

ABSTRACT

Experimental and Numerical Studies of
Aerosol Penetration through Screens. (May 2007)
Tae Won Han, B.S., M.S., Keimyung University, Korea;
M.S., Texas A&M University
Chair of Advisory Committee: Dr. Andrew R. McFarland

This research reports the results of experimental and numerical studies performed to characterize aerosol deposition on four different types of commercially available screens (electroformed-wire, woven-wire, welded-wire, and perforated-sheet) over a wide range of Stokes numbers (Stk ~ 0.08 to 20) and Reynolds numbers (Re_C ~ 0.5 to 575). The objective of the present research was to use the results of the study to develop models and data that will allow users to predict aerosol deposition on screens. Three-dimensional Computational Fluid Dynamics (CFD) simulations using Fluent (version 6.1.22), as a tool, were undertaken and thus validating the numerical technique and then the result has been compared with the experimental data. For each type of screen, results showed that beginning at critical value of Stokes number where efficiency increased gradually to its maximum value that was almost asymptotic to the areal solidity. It is shown that data obtained from experimental and numerical studies for one particular type of screen would collapse to a single curve if the collection efficiency is expressed in terms of non-dimensional parameters.

Correlations characterizing the aerosol deposition process on different types of screens were developed based on the above methodology. The utility of the developed procedure was demonstrated by considering an arbitrary test case, for a particular condition and reconstructing the efficiency curve for the test case. Further, results of the current study were compared with earlier researchers' models (Landahl and Hermann, 1949; Davies, 1952; Suneja and Lee, 1974; Schweers et al., 1994) developed for aerosol deposition on fibrous filters and discussed. These results suggest that the aerosol collection characteristic on different models is different and depends on the nature of the manufacturing process for a typical model (wire or fiber).

Finally, the pressure coefficient (Cp) for flow across the screen can be expressed as a function of the Reynolds number ($Re_{C,f}$) and the fraction of open area (f_{OA}). Correlations expressing the actual relationships were evolved. Additionally, a model was developed to relate pressure coefficient in terms of correction factor ($G_{f_{OA}}$) and Reynolds number.

DEDICATION

To my family

ACKNOWLEDGMENTS

My research is very much the product of a sustained collective endeavor and love. During my research over the part several years I have received enormous support and encouragement from the faculty, staff and fellow graduate students of Texas A&M University, the Mechanical Engineering Department's Aerosol Technology Laboratory. First of all, I would like to express my deepest gratitude to Dr. Andrew R. McFarland for his guidance, enthusiasm, and support throughout the course of this research. He is a great scientist, engineer, instructor and leader in aerosol science. I wish to thank him for all the opportunities he has made available to me in the pursuit of my Ph.D. degree and for always motivating me to perform my best.

I have also been blessed to benefit from the many fruitful discussions and suggestions from Dr. Sridhar Hari regarding this research. I would also like to extend my thanks to Dr. John S. Haglund. His engineering insight and intuition are truly remarkable. I am also grateful to Dr. Yassin A. Hassan who served as a member of my committee and provided comments and suggestions for improving this manuscript.

Special thanks and respect is extended to Mr. Carlos A. Ortiz in the Energy Systems Laboratory for his helpful, stimulating, and encouraging comments. I wish to thank Charlotte D. Sims for her editing skills. I would also like to thank my past advisors, Dr. Dennis O'Neal from Texas A&M University and Dr. Sung-Hoon Kim from Keimyung University in Korea, who provided me with tremendous encouragement for my life.

Many thanks to YoungJin Seo and other laboratory colleagues in the Mechanical Engineering Department for their help and encouragement. Additionally, I would like to

thank Mr. Nene for the detailed flow disturbance velocity and turbulent intensity measurements at various sampling locations presented in my study.

This thesis could not have been done without the sacrifices and support of my wife; Soo-Kyoung Bae. I am dedicating my small accomplishment to her, my daughter, my parents, and parents-in-law.

Finally, I thank Almighty God for all His blessings and presence in my life.

TABLE OF CONTENTS

Page

CHAPTER

CHAPTER Page

LIST OF FIGURES

FIGURE Page

FIGURE Page

FIGURE Page

FIGURE Page

LIST OF TABLES

TABLE Page

LIST OF SYMBOLS

a = Constant
A = Constant
AF = After-Filter
AD = Aerodynamic Diameter
ATL = Aerosol Technology Laboratory

b = Constant
B = Constant

c = Constant
C = Relative aerosol concentration
C_a = Cunningham's slip correction factor based on the aerodynamic diameter
C_{AF} = After filter concentration
C_c = Cunningham's slip correction
C_D = Particle drag coefficient
c_f = Concentration of fluorescein in filter or screen sample (fluorometer reading)
C_i = Reference concentration
C_o = Concentration after wall loss
C_p = Cunningham's slip correction factor based on the physical particle diameter
Cp = Pressure coefficient
C_{SM} = Screen relative concentration
C_1, C_2, C_3 = Constants
CFD = Computational Fluid Dynamics
CS = Center-to-Center Spacing
COV = Coefficient of Variation

d_a = Aerodynamic diameter
d_c = Characteristic length (fiber diameter or wire diameter or hole diameter)
d_{es} = Effective slack length
d_f = Fiber diameter
d_p = Particle diameter
d_m = Diameter of the droplets measured under the microscope
d_w = Wire diameter
d_h = Hole diameter

E = Total efficiency

f = Flattening factor to account for distortion of a droplet on a microscope slide
F_D = Drag force on the particle
f_{OA} = Fraction of the projected open area
Fr = Froude number

g or g_i = Gravitational acceleration
G = Dimensionless number that controls deposition due to gravitational settling

$G_{f_{OA}}$ = Correction factor
h = Height or height of channel
H = Correction factor

J = Diffusion flux

Ko = Darcy's constant
K or Ku = Kuwabara's hydrodynamic factor

L = Filter thickness in the direction normal to the flow
l = The length of all the fibers in the unit volume of the filter

M = Mesh size
m_f = Mass of fluorescein collected on the filter or screen

n = The number concentration of particles entering the element
n_o = Particle concentration upstream of the filter mat

OL = Opening length

P = Penetration
PISO = Pressure Implicit with Splitting of Operations
P_s = Static pressure

Q = Corrected volumetric air flow rate

R = Interception parameter (Ratio of particle diameter to fiber or wire diameter)
R_C = Concentric boundary of radius
R_f = Radius of a fiber
Re = Reynolds number
Re_C = Reynolds number based on the characteristic length (wire diameter or effective slack length) and the average velocity inside screen
$Re_{C,f}$ = Reynolds number based on the characteristic length and the face velocity
Re_f = Fiber Reynolds number based on the average velocity inside filter
Re_p = Particle Reynolds number
R^2 = R-sdquare, Sum Squared error
SM = Mesh-Screen
Stk = Stokes number or inertia parameter
Stk_c = Critical Stokes number
SIMPLE = Semi-Implicit Method for Pressure-Linked Equation
SIMPLEC = Semi-Implicit Method for Pressure-Linked Equation Consistent
SSE = Sum of square error

t = Time or sampling time
th = thickness

u or U_o = Face velocity, free stream velocity
U = Average velocity inside a filter or screen
u_i = Flow velocity in the i^{th} direction
u_j = Flow velocity in the j^{th} direction
u_u = Gas velocity
u_v = Particle velocity

V = Volume of solution used to elute the tracer
V_{TS} = Settling velocity of the particle

wd = Width
w_i = Uncertainty of X_i
w_{R_i} = Overall uncertainty of Y by all X_i
WL = Wall loss

X_i = Measured variables
x_i = Independent variables in the i^{th} direction
x_j = Independent variables in the j^{th} direction
x_v = Particle trajectory
x_0, x_1, x_2, x_3 = Constants

Y = Result

z_0, z_1, z_2, z_3, z_4, z_5, z_6 = Constants

α = Solidity or packing density
α_A = Area solidity

δ = Variation

η = Single fiber efficiency
η_A = Actual efficiency
η_I = Single fiber efficiency due to impaction
η_{IR} = The combined single fiber efficiency due to interception and impaction
η_{SS} = Standardized screen efficiency
$\eta_{SS,corr}$ = Standardized screen efficiency of final correlation
$\eta_{SS,i}$ = Standardized screen efficiency for each screen
η_R = Single fiber efficiency due to interception

θ = Angle of staggered type perforated-sheet

ρ = Gas density
ρ_a = Air density
ρ_p = Droplet density
ρ_w = Density of water

λ = Mean free path

μ = air viscosity

CHAPTER I

INTRODUCTION

Background

Aerosol measurement frequently requires that a sample be conveyed to a diagnostic device or collection system. For accurate measurements, a representative aerosol sample must be drawn through an inlet into the particle measuring or collecting device (Figure 1.1). However, the air sample aspirated into the inlet may be contaminated with unwanted large-sized debris such as insects, plant debris, and fibers. Such contaminants are usually removed by a screen placed downstream of the inlet aspiration region. An effective screen is one that filters the contaminant while allowing aerosol particles of interest to penetrate with minimum deposition.

Figure 1.1. Representative inlet samplers with screen.

This dissertation follows the style and format of *Journal of Aerosol Science*.

There are several types of commercially available screens that can be classified based on the fabrication methods and configuration, e.g., electroformed-wire, woven-wire, welded-wire, perforated-sheet, etc. (Table 1.1). Wire screens are extensively used in an incredibly wide variety of industries. Its presence is rarely detected as, more often than not, it is incorporated as a filter or screening medium within a finished product or piece of equipment. It is used in typical process plants for size classification, product separation, impurity removal, particle filtration, and mist elimination (Capps, 1994). Woven-wire and welded-wire screens are the most widely used configurations for commercial sorting, screening, and filtering applications. Electroformed-wires are used increasingly for small-scale production of specialty materials and precision quality control. Perforated metal sheets have been used for a variety of other applications such as sorting, separating, machine guards, ventilating grills, and fabricating custom parts.

Woven-wire screens can be further classified into different grades such as standard filter, milling, bolting, strainer, etc. The typical mesh screen is made of wires of a particular diameter interwoven together to form a perforated planar structure with desirable mesh openings (shape and size). Depending on the intended application, the wire size and mesh openings of a screen may vary from a few tens of micrometers to millimeters. The woven structure of the wire screen may be soft and flexible or as rigid and durable as a solid steel plate (Soar, 1991). Among woven-wire cloths, bolting grade has the smallest wire diameter and highest percentage of open area, which suggests that it should find application in air sampling for blocking the passage of insects while minimizing loss of particles that are to be sampled.

Table 1.1. General information of wire and perforated-sheet screens.

Type	Percentage of Open Area Range	Wire Diameter Range Inch (Micrometers)	Thickness Inch (Micrometers)	Material Type	Grade*	Pattern Opening
Electroformed Wire Cloth	36.0-98.0	0.0002 - 0.0067 (5 - 170)	N/A	Copper, Gold, Nickel	N/A	N/A
Woven wire cloth	11.7-85.7	0.00079-0.375 (20 - 9525)	N/A	Aluminum, Brass, Bronze, Copper, Nickel, Silver, Steel Stainless, Steel, Titanium	Standard, Bolting, Milling, Filter, Space Cloth, Strainer	N/A
Welded Wire Cloth	73.6-87.8	0.017 - 0.106 (432 - 2692)	N/A	Stainless Steel, Steel	N/A	N/A
Round Hole Perforated Sheet	10.0-63.0	N/A	0.006 - 0.25 (152 - 6350)	Aluminum, Brass, Plastic, Stainless Steel, Steel	N/A	Staggered, Straight

*Standard: Most commonly used grade. Ideal for liquid particle separation, gravel sizing, support screens, basket liners.
Bolting: Smaller wire diameter and higher percentage of open area than milling and standard grade. Use for accurate wet and dry sifting and separating.
Milling: Smaller wire diameter and higher percentage of open area than standard grade. More durable in processing and sifting applications than standard and bolting grade cloths.
Filter: Tightly woven-wires for very durable, strong mesh. Use for accurate filtration at high pressure and flow rates.
Space cloth: Woven from large wire diameters with large, square openings.
Strainer: Very fine wire diameter and small mesh size. Good for straining liquids and grading powders.

Owing to its great practical importance, the penetration of aerosol particles through fibrous filters has been widely studied from both the theoretical and experimental points of view (Fuchs, 1964; Happel, 1959; Kuwabara, 1959; Landahl and Herrman, 1949; Langmuir, 1942; Lee and Liu, 1982; Liu and Pui, 1975; Stechkina and Fuchs, 1966; Stechkina et al., 1969; Suneja and Lee, 1974; Torgeson, 1964). However, for screens, aerosol penetration studies have been largely confined to the nanoparticles regime with emphasis on the size separation of these particles using diffusion batteries that consist of a series of screens (Scheibel and Porstendorfer, 1984; Cheng et al., 1990; Alonso et al., 2001). Cheng (1993) studied the operating principle, theory, design and applications, and data analysis of the diffusion batteries.

Collection of uncharged particles by screens is influenced by different particle deposition mechanisms such as Brownian motion, interception, and inertial impaction. For a particular screen configuration, flow conditions and particle sizes determine the mechanisms that govern deposition. The penetration process is strongly influenced by the mesh size, flow field, and Stokes number (the ratio of the stopping distance of a particle to a characteristic dimension of the obstacle). A detailed discussion on the deposition mechanisms for aerosol particles on screen media will be presented later.

Objectives of the Present Study

The principal objective of the present research was to study aerosol deposition on different types of screens (electroformed-wire, woven-wire, welded-wire, and perforated-sheet screens) using both experimental and numerical techniques, as a means of developing models and data that will allow users to predict aerosol deposition on screens.

The experimental investigation involved measurements of aerosol losses for different screen designs and operational conditions. Tests were carried out for screens in the flow regime (1< Re_C <500). Three-dimensional Computational Fluid Dynamics (CFD) simulations of the experiments were undertaken simultaneously to validate the numerical approach against experimental data. An additional goal is to develop empirical correlations summarizing the deposition process on screens and a new parameter that consolidates aerosol deposition data on screens. The following steps were taken to fulfill the goals of this project.

Electroformed-Wire Screen was used as a reference screen in the present study. The primary reason that an electroformed-wire was selected to study aerosol deposition as a reference wire screen was the fact that openings of precision electroformed-wires are consistently accurate, in contrast to ordinary wire screens. An experimental technique for measuring the collection efficiencies (actual efficiency, η_A) and pressure drop through the screen was developed. A three-dimensional numerical study was performed using commercial software (Fluent) with electroformed-wire cloth. The numerical results were compared with the experimental results. An empirical correlation for the actual efficiency (η_A), as a function of the non-dimension parameters (Stokes number and area solidity), was then obtained using a multi-variable regression technique. Further, as there is well-established correlation between the collection efficiency and the non-dimensional parameters (interception parameter, Reynolds number, and Stokes number) for the fibrous filtration process, a similar approach was attempted in the process of standardizing the collection efficiency data on the screens. A model was developed that will allow users to predict, on an *a priori* basis, the deposition of aerosol on screens. The entire study can be divided into two primary components: the experimental study and the numerical study. Both aspects of the study are described in more detail in the following sections.

Layout and Key Points in Each Chapter

The study reported in this thesis involved a series of different procedures. These procedures include (a) A review of the previous studies of filtration with fibrous filters, (b) objective and description of screens, (c) the development of experimental methods, (d) the conduction of a series of experiments, (e) the development of numerical models, and (f) development of empirical correlation using a multi-variable regression technique.

Chapter II begins with a description of the review of the previous studies on aerosol filtration with fibrous filters. Theoretical concepts pertaining to the aerosol filtrations process are briefly reviewed. A basic introduction of the single fiber concept is provided. Important deposition mechanisms that influence the transport and deposition of aerosol particles are outlined. Concepts related to flow and pressure drop across the filter are provided. Contributions of previous researchers on the filtration process are summarized.

In Chapter III, a brief description of the different commercially available screen types are presented and illustrated with sample photographs. Important geometrical features that characterize each type of screen are outlined. Technical terminology that is adopted to specify screen characteristics are introduced and are described in detail.

In Chapter IV, various components of the experimental setup used in the aerosol deposition studies are described in detail. A brief outline of the experimental methodology adopted in the process of conducting tests with liquid aerosols is presented. Various other issues that are important from the experimental viewpoint in the process of conducting the studies are introduced and discussed. Finally, details of the experiments performed on different screen types are provided.

In Chapter V, numerical methodology adopted in the current study is outlined. Concepts that form the theoretical basis of the numerical approach are briefly presented. Efforts undertaken to arrive at the appropriate model for the numerical studies are delineated and the findings are reported. The numerical approach is validated by providing a comparison of the simulation predictions to experimental data for two different electroformed wire screens. Further, mention is made of the various simulations performed on the different screen types.

As a next step, in Chapter VI, simulation predictions for the different screen types are compared to the corresponding experimental results. This is followed by the development of empirical correlation equations describing results for each screen type, utilizing a multi-variable regression technique that enables the user to characterize actual efficiency using mathematical equations. Details on the development of a methodology to standardize experimental and numerical results on each screen type are presented. Finally, non-dimensional groups that influence the screen performance are identified and correlations expressing the standardized performance as a function of the non-dimensional groups are evolved.

Chapter VII summarizes the conclusions of the present work and presents a series of recommendations for future studies. There is a good chance that this work will benefit screen applications and provide users with a better understanding the deposition process with liquid aerosols. Results of this work may also be used to help individuals in selecting the appropriate type of screens to remove larger debris while collecting liquid aerosols with minimum losses.

CHAPTER II

THEORETICAL BACKGROUND

Three elements are fundamental in the filtration process are the dispersed aerosol, the transport medium (usually air), and the porous media, filter or screen. Each of these elements plays an important role in determining the collection efficiency and pressure drop. The first step in the process of formulating a quantitative basis for the filtration phenomenon is an understanding of the flow field and the associated particle behavior at the single element level. In the case of a fibrous filter, the medium may ideally be assumed to be composed of a number of cylindrical elements in series and parallel combinations. Different filter models have been proposed and the flow field corresponding to each model has been determined. The most important and frequently used models are an isolated cylinder model (Lamb, 1932), a cell model (Kuwabara, 1959; Happel, 1959), a fan model (Kirsch and Fuchs, 1968), and a staggered-array-model (Yeh, 1972).

Description of the Filter Models for the Flow Field

The Lamb equation which is frequently used to describe the flow field around an isolated cylinder has an approximate solution to the Navier-Stokes equation. The isolated cylinder model ignored the effects of neighboring fibers and packing density, therefore this model does not represent a realistic flow condition around a cylindrical fiber;

nevertheless, Lamb's theory is accurate at low Reynolds numbers (*Re*, a dimensionless number that characterizes fluid flow around an obstacle such as a filter).

The cell model derived by Kuwabara (1959) and Happel (1959) considers the effect of the neighboring fibers and fiber packing density. This model is based on a firm theoretical basis and approximates the true flow field in a real filter better than the other models. The model consists of a fiber of radius (R_f) surrounded by a concentric boundary of radius (R_C) with a packing density, α, that is equal to the ratio of R_f^2/R_C^2. A zero gradient of the circumferential velocity was assumed by Happel on the outer boundary of the cell, whereas, zero vorticity was assumed by Kuwabara. The solution of the Kuwabara model was obtained based on the assumption that the inertia force term in Navier-Stokes equations is negligible. Therefore, the solution of this model which was obtained by ignoring the inertia term in Navier-Stokes equations is valid for creep flow only.

The fan model which is derived by Kirsch and Fuchs (1968) consists of a series of layers of equidistant, parallel fibers, which is not so in real filters. To account for this feature, they introduced an inhomogeneity factor in their model. At the end of the 1960's, Fuchs and his co-workers had the conclusion that it is possible to calculate the resistance and efficiency with sufficient accuracy for practical purposes, if the geometric parameters (fiber radius, solidity, and filter thickness) are known.

Yeh (1972) selected the staggered-array model which is an approximation of the fiber structure in a real filter. Fibers in a filter were distributed as a staggered array of infinitely long parallel cylinders perpendicular to the flow. There is an implicit assumption that the flow fields around each cylinder are similar (like a periodic boundary condition). Therefore, only the flow field in the region within a rectangular shaped parallel channel is considered. More importantly, the flow field obtained by solving the complete form of the Navier-Stokes equations in this model is valid for higher Reynolds number flows.

In the case of wire screens, few investigators only modeled the pressure drop and fluid flow through a wire screen regenerator. Cheng et al. (1985) measured the pressure drop across layers of screens, estimated the single-fiber collection efficiency of screens and compared his results to the theoretical prediction obtained from fan model filtration.

Yarbrough et al. (2004) investigated three types of models under steady and oscillating flow conditions; a three-dimensional model of plain woven wire screens, a two-dimensional staggered tube bank model, and a porous media regenerator model were built. Their goal was to determine the best model for a wire screen regenerator using the CFD approach. The plain square weave wire screen model was created initially with one layer of screen. However, two and three screen models were made (as the copy of the first screen and positioned behind) since regenerators contain hundreds of screens. Their results showed that the most realistic model among three different models is the wire screen model, but it has some requirements (computational size and requirements) for numerical simulations. The other two models (two-dimensional staggered tube bank model and porous media model) have to be considered as simplified regenerator models. The porous media model is the most promising model for simulations, and would also be the easiest to incorporate into a system level model. However, it does not represent the flow behavior well.

Single Fiber Efficiency Concept

The starting point in studying aerosol penetration through screens is to consider the capture of particles by a single element of an electroformed-wire, woven-wire, welded-wire, or perforated-sheet. The classical filtration theory only dealt with isolated fiber, but the modern filtration theory, single fiber theory, takes into account in the effects of neighboring fibers. The Reynolds number, Re_f that characterizes the flow around a fiber having a diameter, d_f, was defined as

$$Re_f = \frac{\rho_a U d_f}{\mu} \tag{2-1}$$

Where ρ_a is air density; U is the average velocity inside a filter, $U_o/(1-\alpha)$; d_f is the fiber diameter; μ is air viscosity. U_o is called the face velocity, just before the air enters inside a filter. Let α be the solidity or packing density, i.e., volume fraction of the fibers in the filter, and l be the length of all the fibers in the unit volume of the filter.

The single fiber efficiency, η, is defined as the ratio of the number of particles striking the fiber to the number which would strike if the streamlines were not diverted around the fiber.

The total efficiency, E, of a filter composed of many such individual fibers in a mat can be related to the single fiber efficiency, η. The solidity and the total efficiency can be written as

$$\alpha = \frac{\pi d_f^{\,2}}{4} l \tag{2-2}$$

$$E = 1 - \frac{n}{n_O} = 1 - \exp\left[\frac{-4\eta\alpha L}{\pi(1-\alpha)d_f}\right] \tag{2-3}$$

Where n is the number concentration of particles entering the element; n_o is the particle concentration upstream of the filter mat; L is the filter thickness in the direction normal to the flow, and d_f is the fiber diameter.

The advantage of using the single fiber efficiency is that it is independent of the filter thickness, L. This is an important point to consider in comparing filters, because a filter with lower single fiber efficiency can be made to have a higher total efficiency by simply using more material in the mat.

In real filters, not all of the fibers are placed transverse to the flow. Some fibers are clumped together, resulting in non-uniform distribution in the filter that will usually result in a reduced efficiency. In considering the performance of real filters, it is necessary to take this into account.

Capture Mechanisms

As air flows around a wire, trajectories of particles may deviate from the streamlines due to several mechanisms. As a result, particles may collide with the fibers or wires and deposit on them. The important deposition mechanisms for particles in the size range of interest (2 to 20 µm AD) are inertial impaction, interception, and gravitational settling (Hinds, 1998). Other mechanisms such as electrostatic and diffusion were ignored in this study because diffusion is only dominated for particle below submicron size range and the electrostatic effects are pre-eliminated before test.

Even if the trajectory of a particle does not depart from the original streamline, a particle may still be collected if the streamline brings the particle center to within one particle radius from the fiber surface, which is called the interception effect. One would expect the interception to be relatively independent of flow velocity for a given filter (Figure 2.1), which can be contrasted to the flow dependent characteristics of diffusion and inertial impaction. The dimensionless parameter describing the interception effect is the interception parameter (R), defined as the ratio of particle diameter to fiber or wire diameter.

Fluid streamlines around a cylinder are curved. Particles with a finite mass moving with the flow may deviate from streamlines due to their inertia (Figure 2.1). If the curvature of a streamline is sufficiently large and the mass of a particle sufficiently high, the particle may deviate far enough to collide with the cylinder. The importance of this inertial impaction mechanism increases with increasing particle size and increasing air velocity. This is contrary to that for diffusion, where both smaller size and lower velocity increase the opportunity of collision of particles with cylinders. By the Stokes number, the mechanism of inertial impaction is defined as:

$$Stk = \frac{C_c \rho_p d_p^{\,2} U_o}{18 \mu d_c} \tag{2-4}$$

Where C_c is Cunningham's slip correction; ρ_p is the particle density; d_p is the particle diameter; U_o is the face velocity; μ is the gas viscosity; and d_c is the characteristic length (fiber diameter, wire diameter or slack width). The Stokes number is the basic parameter describing the inertial impaction mechanism for particle collection in a filter or a wire. A large Stokes number implies a high probability of collection by impaction, whereas a small Stokes number indicates a low probability of collection by impaction.

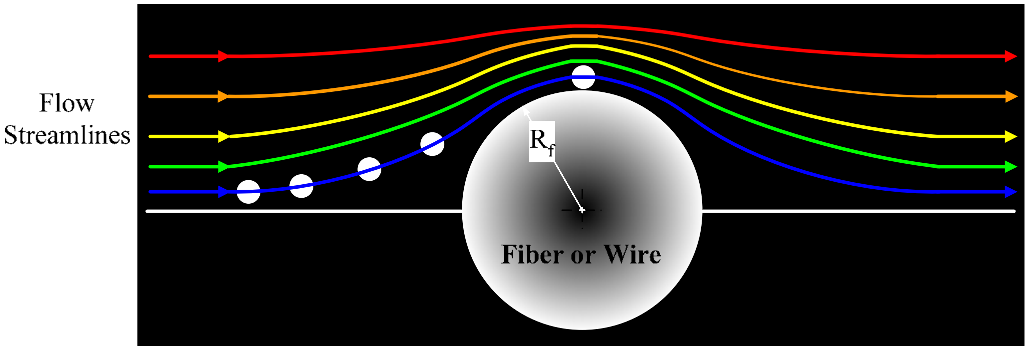

(a) Interception

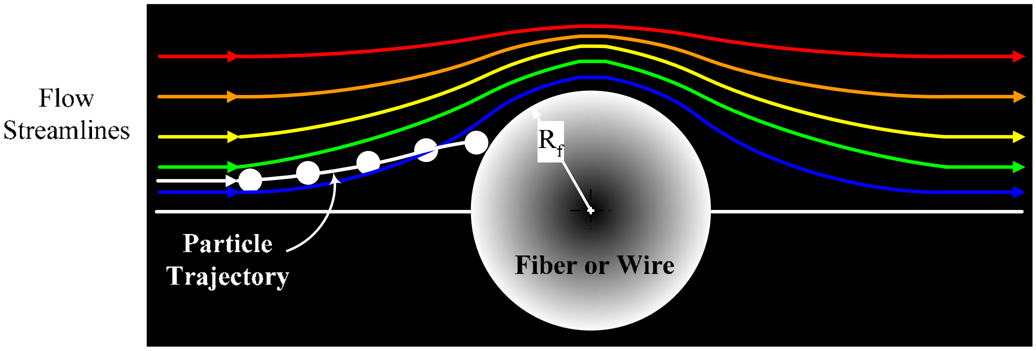

(b) Impaction

Figure 2.1. Illustration of particle collection by a single fiber or wire through the interception and impaction mechanisms.

With a finite velocity, particles will settle with a finite velocity in a gravitational force field. When the settling velocity is large enough, particles may deviate from the streamline. This mechanism is typically important for particles larger than at least a few micrometers in diameter and at low velocities. The dimensionless number that controls deposition due to gravitational settling is the parameter *G*.

$$G = \frac{V_{TS}}{U_o} = \frac{\rho_p {d_p}^2 C_c g}{18 \mu U_o} \tag{2-5}$$

Where U_o is the face velocity; V_{TS} is the settling velocity of the particle; and, g is the gravitational acceleration. Generally, effect of gravitational settling is small compared to other mechanisms considered in this study; unless the particle size is large and the face velocity is low, this mechanism should be unimportant.

In some filtration theories, it is assumed that the individual filtration mechanisms discussed above are independent of each other and additive. Therefore, η, the overall single fiber collection efficiency in Equation 2-2, can be written as the sum of individual single filter efficiencies contributed by the different mechanisms. This approximation has been found to serve adequately for predicting the overall collection efficiencies, owing to the different ranges in particle sizes and face velocities in which different filtration mechanisms predominate (Hinds, 1998). Some theories combine interception with diffusion or inertial impaction to provide more realistic models. Sometimes a small correction term is included to take into account the combined effect. Additionally, the wake region behind the wires could introduce some minor collection. The amount collected is dependent on the Reynolds number.

In this research, aerosol deposition on the screen was not represented as being caused by a combination of the individual efficiencies (as in the single fiber concept), but the overall efficiency value was estimated.

Summary of Earlier Researchers' Results

Theoretical and numerical results are summarized in Tables 2.1 to 2.3. The first systematic study of aerosol filtration, by mats of cylindrical fibers, was made by

Table 2.1. Single fiber efficiency due to interception mechanism.

Investigator	Equation for Interception, η_R	Remarks
Langmuir (1942)	$\eta_R = \frac{1}{2(2-\ln(Re))}\left[2(1+R)\ln(1+R)-(1+R)+\frac{1}{(1+R)}\right]$	Lamb's Flow (1932)
Friedlander (1957)	$\eta_R = \frac{1.25R^{1.82}}{2K_O}$ where $K_O = 2.0022 - \ln Re$	Tomotika & Aoi Flow (1951)
Kuwabara (1959)	$\eta_R = \frac{(1+R)}{2K}\left[2\ln(1+R)-1+\alpha+(\frac{1}{1+R})^2(1-\frac{\alpha}{2})-\frac{\alpha}{2}(1+R)^2\right]$ where $K = -\frac{1}{2}\ln\alpha+\alpha-\frac{1}{4}\alpha^2-\frac{3}{4}$	
Natanson (1962)	$\eta_R = \frac{1}{K_O}R^2$ where $K_O = 2.0022 - \ln Re$	Lamb's flow for R<<1
Torgeson (1964)	$\eta_R = 0.0518\frac{4\pi}{2-\ln Re}R^{\frac{3}{2}}$	Lamb's Flow
Fuchs (1964)	$\eta_R = 1+R-\frac{1}{(1+R)}$	Potential Flow
Stechkina and Fuchs (1966)	$\eta_R = \frac{(1+\alpha)}{2K}\left[2\ln(1+R)-1+\frac{1}{(1+R)^2}\right]$	
Lee and Ramamurthi (1993)	$\eta_R = \frac{(1-\alpha)}{K}\frac{R^2}{(1+R)}$	for $0.005<\alpha<0.2$

Table 2.2. Single fiber efficiency due to inertial impaction mechanism.

Investigator	Equation for Inertial Impaction, η_I	Remarks
Landahl & Herrmann (1949)	$\eta_I = \frac{Stk^3}{Stk^3 + 0.77Stk^2 + 0.22}$	$Re=10$
Yeh and Liu (1974a)	$\eta_I = \frac{(Stk)J}{(2K)^2}$ $J = (29.6 - 28\alpha^{0.62})R^2 - 27.5R^{2.8}$ for $R<0.4$ $J = 2.0$ for $R>0.4$ $K = -\frac{1}{2}\ln\alpha + \alpha - \frac{3}{4} - \frac{1}{4}\alpha^2$	for $0.005<\alpha<0.2$, $0.1<d_f<50\mu m$ and $Re<1$
Schweers et al. (1994)	$\eta_I = \left(\frac{Stk}{Stk + 0.8} - \frac{2.56 - Log(Re) - 3.2R}{10\sqrt{Stk}}\right)(1+R)$	for $1<Re<60$

Table 2.3. Single fiber efficiency due to interception plus inertial impaction mechanisms.

Investigator	Equation for Interception Plus Inertial Impaction, η_{IR}	Remarks
Davies (1952)	$\eta_{IR}=0.16\left[R+(0.5+0.8R)Stk-0.1052RStk^2\right]$	for *Re*=0.2
Torgeson (1964)	$\eta_{IR}=\eta_R\left[1+R^{-\frac{3}{2}}Stk(0.5+0.8R)\right]$	Where η_R from Table 2
Stechkina et al. (1969)	$\eta_{IR}=\eta_R+\eta_I$ where $\eta_I=\dfrac{J\cdot Stk}{(2K)^2}$ $\eta_R=\dfrac{1}{2K}\left[2(1+R)\ln(1+R)-(1+R)+\dfrac{1}{(1+R)}\right]$ $J=(29.6-28\alpha^{0.62})R^2-27.5R^{2.8}$ $K=-\dfrac{1}{2}\ln\alpha+\alpha-\dfrac{1}{4}\alpha^2-\dfrac{3}{4}$	For *Stk*<<1
Suneja and Lee (1974)	$\eta_{IR}=\dfrac{1}{\left[1+\dfrac{1.53-0.23\ln\mathrm{Re}+0.0167(\ln\mathrm{Re})^2}{Stk}\right]^2}+\dfrac{2R}{3Stk}$	for *Re*<500

Langmuir (1942). Landahl and Herrmann (1949) employed the flow field in calculating the inertial impaction efficiency and gave an equation for $Re = 10$. Davies (1952) was the first to calculate the filtration efficiency due to interception and inertial impaction by the use of viscous flow. His calculation was presented in a graphical form for $Re = 0.2$ and the equation has been found to fit his results. Improved theories have been developed using more reliable and exact flow fields. Friedlander (1957), Kuwabara (1959), Natanson (1962), Fuchs (1964), Stechkina and Fuchs (1966), and Lee and Ramamurthi (1993) calculated the efficiency due to interception. Torgeson (1964) combined the filtration efficiencies due to interception and inertial impaction. In addition to the above investigations, the studies of Lee and Liu (1982), Liu and Pui (1975), Suneja and Lee (1974), Yeh and Liu (1974a and 1974b), and Schweers et al. (1994) consider efficiency due to inertial impaction.

Compared to the above literature on aerosol deposition on fibrous filters, aerosol penetration studies on screens have been largely confined to the nanoparticle regime with emphasis on size separation of these particles using diffusion batteries that consist of a series of screens (Scheibel and Porstendorfer, 1984; Cheng and Yeh, 1980; Alonso et al., 2001). Alonso et al. (2001) presents experimental results of aerosol penetration through a wire screen for mobility equivalent particle diameters between 2 and 10 nm. His experimental investigation on the relationship between single fiber efficiency for diffusional deposition and the Peclet number was carried out for a relatively wide range of Reynolds numbers and an empirical equation was obtained. There is little information available on the penetration of aerosol particles in the size range of interest for sampling inlets, which is generally comprised of sizes less than about 20 μm Aerodynamic

Diameter (AD). Studies of aerosol deposition on different types of screens are quite rare and have not been characterized in detail.

Pressure Drop Across Screens

Prediction of pressure drop is an important part of a filtration study for the simple reason that the measured pressure drop value can be used to validate the accuracy of the flow field calculations that are subsequently used for the determination of the aerosol collection efficiency. In other words, once a flow field is solved numerically, the corresponding pressure drop can be calculated and compared with the actual measurements.

Fluid flow in filters is usually viscous at low velocity; therefore, the pressure drop across the filter is approximately proportional to the flow rate. Darcy (1856) first described this in his book on water flow through a porous medium. He provided Darcy's Law, which is valid only for small Reynolds numbers and for cases where the inertia term in the Navier-Stokes equation is unimportant. As the velocity increases, the inertia term in the Navier-Stokes equation is no longer negligible and begins to affect the flow field. According to Davies (1973), the upper limit for the viscous flow regime occurs at a Reynolds number of about 0.05 and the inertia is important in the region $0.05 < Re < 20$.

Langmuir's expression for pressure drop is based on a model in which evenly spaced cylinders are located with their axes parallel to the flow direction (Langmuir, 1942). He stated that the resistance of the filter would be increased by a factor of 1.4 compared to that given by the equation when the cylinders are arranged across the flow direction. Iberall (1950) took into account the random orientation of the fibers by assuming an equal distribution of fibers in three perpendicular directions. Davies (1952), using dimensional analysis, correlated his theoretical results with pressure drop data for a large number of filter media.

There have been studies of the flow through screens, though a considerable amount of work has been done on the flow of gases and this has been reviewed by Laws and Livesay (1978). Weighardt (1953) investigated liquid flow and proposed an empirical correlation for pressure drop as a function of wire diameter, flow rate, and physical properties of the liquid. Ehrhardt (1983) has extended the work and covered a wider range of conditions ($0.5 \leq Re_C \leq 1000$). Several works have been published about the porosity and pressure drop at steady flow conditions for wire-mesh woven screens. Armour and Cannon (1968) investigated several types of screens through experiments made in a bed with a single screen layer. Correlations to evaluate the porosity, based on the geometry of the screen, were also proposed. Chang (1990) demonstrated the importance of the inclusion of the actual thickness of the wire screen for an accurate estimate. Simon and Seume (1988) provide a further review of friction factor correlations for steady flow and also presented the compressibility effects and the oscillating characteristics of the flow. Wakeland and Keolian (2003) presented measurements of the resistance to oscillating flow for $0.002 \leq Re_{C,f} \leq 400$ of individual woven-wire screens.

CHAPTER III

DESCRIPTION OF SCREENS

The geometry of screens generally varies based on the relative dimensions of the elements. The most common type is the plain weave type of wires evenly spaced in both directions. Another simple type in frequent use is represented by the perforated-sheet. The relative scale of any type is best described by the fraction of open area, the fractional degree of which the screen obstructs the flow. The range of the fraction of open area is from zero for no screen to unity for a solid plate. The full range is important, although the two limits have no practical significance. We refer to each screen by its nominal size in both units (inch and μm). Tested screen dimensions are found in Table 3.1.

Wire Screen

A plain weave type of wire screen (electroformed-wire, woven-wire, and welded-wire) was chosen for this study (Figures 3.1 to 3.3). The important screen parameters are the fraction of open area (f_{OA}), characteristic length (d_w), and mesh size (M). The term mesh refers to the number of openings per unit length. The distance is the length between the two centers of the adjacent parallel wires, which is simply the inverse of the mesh number. The clear width of the mesh opening is the distance minus the diameter of the wire. We calculate the fraction of open area ($f_{O\mathrm{A}}$) of a screen by computing the fraction of

Table 3.1. Specification of screens tested for this study.

	Screen Type	**Grade**	**Opening Pattern**	**Characteristic Length (*dw* or *d_h*)**		**Fraction of Open Area (f_{OA})**	**Mesh Size**	**CS†**		**Thickness (*th*)**		**OL‡**	
				inch	µm	%		inch	µm	inch	µm	inch	µm
1	Electroformed	N/A	N/A	0.00629	160	56.0	40	N/A		N/A		0.01871	475
2	Electroformed	N/A	N/A	0.00268	68	75.0	50	N/A		N/A		0.01732	440
3	Electroformed	N/A	N/A	0.00138	35	88.0	45	N/A		N/A		0.02080	528
4	Electroformed	N/A	N/A	0.00257	65	90.0	20	N/A		N/A		0.04740	1204
1	Woven	Standard	N/A	0.01700	432	43.6	20	N/A		N/A		0.03300	838
2	Woven	Bolting	N/A	0.00450	114	50.7	64	N/A		N/A		0.01110	282
3	Woven	Standard	N/A	0.01800	457	50.7	16	N/A		N/A		0.04450	1130
4	Woven	Milling	N/A	0.00950	241	51.1	30	N/A		N/A		0.02380	605
5	Woven	Milling	N/A	0.01600	406	55.4	16	N/A		N/A		0.04650	1181
6	Woven	Milling	N/A	0.01700	432	58.1	14	N/A		N/A		0.05440	1382
7	Woven	Bolting	N/A	0.00950	241	71.9	16	N/A		N/A		0.05300	1346
1	Welded	N/A	N/A	0.01700	432	74.6	8	N/A		N/A		0.10800	2743
1	Perforated	N/A	Staggered	0.01500	381	21.0	N/A	0.0310	787	0.014	356	N/A	N/A
2	Perforated	N/A	Staggered	0.18750	4763	51.0	N/A	0.2500	6350	0.060	1524	N/A	N/A

†CS: Center-to-Center Spacing

‡OL: Opening Length

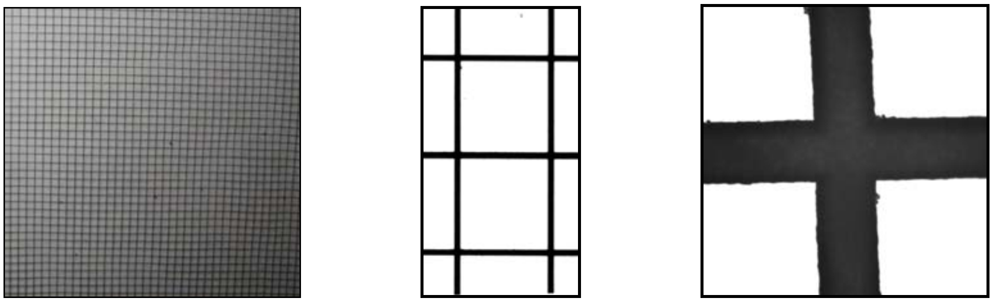

Photo (40× magnification) (400× magnification)

Photomicrographs

(a) 45×45, 0.00138-inch, 0.88

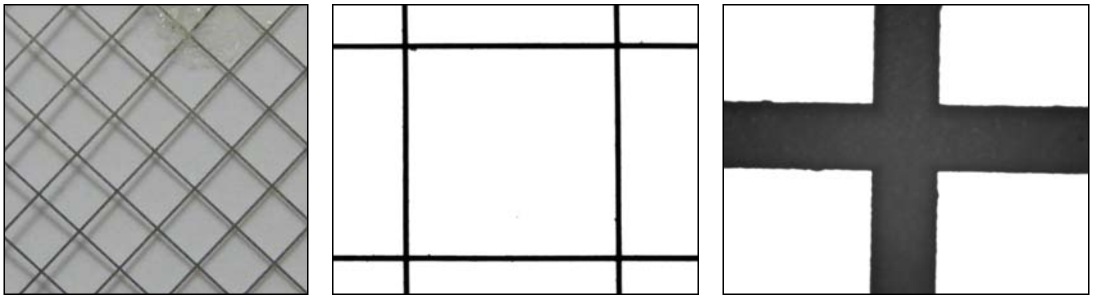

Photo (40× magnification) (400× magnification)

Photomicrographs

(b) 20×20, 0.002565-inch, 0.90

Figure 3.1. Electroformed-wire screen tested. Parameters in each figure are mesh size (M), wire diameter (d_w) and fraction of open area (f_{OA}).

the projected open screen area, instead of the volume fraction of the actual cylinder-shaped wire, as would be the case for a fibrous filter (Figure 3.4). The equation for f_{OA} can be expressed in this form for each screen,

$$f_{OA} = (1 - d_w \times Mesh)^2 \tag{3-1}$$

It must be noted that even though, in theory, wire screen configurations with a specific wire size and a mesh opening size could be made, not all of them are commercially available. For example, screens with small wire diameters and large mesh openings would have limited value in industrial applications. Therefore, for this study,

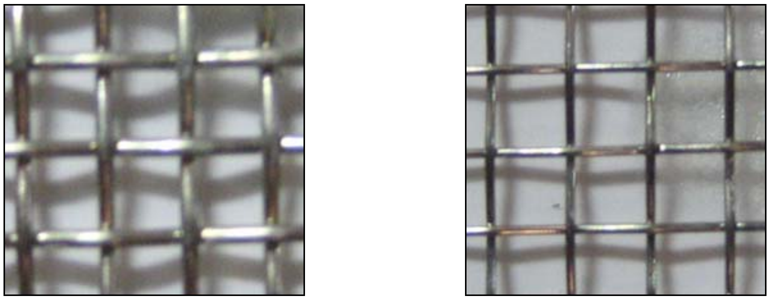

14×14, 0.017-inch, 0.581　　16×16, 0.0095-inch, 0.719

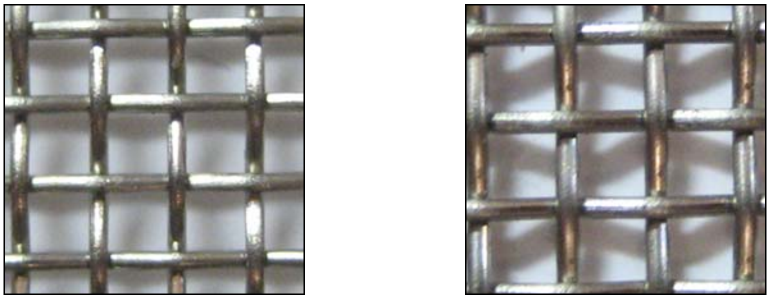

16×16, 0.016-inch, 0.554　　16×16, 0.018-inch, 0.507

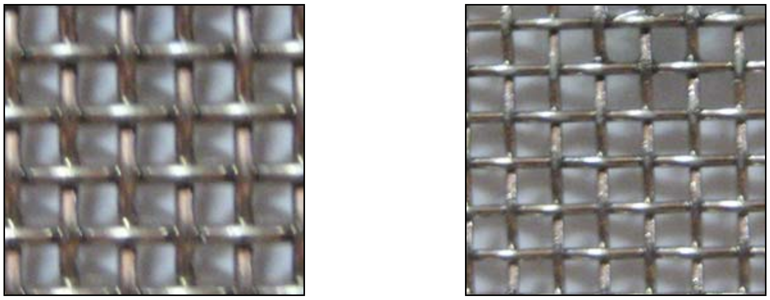

20×20, 0.017-inch, 0.436　　30×30, 0.0095-inch, 0.511

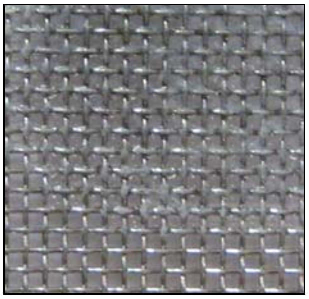

64×64, 0.0045-inch, 0.507

Figure 3.2. Woven-wire screen tested. Parameters in each figure are mesh size (*M*), wire diameter (d_w) and fraction of open area (f_{OA}).

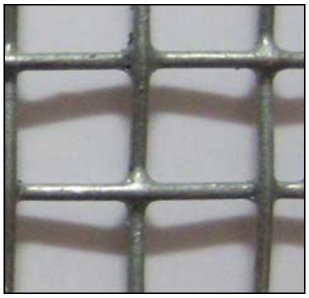

8×8, 0.017-inch, 0.746

Figure 3.3. Welded-wire screen tested. Parameters in each figure are mesh size (M), wire diameter (d_w) and fraction of open area (f_{OA}).

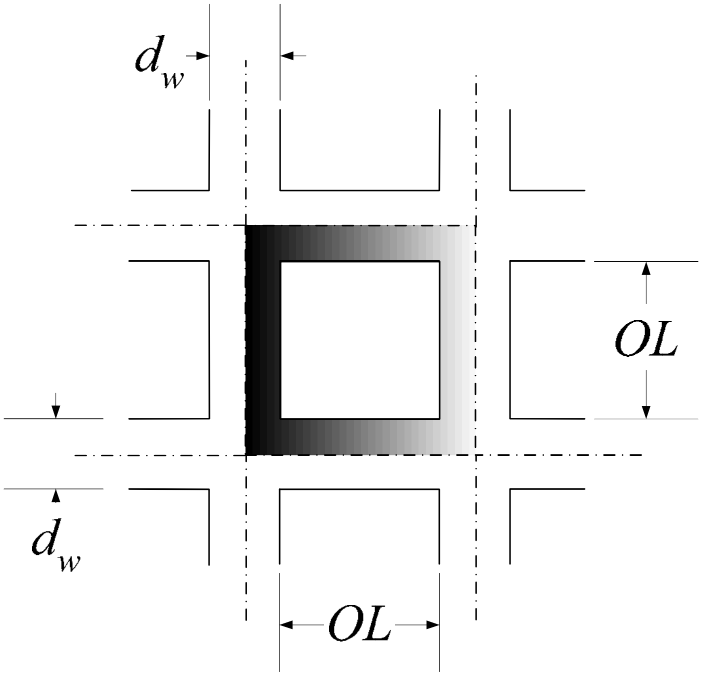

Figure 3.4. Schematic for the calculation of fraction of open area (f_{OA}) on wire screen.

wire screens sample covering a wide range of commercially available wire size and mesh openings, which could potentially be of use in aerosol sampling apparatus, were selected for the experiments.

Openings of precision electroformed-wires are consistently accurate in contrast to ordinary woven-wires. Acceptable tolerances of opening sizes for electroformed-mesh screens (InterNet Inc., Anoka, MN) are specified in the American Society of Testing and Materials (ASTM) Standard E-161-00 (ASTM, 2004a). Regardless of opening size, the allowable tolerance on the range of opening sizes is ± 2 micrometers. The tolerances for woven-wire are specified by ASTM Standard E-11-04 (ASTM, 2004b), for which a summary is given in Table 3.2.

Table 3.2. Tolerances for woven-wire and perforated-sheet openings are specified by ASTM Standard E-11-04.

Wire Diameter inch	Tolerance Micrometers	Opening Length inch	Tolerance Micrometers
Under 0.0048	± 2.54	1/16 to 1/8	± 177.8
Under 0.0080 to 0.0048	± 5.08	Over 1/8 to 3/16	± 254.0
Under 0.0120 to 0.0080	± 7.62	Over 1/8 to 1/4	± 304.8
Under 0.0024 to 0.0120	± 10.16	Over 1/4 to 3/8	± 381.0
		Over 3/8 to 1/2	± 431.8
		Over 1/2 to 3/4	± 508.0
		Over 3/4 to 1	± 762.0

Perforated-Sheet Screen

Figure 3.5 shows a round-hole perforated sheet screen with a staggered opening pattern. In general, manufacturer provides the following basic information on the screen: the fraction of open area (f_{OA}), center-to-center spacing (CS), hole size (d_h), thickness (th), and the angle of the staggered opening pattern. We calculate the fraction of open area

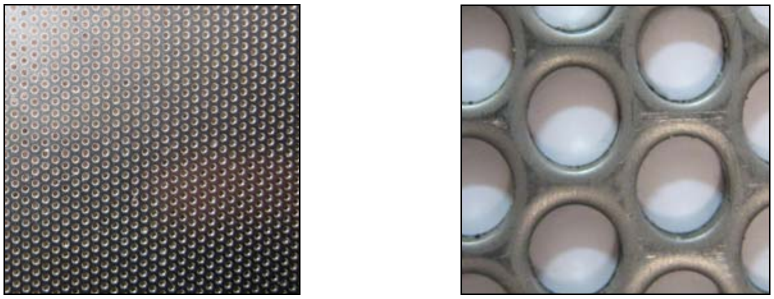

0.015-inch, 0.21 0.188-inch, 0.51

Figure 3.5. Perforated-sheet screen tested. Parameters in each figure are hole diameter (d_h) and fraction of open area (f_{OA}).

(f_{OA}) of a perforated-sheet screen by computing the fraction of the projected open screen area (Figure 3.6). The equation for f_{OA} can be expressed in the following form:,

$$f_{OA} = \frac{\pi (d_h / 2)^2}{(\sin\theta) \times (C.S.)^2} \tag{3-2}$$

Determination of the characteristic dimension (equivalent to the wire diameter for the other screen types) for perforated-sheet screen is complicated owing to the nature of the screen and the geometrical structure. It would be seen in the future chapters that the choice of the characteristic length greatly influences the shape of the collection efficiency curve. A discussion on the various methodologies examined in the course of the above research based on suggestions available in literature and the determination of the characteristic dimension is presented later. The tolerances for perforated-sheet hole diameter are specified by ASTM Standard E-323-80 (ASTM, 2004c), for which a summary is given in Table 3.3.

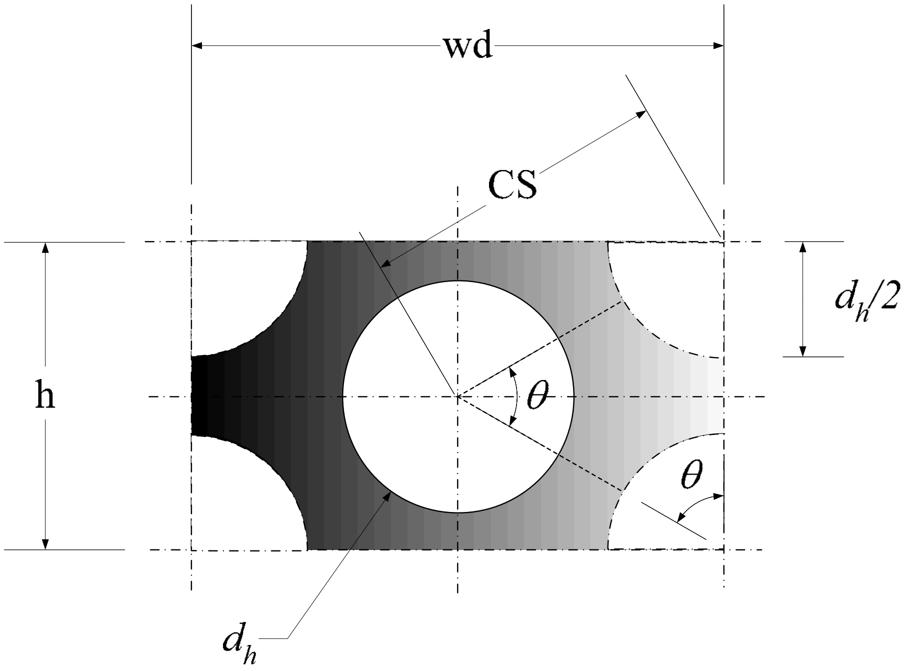

Figure 3.6. Schematic for the calculation of fraction of open area (f_{OA}) on perforated-sheet screen.

Table 3.3. Tolerances for hole diameter of perforated-sheet are specified by ASTM Standard E-323-80.

Screen Type	Hole Diameter	Tolerance
	inch	Micrometers
Perforated Sheet	Under 0.0048	± 2.54
	Under 0.0080 to 0.0048	± 5.08
	Under 0.0120 to 0.0080	± 7.62
	Under 0.0024 to 0.0120	± 10.16

CHAPTER IV

EXPERIMENTAL STUDIES

This chapter describes the experimental setup, procedure, and a screen efficiency measuring technique based on certain new configuration developments at the Aerosol Technology Laboratory (ATL). It includes mixing requirements, sampling locations, and description of measuring apparatus, data processing, experimental parameter, and methodology.

Detailed experimental studies were conducted on different commercially available screens to characterize screen deposition. Aerosol particle is generated by the Vibrating Orifice Aerosol Generator (VOAG) (Berglund and Liu, 1973) and an Aerosol Particle Sizer (APS, Model 3321, TSI Inc., St. Paul, MN), which enabled particle distribution to be checked quickly. In this study, only commercial available screens were used. The Reynolds number, Re_C (Subscript C for the characteristic length), as defined previously, varied between 0.5 and 600 for this study. For wire screens, the obstacle length (wire diameter) is used as the characteristic length. However, determination of the characteristic length in the case of perforated sheet screens is more complicated, and is estimated based on the diameter of an imaginary wire (effective slack length), as demonstrated in the calculation presented in Appendix-1. The collection efficiency is obtained as a function of Stokes number.

Aerosol Generator

A nearly monodisperse aerosol was generated with a vibrating orifice aerosol generator from a mixture of non-volatile oleic acid, ethanol, and a fluorescent analytical tracer (sodium fluorescein). The test aerosol was passed through a 10 mCi Kr-85 source to neutralize any electrical charge on the aerosol. The particles are thus brought to a state of Boltzmann charge equilibrium. A mixture of master solution is the combination of 9% oleic acid and 1% sodium fluorescein salt (uranine) dissolved in 90% ethanol to create the liquid particle. The interested range of particle size is controlled by diluting the master solution while maintaining the operational parameters of the VOAG.

Aerosol Size Distribution and Measurement of Aerosol Particle Size

The consistency of aerosol concentration and monodispersity is an important consideration when generating the aerosol particle. The diameter of the aerosol particles was determined by collecting a sample on an oil-phobic glass slide and then measuring the apparent size under a microscope. Aerodynamic diameter, d_a, of the aerosol particles is calculated from:

$$d_a = \frac{d_m}{f}\sqrt{\frac{C_P \rho_P}{C_a \rho_w}} \tag{4-1}$$

Here, d_m = diameter of the droplets measured under the microscope; f = flattening factor to account for distortion of a droplet on a microscope slide (Olan-Figueroa et al., 1982); C_p = Cunningham's slip correction factor based on the physical particle diameter (d_m/f); ρ_P = droplet density (934 kg/m^3) for a mixture of oleic acid and sodium fluorescein tracer; C_a = Cunningham's slip correction factor based on the aerodynamic diameter; and, ρ_w = density of water.

The value of *f* is 1.29 (ATL, 2005) for oleic acid/sodium fluorescein mixture deposited on slides coated with an oil-phobic agent (NYEBAR, Type Q, 2.0%, NYE Lubricants Inc., New Bedford, MA). During the course of an experiment, the size distribution of particles output from the VOAG is continuously monitored with an APS. This equipment is used to provide assurance of a constant particle size throughout the experiment; however, because of errors of this device in sizing liquid droplets (Baron, 1986), it is not used for characterizing the actual size. The particle size range spanned by the APS is from 0.5 to 20 μm. Particles are also detected in the 0.3 to 0.5 μm range using light-scattering.

Experimental Methodology

Figures 4.1 and 4.2 show a photo and a schematic diagram of the system used for the screen penetration tests. The system is comprised of a Vibrating Orifice Aerosol Generator (VOAG, Berglund and Liu, 1973), a Kr-85 neutralizer, a vertical tube (147 mm diameter), an Aerosol Particle Sizer (APS, Model 3321, TSI Inc., St. Paul, MN), a filter holder, and a Hi-Vol blower. The Hi-Vol blower (Model GBM2360, ThermoAndersen, Smyrna, GA) system was calibrated using a Roots meter (Model 5M 125 TC, Dresser Measurement, Houston, TX), a digital flow meter (HFC-digital-1400, Hi-Q Env. Products, San Diego, CA), and a U-tube or digital manometer (Model 8360, TSI Inc., St. Paul, MN).

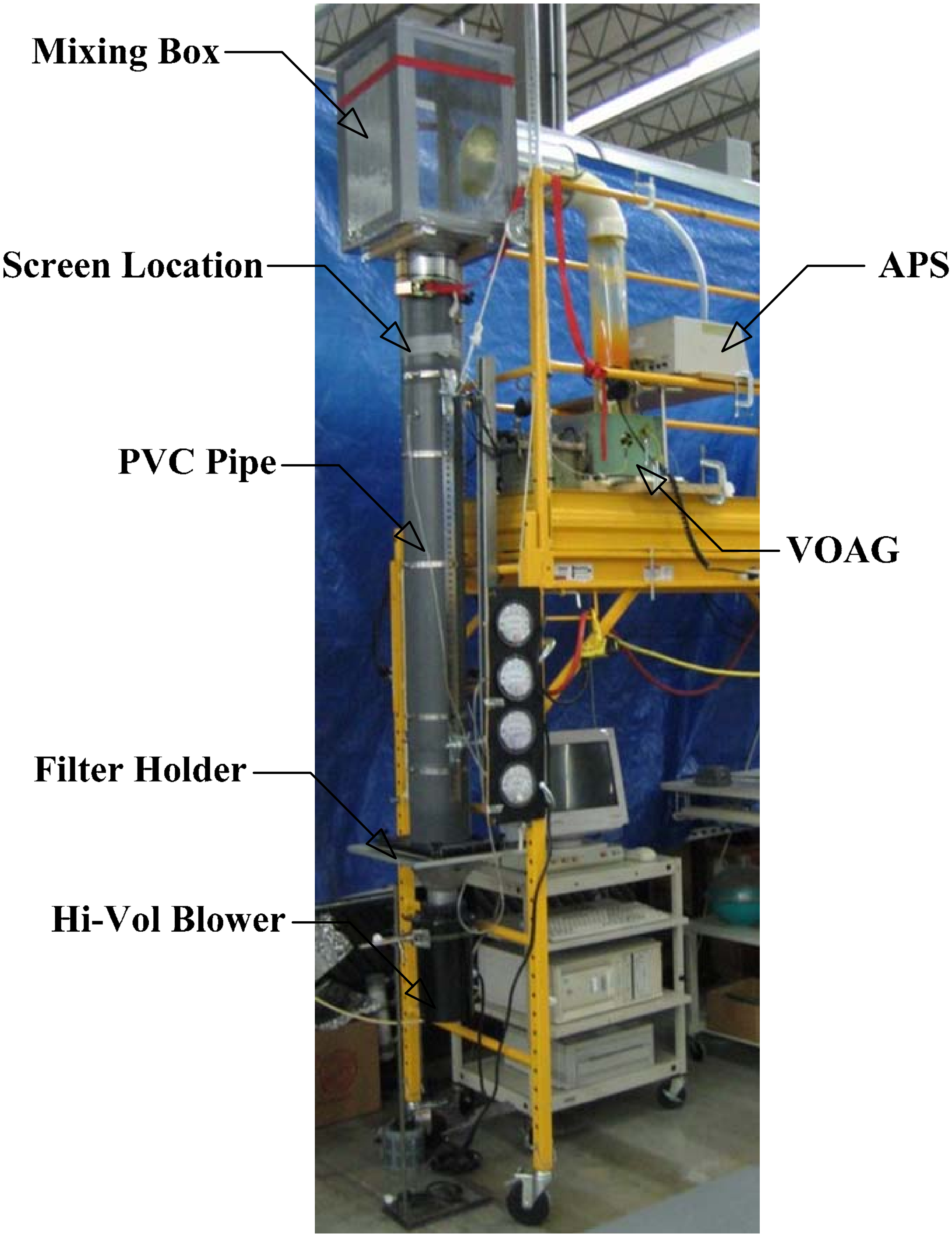

Figure 4.1. Photo of setup for screen test.

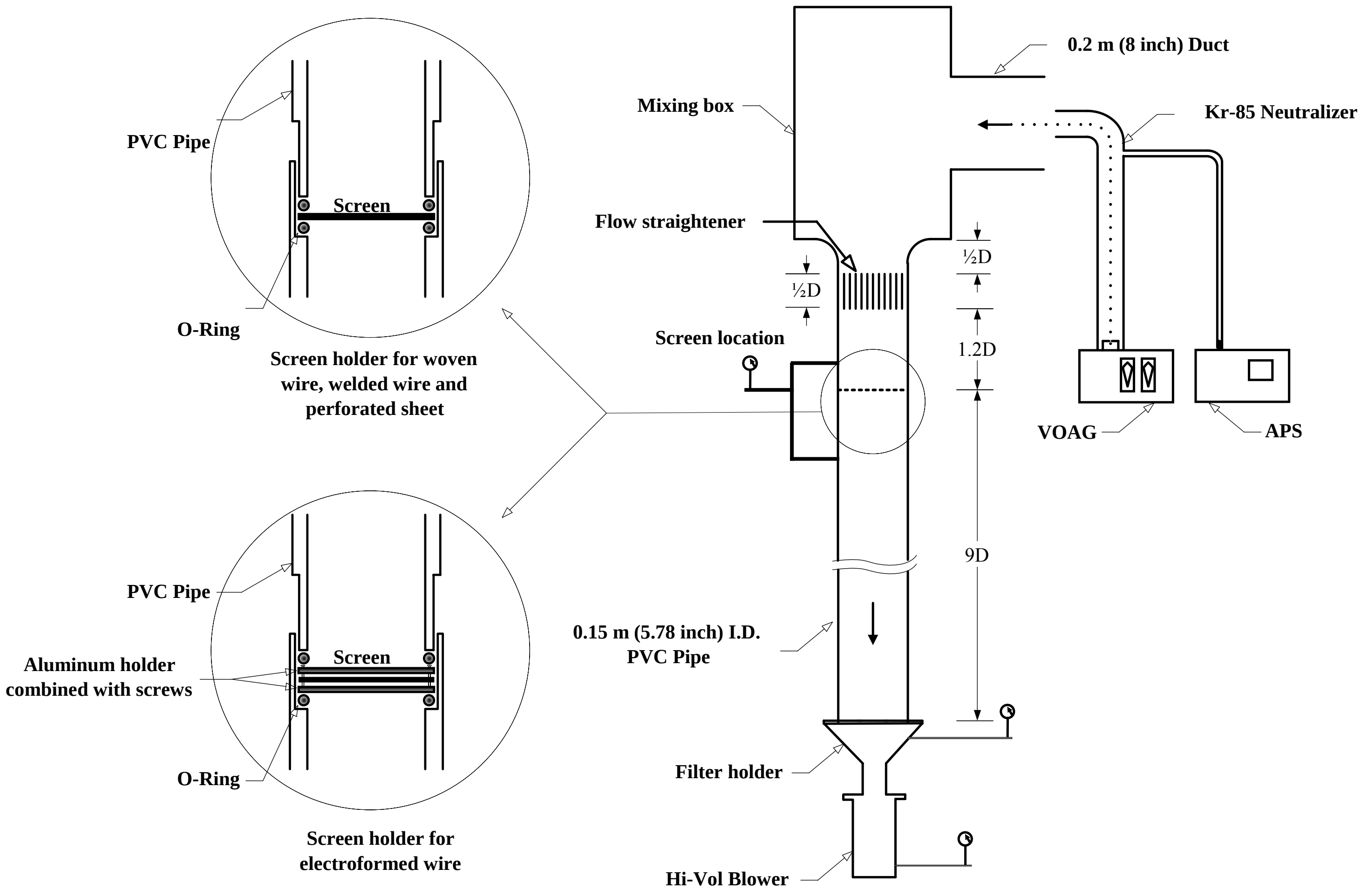

Figure 4.2. Schematic of setup for screen test.

Pressure drop across the screen was measured with a Magnehelic differential pressure gauge (Dwyer Instruments, Michigan City, IN). A Hi-Vol blower system was calibrated using a roots meter (full flow ranges; 200-3000 L/min) and H-Q digital meter (low flow ranges; 200–1500 L/min) with U-tube and digital manometer was shown in Figure 4.3. The flow rates are continuously monitored with digital pressure meter and manometer.

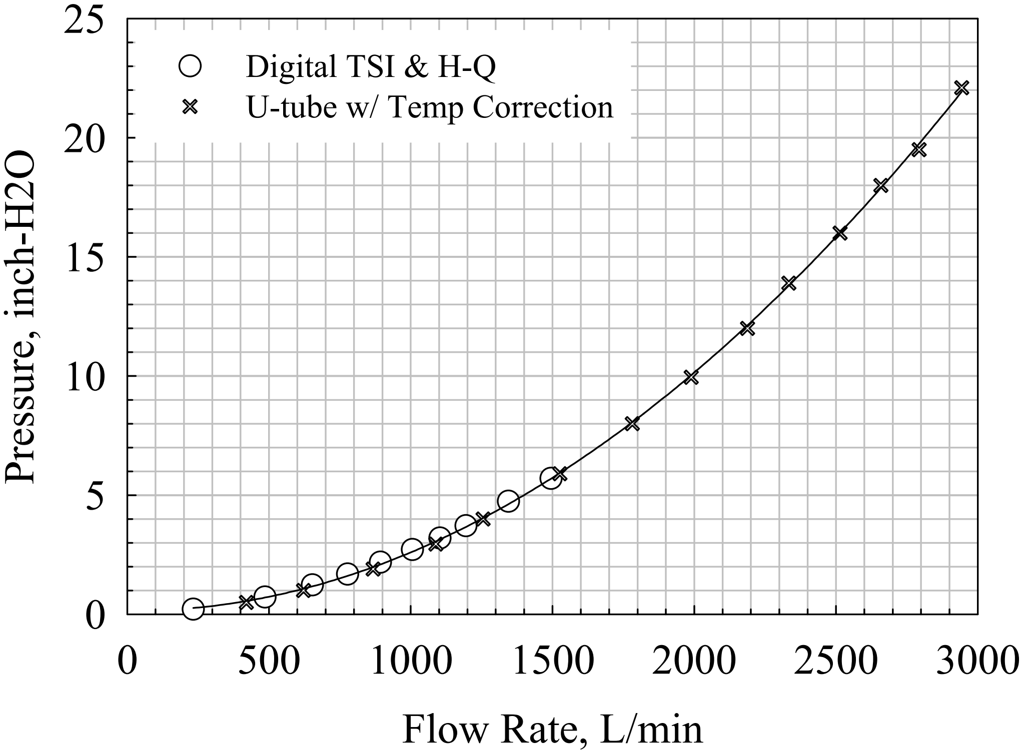

Figure 4.3. Calibration result of Hi-Vol Blower using root meter (full flow ranges; 200-3000 L/min) and H-Q digital meter (low flow ranges; 200–1500 L/min) with U-tube and digital manometer.

The test procedure consists of first placing the screen and filter medium in the holder, bringing the aerosol generator to a steady operating condition, and then measuring the particle size distribution generated by the VOAG. The electrically neutralized aerosol is passed through a 0.203 m (8.0 inches) duct into a Generic Tee Plenum (Han et al., 2005). The characteristic dimensions of the GTPs are 0.305 m × 0.305 m × 0.457 m (12 inches × 12 inches × 18 inches), where the dimensions are scaled to the reference dimensions of the duct (0.203 m). The GTP mixing system was developed to provide ANSI/HPS Standard N13.1-1999 compatible sampling locations in short runs of ducts downstream of the mixing element and operate with a relatively low pressure loss.

Results from these tests show that the mixing is well within the ANSI/HPS Standard N13.1-1999 criteria – the coefficient of variation (*COV*) for velocity and tracer gas were less than the 20% criteria levels at measurement locations (0.7 duct diameters upstream and 1 duct diameter downstream of the screen location). Velocity measurements were made with a TSI Inc., thermal anemometer, Model 8360, Serial Number 505025. Tracer gas tests were conducted by releasing a continuous stream of dilute sulfur hexafluoride (SF6) at the center of the duct intake (Figure 4.2). Samples were extracted at the sampling location with 60 mL hypodermic syringes from the 4-points of each traverse location for the flow rate of 1080 L/min. The samples were analyzed with a gas chromatograph (Lagus Model 101 Autotrac, Serial Number 140, Lagus Applied Technology, Inc., San Diego, CA).

The detailed flow disturbance velocity measurements and turbulent intensities was provided at the sampling location, which were produced by using a TSI Inc., hot wire anemometer, Model 157 (Table 4.1 and Figures 4.4 to 4.9). Measurements for characterizing the *COV*s of velocity with and without screens were made at the sampling locations. Tests were conducted at a particular flow condition, about 1200 L/min. Velocity measurements were made at the center 7-points of each traverse location. Next,

Table 4.1. The summary of average velocity and *COV* at each configuration.

Configuration and Location	u_{AVG} (m/s)	$Std.\ Dev._{AVG}$	*COV*
Without screen			
Upstream	1.62	0.26	16.10
Downstream	1.62	0.14	8.70
With screen			
16×16 Mesh, 0.018-inch, 51%			
Upstream	1.59	0.23	14.20
Downstream	1.64	0.08	5.00
20×20 Mesh, 0.017-inch, 44%			
Upstream	1.62	0.29	17.80
Downstream	1.60	0.06	3.40

the data collected at each traverse point were normalized to the mean velocity of the set. The *COV* was then computed from the standard deviation of the normalized velocity values at each point. The average *COV* was then computed from the *COV*s of each test. Table 4.1 shows the *COV*s of velocity concentrations for the two different screens at measurement locations 0.5-duct diameter upstream and 1.0-duct diameter downstream of the screen location. The screen produced *COV*s of less than 18.0% for the velocity concentration at 0.5 duct diameters upstream and less than 5.0% for 1.0 duct diameter downstream. From these velocity results obtained in the present study, the use of GTP downstream of the interface of the system appears to affect the good mixing performance for aerosol deposition on screens.

The flow is drawn through a 0.147 m (5.78 inches) diameter vertical pipe, then through a glass fiber filter, and exhausted from the system. A Hi-Vol blower and voltage meter arrangement with a flow controller was used to suck air from the system. The conditions of the tests for this study are presented in Table 4.2, which are shown as particle size, flow rates, flow Reynolds number, characteristic length Reynolds number,

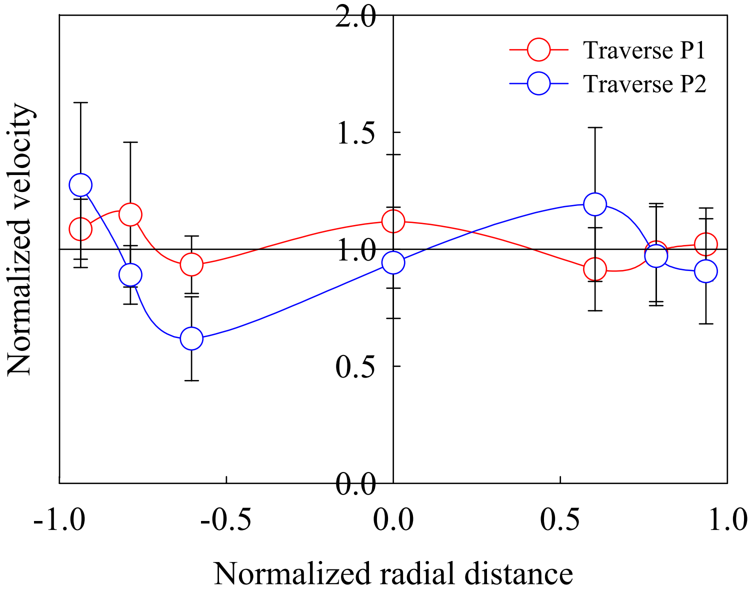

(a) Normalized velocity profile

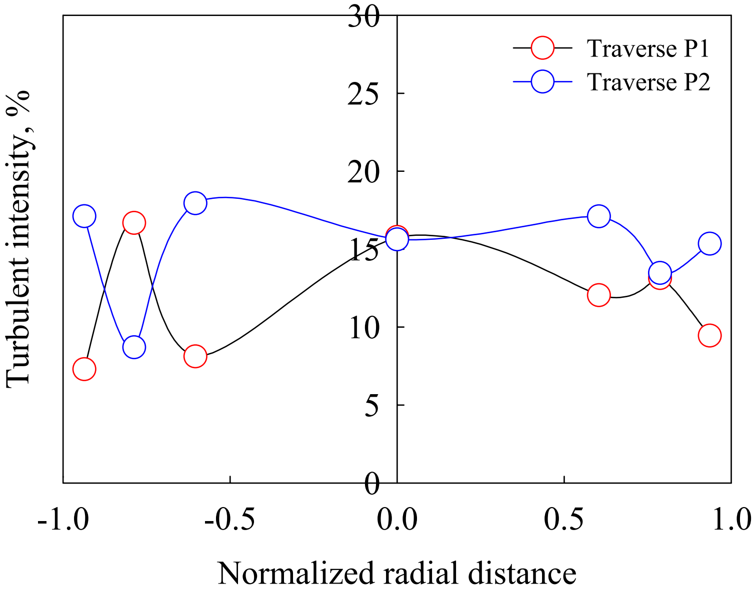

(b) Turbulent intensity profile

Figure 4.4. Normalized velocity profile and turbulent intensity at 0.7-duct diameter upstream of screen location. $u_{\mathrm{AVG}} = 1.62$ m/s, $Std.\ Dev._{\mathrm{AVG}} = 0.261$, $COV = 16.1\%$.

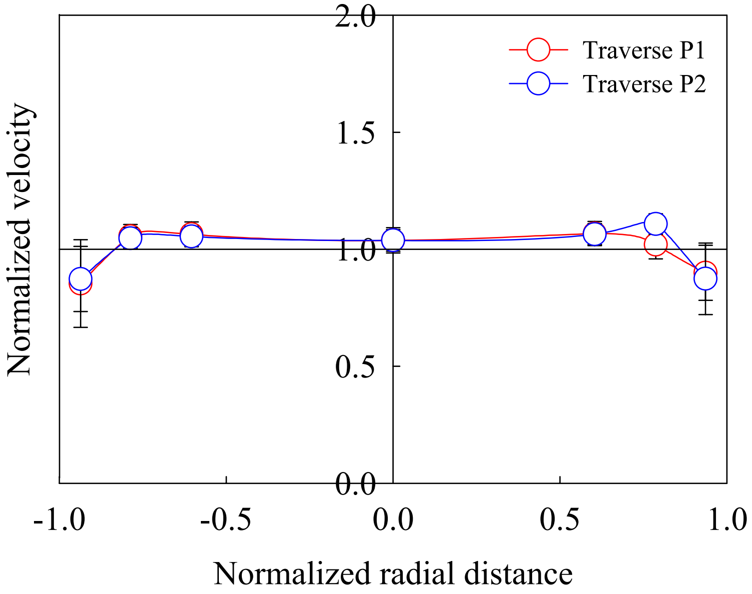

(a) Normalized velocity profile

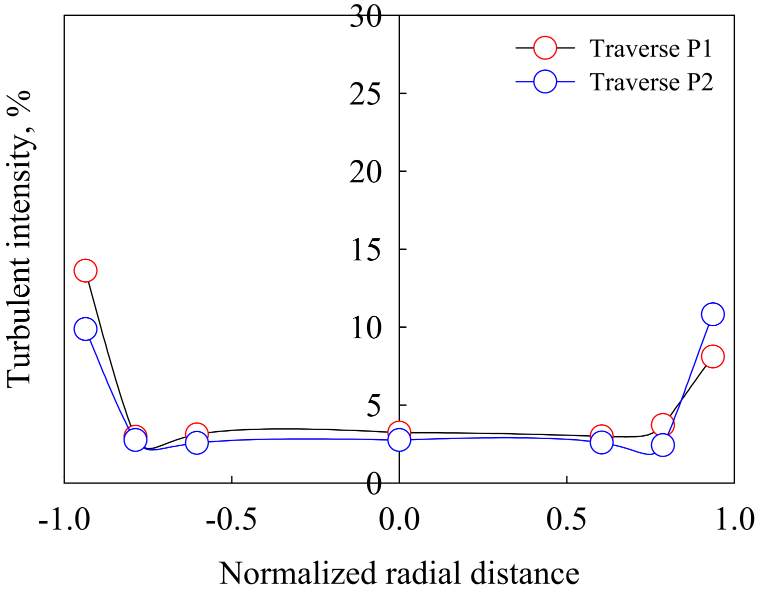

(b) Turbulent intensity profile

Figure 4.5. Normalized velocity profile and turbulent intensity at 1.0-duct diameter downstream of screen location. $u_{\mathrm{AVG}} = 1.62$ m/s, *Std. Dev.*$_{\mathrm{AVG}} = 0.141$, *COV* = 8.7%.

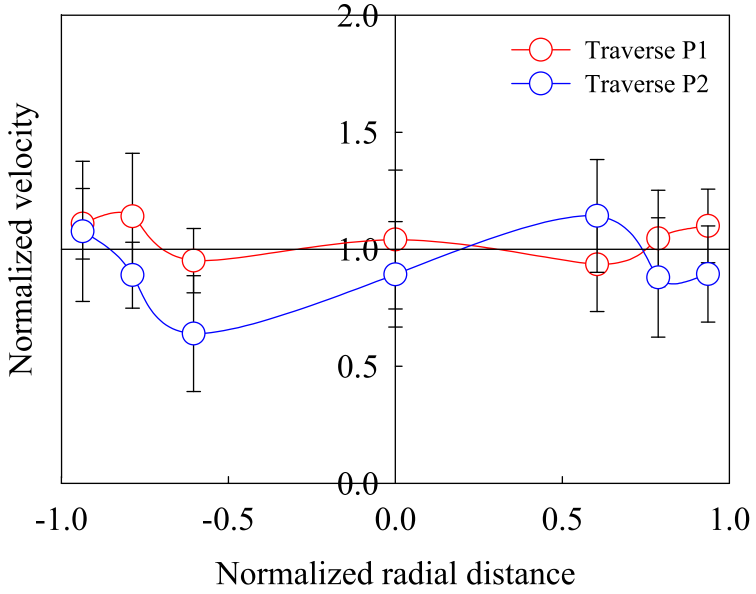

(a) Normalized velocity profile

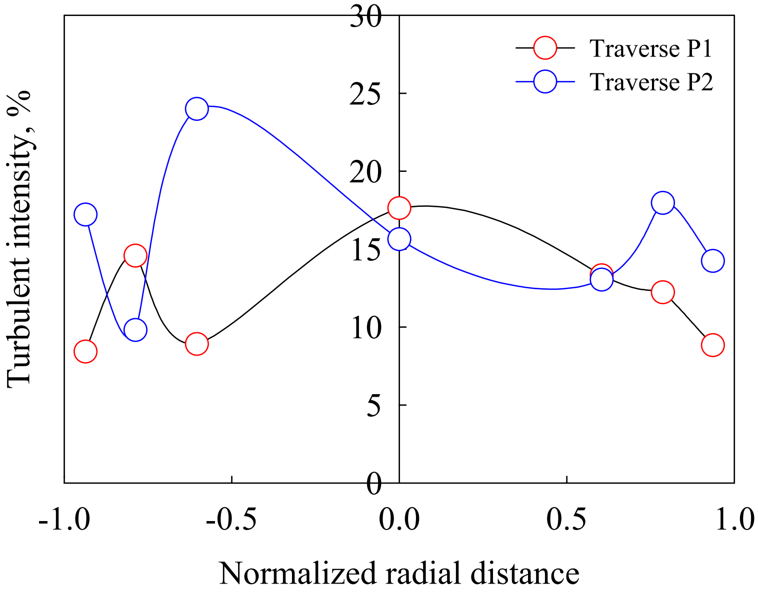

(b) Turbulent intensity profile

Figure 4.6. Normalized velocity profile and turbulent intensity at 0.7-duct diameter upstream of screen location with screen (16×16 Mesh, 0.018-inch, 0.51). u_{AVG} = 1.59 m/s, *Std. Dev.*$_{\mathrm{AVG}}$ = 0.225, *COV* = 14.2%.

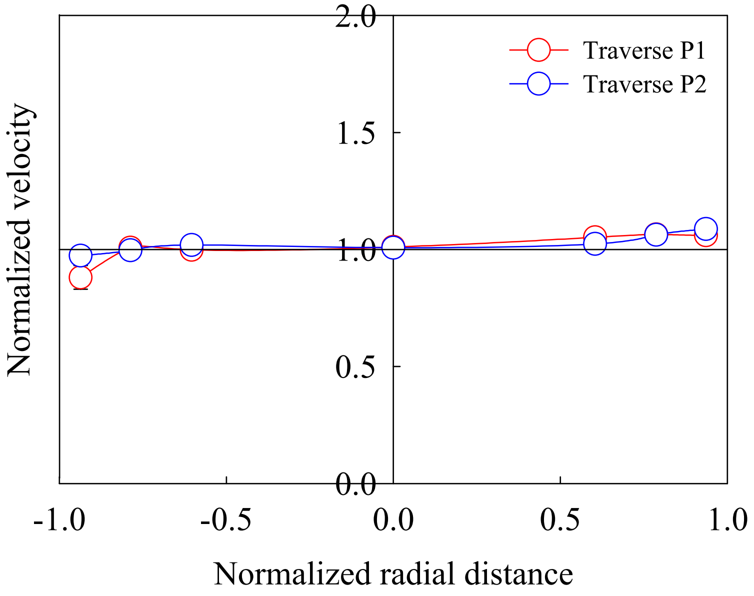

(a) Normalized velocity profile

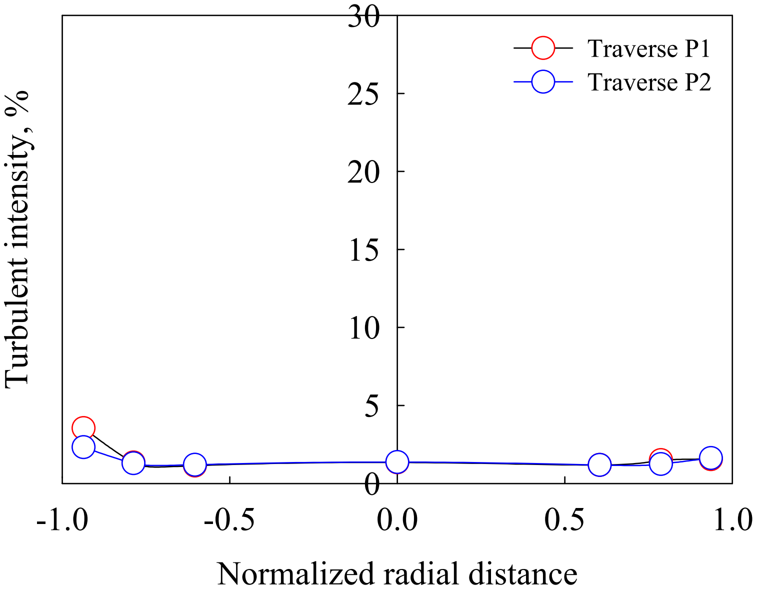

(b) Turbulent intensity profile

Figure 4.7. Normalized velocity profile and turbulent intensity at 1.0-duct diameter downstream of screen location with screen (16×16 Mesh, 0.018-inch, 0.51). $u_{\mathrm{AVG}} = 1.64$ m/s, *Std. Dev.*$_{\mathrm{AVG}} = 0.082$, *COV* = 5.0%

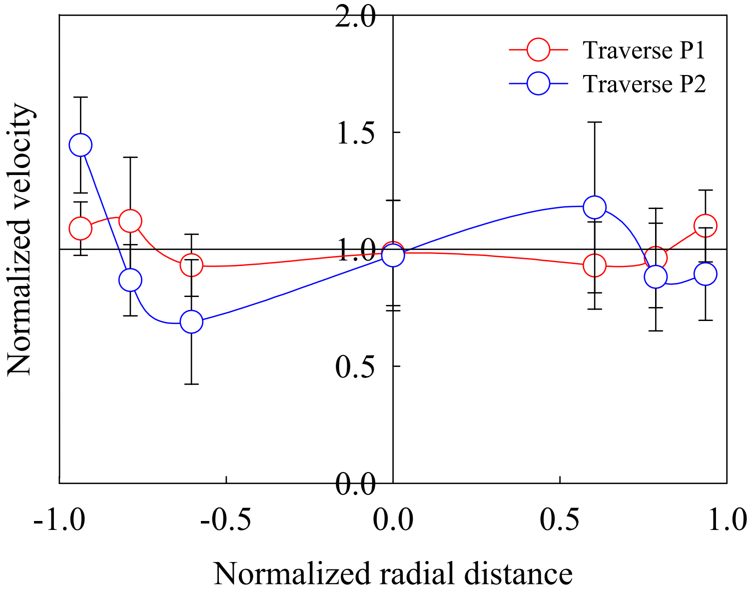

(a) Normalized velocity profile

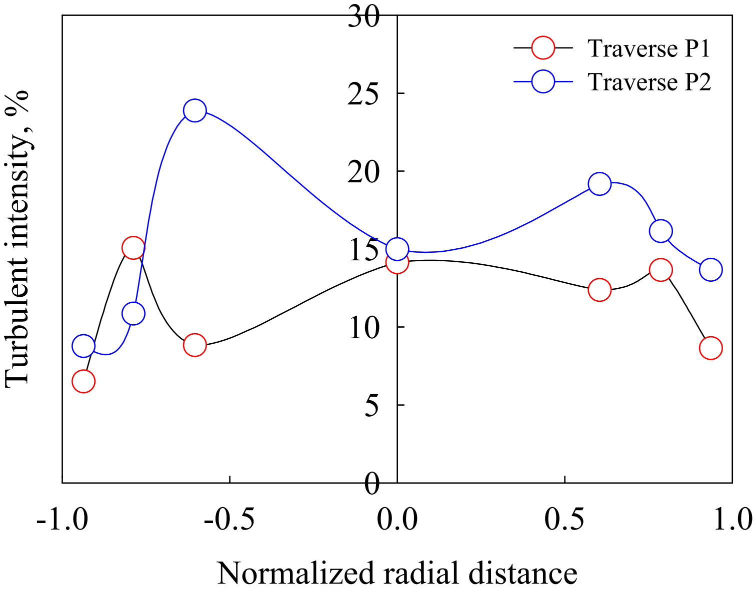

(b) Turbulent intensity profile

Figure 4.8. Normalized velocity profile and turbulent intensity at 0.7-duct diameter upstream of screen location with screen (20×20 Mesh, 0.017-inch, 0.44). $u_{\mathrm{AVG}} = 1.62$ m/s, *Std. Dev.*$_{\mathrm{AVG}} = 0.288$, *COV* = 17.8%

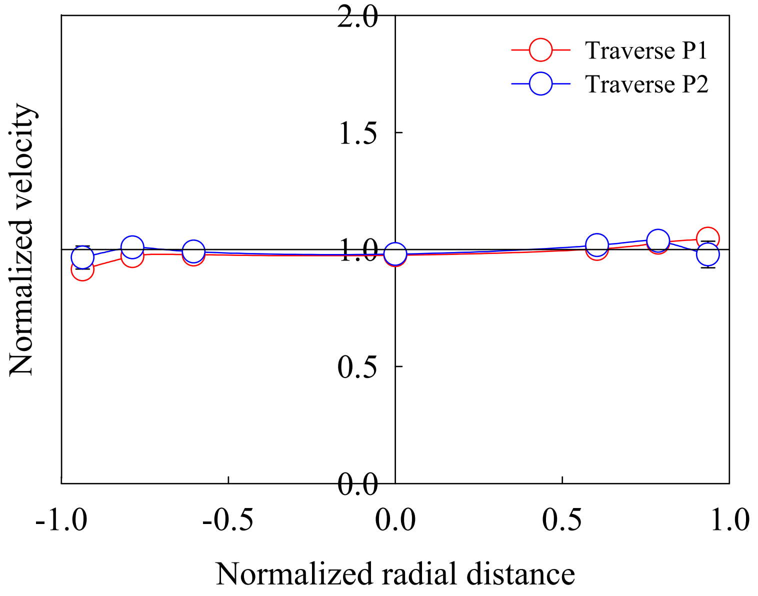

(a) Normalized velocity profile

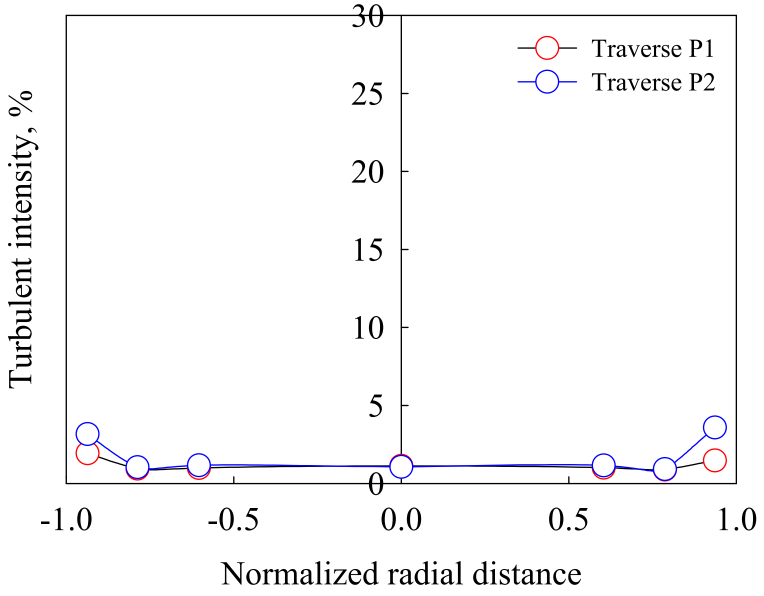

(b) Turbulent intensity profile

Figure 4.9. Normalized velocity profile and turbulent intensity at 1.0-duct diameter downstream of screen location with screen (20×20 Mesh, 0.017-inch, 0.44). $u_{\mathrm{AVG}} = 1.60$ m/s, $Std.\ Dev._{\mathrm{AVG}} = 0.055$, $COV = 3.4\%$

Table 4.2. Operation condition of experiment for each screen.

	Screen Type	**Wire diameter Hole diameter** (dw or d_h) inch	µm	**Fraction of Open Area** (f_{OA}) %	**Mesh Size** (M)	**Particle size AD** µm	***Q*** Min-Max L/min	***Re*** Min-Max	***Re_C*** Min-Max	***R*** Min-Max	***Stk*** Min-Max
1	Electroformed	0.00629	160	56.0	40	N/A	N/A	N/A	N/A	N/A	N/A
2	Electroformed	0.00268	68	75.0	50	N/A	N/A	N/A	N/A	N/A	N/A
3	Electroformed	0.00138	35	88.0	45	4-20	196-1962	1839-18411	0.5-5	0.122-0.559	0.63-14.76
4	Electroformed	0.00257	65	90.0	20	4-20	108-1080	1013-10135	0.5-5	0.066-0.301	0.56-19.02
						4-20	108-1962	1013-18411	0.5-5	0.066-0.559	0.56-19.02
1	Woven	0.0170	432	43.6	20	3-20	300-2500	2815-23460	19-158	0.007-0.047	0.10-6.92
2	Woven	0.0045	114	50.7	64	10-17	109-2356	1026-22108	2-34	0.089-0.152	0.30-7.91
3	Woven	0.0180	457	50.7	16	3-20	100-2500	2815-23460	17-144	0.007-0.045	0.09-6.53
4	Woven	0.0095	241	51.1	30	10-20	150-2356	1408-22108	5-71	0.042-0.083	0.20-7.46
5	Woven	0.0160	406	55.4	16	3-20	300-2500	2815-23460	14-117	0.007-0.050	0.10-7.35
6	Woven	0.0170	432	58.1	14	3-20	250-2500	2347-22437	12-119	0.007-0.047	0.10-6.92
7	Woven	0.0095	241	71.9	16	3-20	112-2500	1051-23460	2-54	0.012-0.083	0.23-7.60
						3-20	80-2500	751-23460	1-268	0.007-0.152	0.08-8.36
1	Welded	0.0170	432	74.6	8	3-20	300-2500	2815-23460	11-93	0.007-0.047	0.13-6.92
1	Perforated	0.0150	381	21.0	N/A	7-20	210-2620	1971-24586	27-340	0.016-0.047	0.17-6.93
2	Perforated	0.1875	4763	51.0	N/A	11-20	550-2500	5161-23460	126-573	0.006-0.011	0.11-1.63
						7-20	210-2500	1971-24586	27-573	0.006-0.047	0.11-6.93
						3-20	80-2500	751-24586	0.5-573	0.0067-0.559	0.08-19.02

*Note: Grey highlight is for the overall ranges for each screen.

interception parameter and Stokes number ranges. Samples obtained through the screen are collected on 8 inches × 10 inches rectangular sheet filters (Part No. FP2063-810, Borosilicate Glass Fiber, HI-Q Environmental Products Co., San Diego, CA). Each screen with the dimension of 0.157 m (6.17 inches) diameter was positioned horizontally at a distance of 1.2-duct diameters below the flow straightener.

The system was operated with after-filter (AF) placed downstream of mesh-screen (SM). A solution of 2/3 (200 mL) isopropyl alcohol and 1/3 (100 mL) distilled water was used to elute the sodium fluorescein from the collection filter and to wash it from the screens. One drop of sodium hydroxide (1N) is added to the solution in order to stabilize the fluorescein, which is then analyzed with a digital fluorometer (Model 450, Sequoia-Turner Corp., Mountain View, CA). The relative aerosol concentration, C, is calculated from:

$$C = \frac{c_f \cdot V}{Q \cdot t} \tag{4-2}$$

Here, c_f = concentration of fluorescein in filter or screen sample (fluorometer reading); V = volume of solution used to elute the tracer; Q = corrected air flow rate; and, t = sampling time. The actual efficiency of the screen, η_A, can be expressed as:

$$\eta_A = \frac{C_{SM}}{C_{SM} + C_{AF}} \tag{4-3}$$

The aerosol penetration through a screen, P, is:

$$P = 1 - \eta_A \tag{4-4}$$

Wall losses between the screen holder and filter holder (Figure 4.10) were measured to be about 0.3% to 6%, in the range of flow Reynolds number (Re), 500 to 20000.

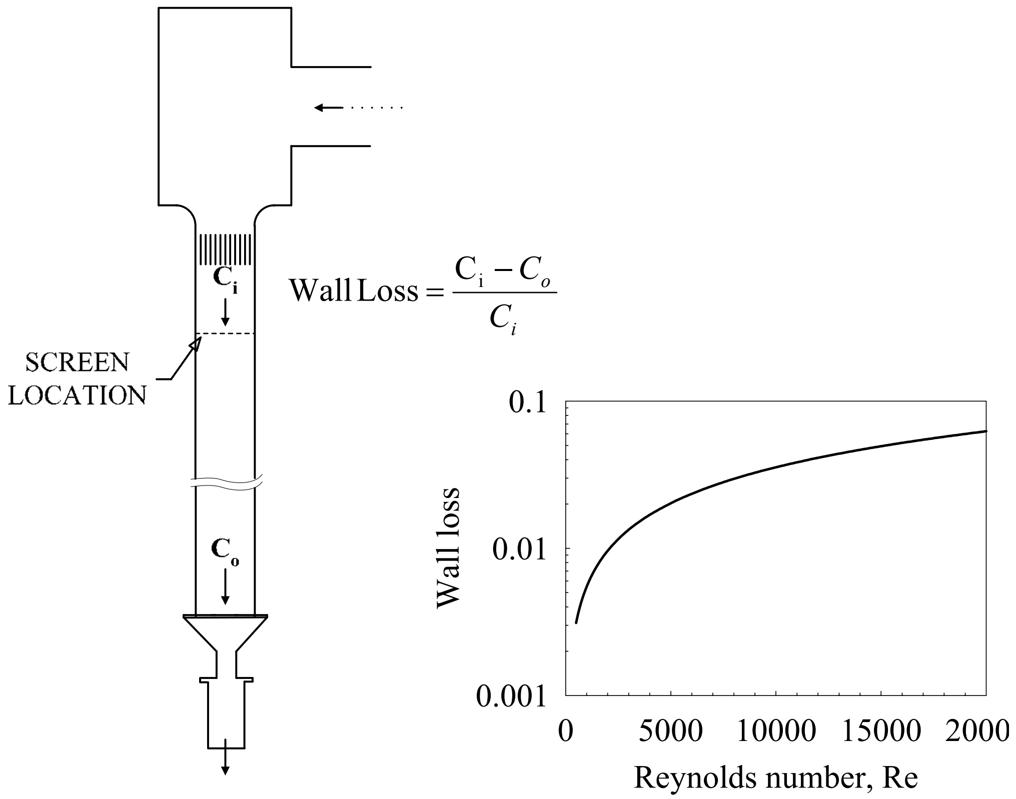

Figure 4.10. Wall losses between screen holder and filter holder.

Table 4.3. Minimum and maximum wall losses for each screen.

Screen	Wire/Hole Diameter inch	Areal Porosity	Mesh Size	Wall Loss Min	Wall Loss Max
Electroformed	0.00257	0.90	20	0.52%	2.45%
	0.00138	0.88	45	0.69%	4.34%
Woven	0.014	0.21	40	0.91%	5.56%
	0.017	0.44	20	0.89%	5.56%
	0.005	0.51	64	0.53%	5.23%
	0.018	0.51	16	0.89%	5.56%
	0.010	0.51	30	0.60%	5.23%
	0.016	0.55	16	0.89%	5.56%
	0.017	0.58	14	0.79%	5.56%
	0.010	0.72	16	0.32%	5.56%
Welded	0.017	0.75	8	0.89%	5.56%
Perforated	0.016	0.21	N/A	0.72%	5.84%
	0.063	0.51	N/A	1.38%	5.56%

An appropriate correlation was developed based on the above data (Figure 4.10) and used to correct the actual efficiency value calculate for each data point (Table 4.3). Therefore, the actual efficiency of the screen, η_A, can be redefined as a ratio of the screen relative to the concentration to the total relative concentration (screen plus filter) for this study, and can be expressed as:

$$\eta_A = \frac{C_{SM}}{C_{SM} + C_{AF}/(1 - WL)} \tag{4-5}$$

To verify the computational results, it is desired to have not only data on penetration but also on the screen pressure drop. Two pressure taps were installed on the screen holder, one on the upstream side of the screen, the other on the downstream side. A digital manometer was used to measure the screen pressure drop to ±0.01 inches of water. The particular digital manometer has a range of 0 to 10 inches of water. For pressure drops above 10 inches of water, a conventional U-tube manometer was used.

Experimental Results

For four different types of screens (electroformed-wire, woven-wire, welded-wire, and perforated-sheet), the experimental measurements of efficiency were made with particle sizes ranging from 3 to 20 μm AD. Due to the micrometer particle size involved in the impaction regime, an experimental measurement of pure mechanism (interception, inertial impaction or gravitation) is very difficult. Most of the deposition phenomenon includes the combination of mechanisms. Hence, the actual efficiency measured in this section will be considered the impaction, interception, and gravitational effects. The flow rate was varied between 80 to 2500 L/min. The results of the screen efficiency measurements are shown in Figures 4.11 to 4.22. In these figures, η_A is the actual

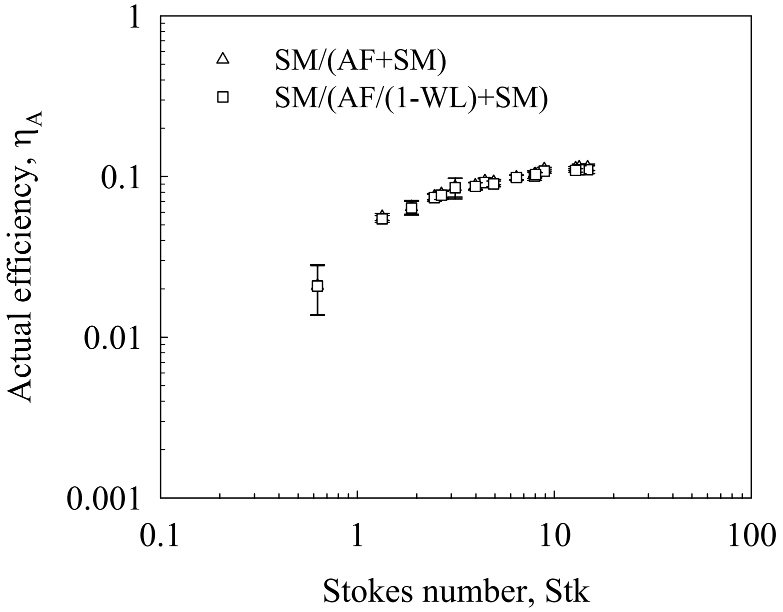

Figure 4.11. Actual efficiency as a function of Stokes number for electroformed-wire screen (45×45, 0.00138-inch, 0.88).

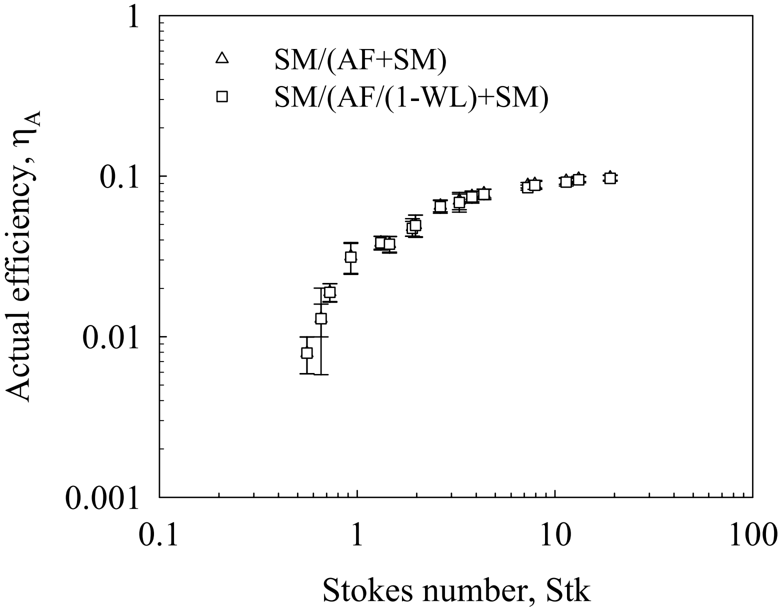

Figure 4.12. Actual efficiency as a function of Stokes number for electroformed-wire screen (20×20, 0.00257-inch, 0.90).

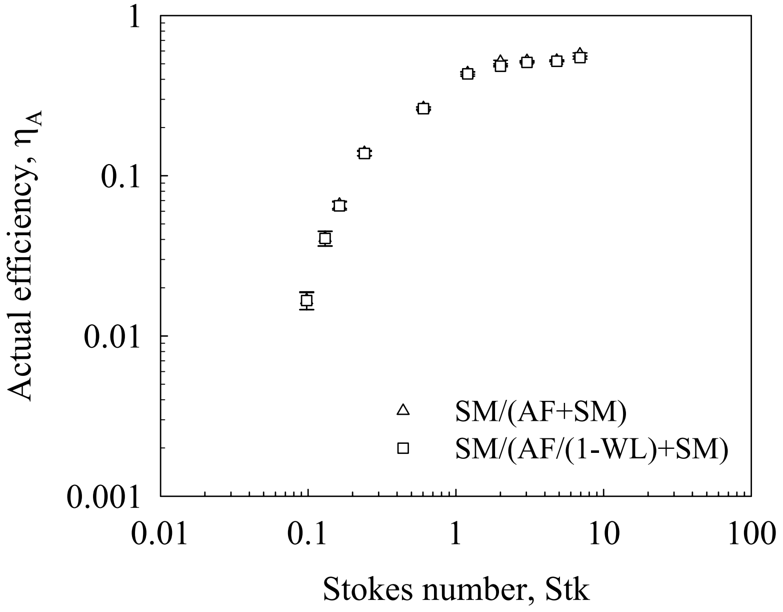

Figure 4.13. Actual efficiency as a function of Stokes number for woven-wire screen (20×20, 0.017-inch, 0.436).

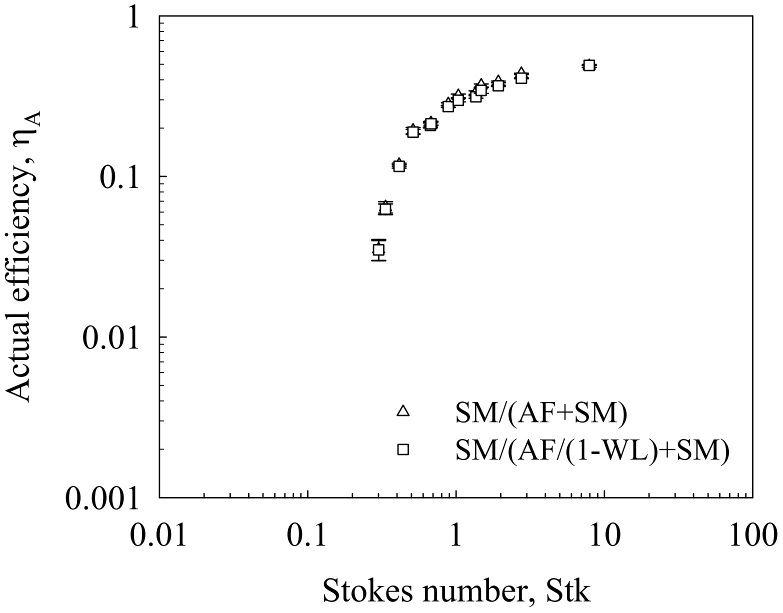

Figure 4.14. Actual efficiency as a function of Stokes number for woven-wire screen (64×64, 0.0045-inch, 0.507).

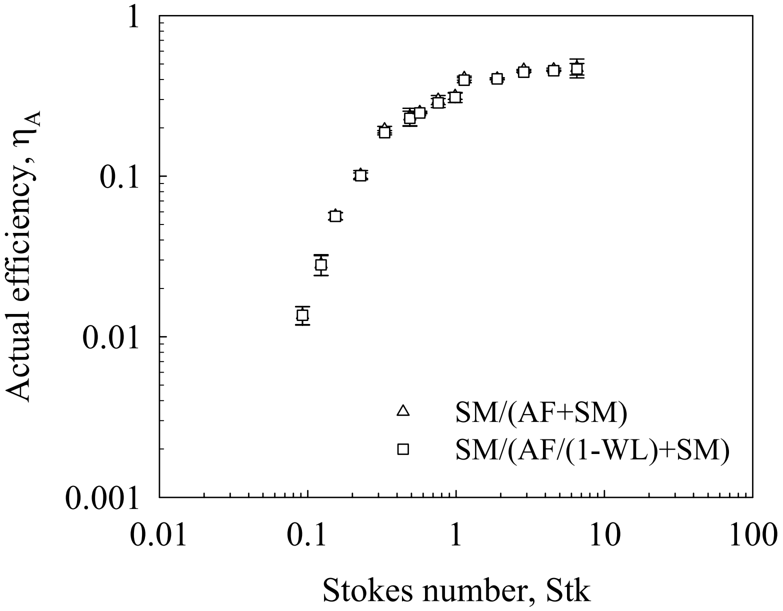

Figure 4.15. Actual efficiency as a function of Stokes number for woven-wire screen (16×16, 0.018-inch, 0.507).

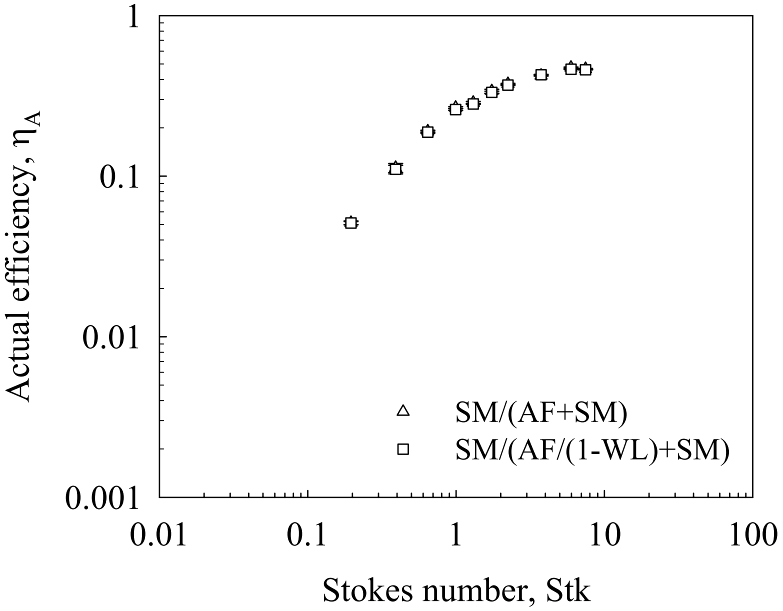

Figure 4.16. Actual efficiency as a function of Stokes number for woven-wire screen (30×30, 0.0095-inch, 0.511).

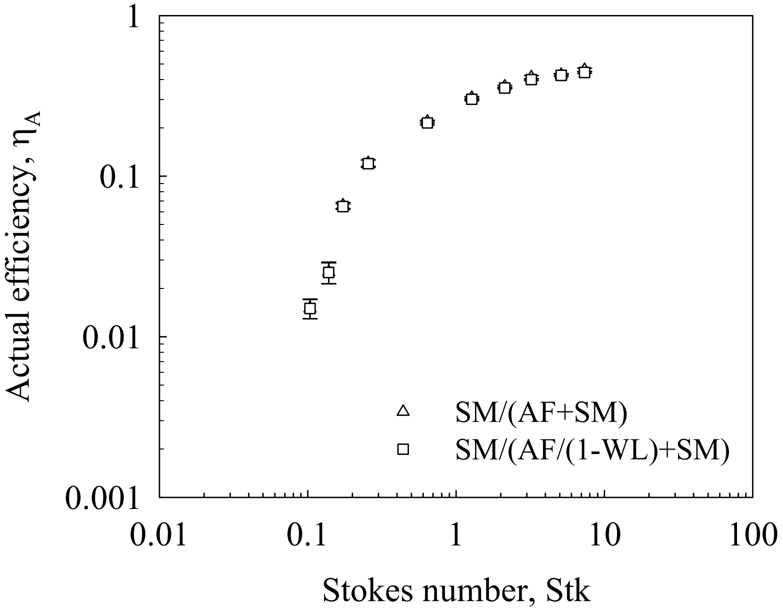

Figure 4.17. Actual efficiency as a function of Stokes number for woven-wire screen (16×16, 0.016-inch, 0.554).

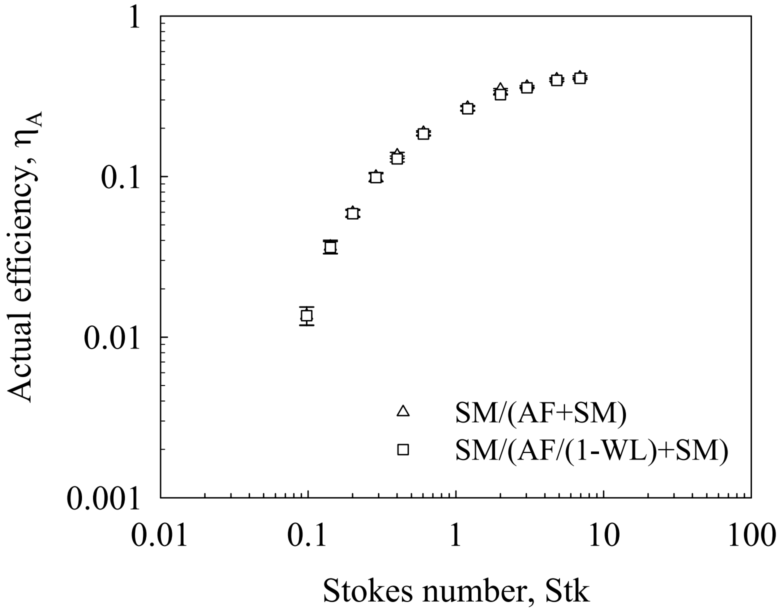

Figure 4.18. Actual efficiency as a function of Stokes number for woven-wire screen (14×14, 0.017-inch, 0.581).

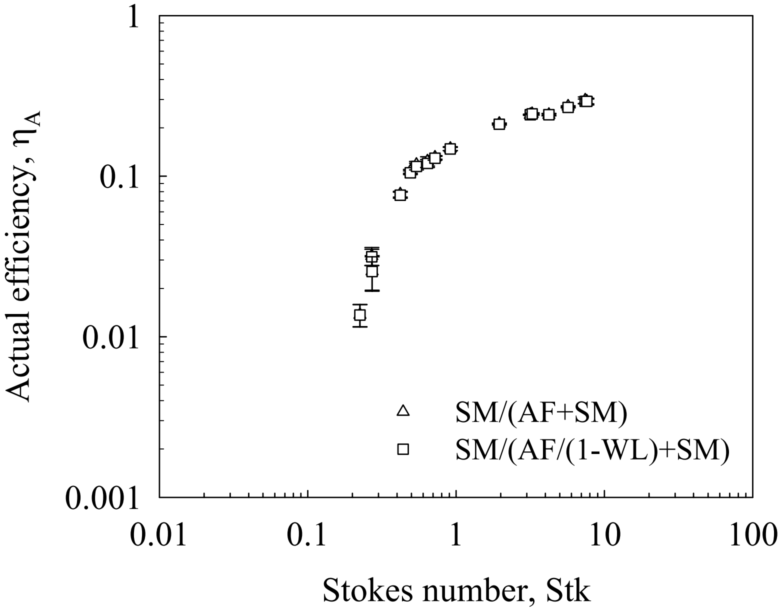

Figure 4.19. Actual efficiency as a function of Stokes number for woven-wire screen (16×16, 0.0095-inch, 0.719).

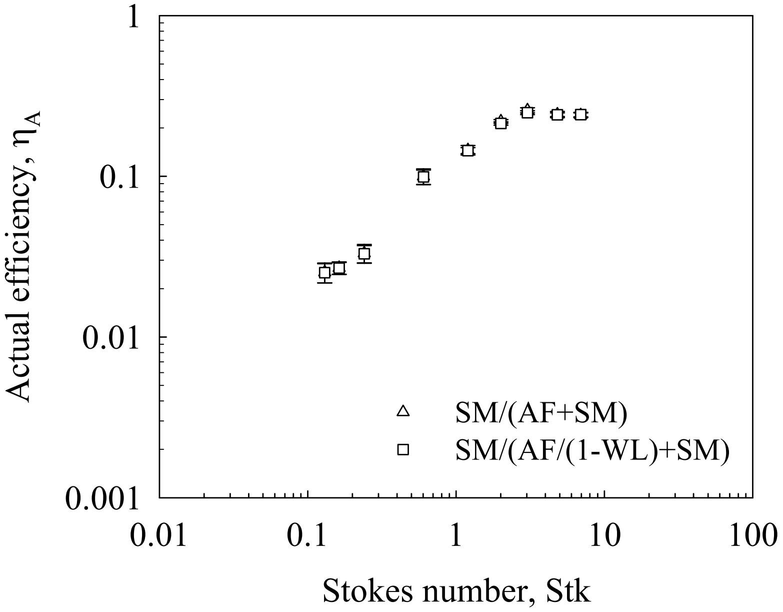

Figure 4.20. Actual efficiency as a function of Stokes number for welded-wire screen (8×8, 0.017-inch, 0.746).

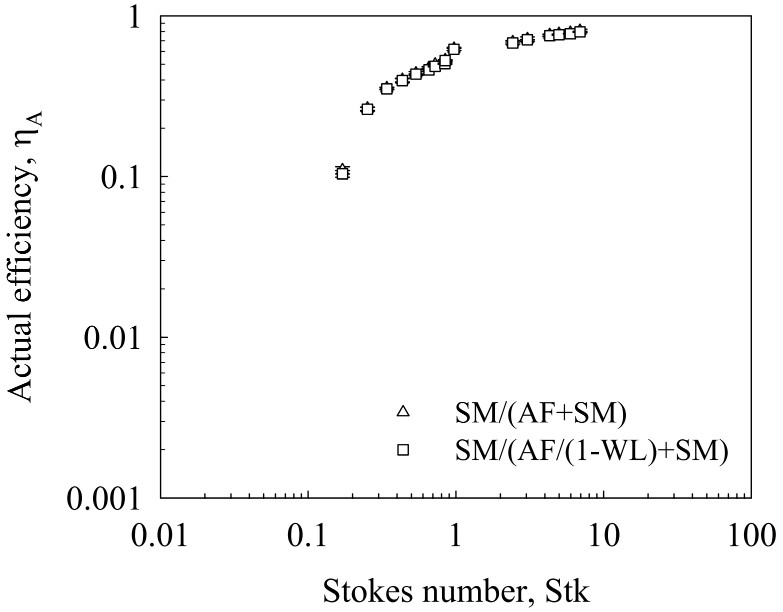

Figure 4.21. Actual efficiency as a function of Stokes number for perforated-sheet screen (0.015-inch, 0.21).

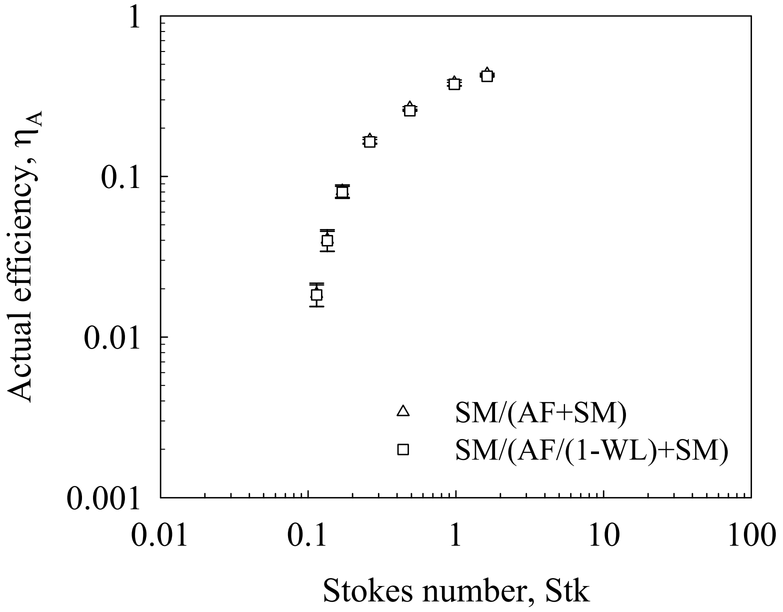

Figure 4.22. Actual efficiency as a function of Stokes number for perforated-sheet screen (0.1875-inch, 0.51).

efficiency, corrected from the aerosol collection in the screen, and it is compared between with wall loss and without wall loss, calculated by means of Equations (4-3 and 4-5). The actual efficiency is plotted as a function of Stokes number for each screen. It is seen that in all cases, the curves are similar in shape, but the slope of each curve is dependent on the fraction of open area (f_{OA}). The efficiency increases with increasing Stokes number which is a function of particle diameter, face velocity and characteristic length (d_C). The increase in efficiency with increasing particle size or face velocity can be explained by the dominance of the inertial impaction collection mechanism where large particles are collected more efficiently due to their high inertial parameter (Stokes number). Two of the most important practical problems in screen filtration studies are to predict the maximum and minimum efficiencies and the corresponding Stokes numbers. In all cases, the maximum actual efficiency is almost close to the solidity value of each screen as the Stokes number is increased. Further discussions of these results will be also made in Chapter VI.

Discussion of Errors

Tables 4.4 to 4.6 summarize predicted uncertainties that may occur in experimental tests through the Kline and McClintock method (1953).

Uncertainty Evaluation by Klein/McClintock

$$Y=Y(X_1, X_2, X_3,\ldots) \qquad (4\text{-}6)$$

Here, Y: results (e.g., relative concentration), X_i: measured variables (e.g., raw fluorometer reading in arbitrary units (m_f), volume of total solvent used to soak filters (V), volumetric air flow rate (Q), test duration (t)).

δX_i : variation of X_i (specified or estimated) (4-7)

$$\frac{\delta X_{\mathrm{i}}}{\mathrm{X_i}} = w_i : \text{uncertainty of } X_i \tag{4-8}$$

$$\delta Y_i = \frac{\partial Y}{\partial X_i} \delta X_i : \text{variation of } Y \text{ by } X_i \tag{4-9}$$

$$\frac{\delta Y_i}{Y} = \frac{1}{Y}\frac{\partial Y}{\partial X_i}\delta X_i = \frac{X_i}{Y}\frac{\partial Y}{\partial X_i}\frac{\delta X_i}{X_i} = \frac{X_i}{Y}\frac{\partial Y}{\partial X_i} w_i = w_{Y_i} \tag{4-10}$$

Overall uncertainty of Y by all X_i

$$w_Y = \pm\sqrt{w^2{}_{Y_1} + w^2{}_{Y_2} + \ldots} = \pm\sqrt{\left[\frac{X_1}{Y}\frac{\partial Y}{\partial X_1} w_1\right]^2 + \left[\frac{X_2}{Y}\frac{\partial Y}{\partial X_2} w_2\right]^2 + \ldots.} \tag{4-11}$$

A degree of uncertainty is related with data collected through experimental investigations such as systematic or bias errors and precision or random errors. In the experimental study, screen aerosol concentration (C_{SM}) and after-filter aerosol concentration (C_{AF}) were determined using Equation (4-8). Applying the concept of Kline and McClintock method gives:

$$w_{C_{SM}} = \pm\sqrt{\left[\frac{m_f}{C_{SM}}\frac{\partial C_{SM}}{\partial m_f}\frac{\delta m_f}{m_f}\right]^2 + \left[\frac{V}{C_{SM}}\frac{\partial C_{SM}}{\partial V}\frac{\delta V}{V}\right]^2 + \left[\frac{Q}{C_{SM}}\frac{\partial C_{SM}}{\partial Q}\frac{\delta Q}{Q}\right]^2 + \left[\frac{t}{C_{SM}}\frac{\partial C_{SM}}{\partial t}\frac{\delta t}{t}\right]^2} \tag{4-12}$$

The overall uncertainty of the aerosol concentration can be estimated by incorporating individual uncertainties in the measurable quantities c_f, V, Q, and t. If the relative errors in these parameters (c_f, V, Q, t) for relative concentration are estimated to be ±5%, ±2.5%, ±2.5%, ±0.4%, respectively, the overall uncertainty of the screen aerosol concentration (C_{SM}) is calculated to be ±6.1% using these values in Equation (4-11). Using the same concept, the overall uncertainties of the after-filter aerosol concentration (C_{AF}) are estimated to be the same value for the screen aerosol concentration (C_{SM}).

If we rewrite the collection efficiency as,

$$\eta_A = \frac{C_{SM}}{C_{SM} + C_{AF}} \tag{4-13}$$

The relative error in collection efficiency is calculated to be ±8.6%:

$$w_E = \pm\sqrt{\left[\frac{\delta C_{SM}}{C_{SM}}\right]^2 + \left[\frac{\delta C_{AF}}{C_{AF}}\right]^2} \tag{4-14}$$

The uncertainty in the physical particle diameter (d_p) which is given by the ratio of the particle diameter measured (d_m) under the microscope to the flattering factor (f) of the droplet which is a mixture of oleic acid and sodium fluorescien is given by:

$$w_{d_P} = \pm\sqrt{\left[\frac{\delta d_m}{d_m}\right]^2 + \left[\frac{\delta f}{f}\right]^2} \tag{4-15}$$

It is estimated that $\delta d_m/d_m$ has ±2.9%, ±1.7%, ±1.2% and ±1.1% for 1-5 µm, 6-10 µm, 11-15 µm and <16 µm particle sizes, respectively, and $\delta f/f$ has ±3% as determined by an approach similar to that by Olan-Figueroa et al. (1982). The overall uncertainty in particle size determination, given by Equation (4-11), is ±4.2%, ±3.4%, ±3.2% and ±3.2% for 1-5 µm, 6-10 µm, 11-15 µm and <16 µm AD particle sizes, respectively. Additional important parameters that require the estimation of uncertainty is the Stokes number. If we rewrite the Stokes number as,

$$Stk = \frac{C_c \cdot \rho_p \cdot d_p{}^2 \cdot U_o}{18 \cdot \mu \cdot d_c} = \frac{(1 + \frac{2.34 \cdot \lambda}{d_p}) \cdot \rho_p \cdot d_p{}^2 \cdot U_o}{18 \cdot \mu \cdot d_c} \tag{4-16}$$

The relative error in calculating the Stokes number for a given particle size may be expressed as:

$$w_{Stk} = \pm\sqrt{\left[\left(\frac{2\cdot d_p + 2.34\cdot\lambda}{d_p + 2.34\cdot\lambda}\right)\frac{\delta d_p}{d_p}\right]^2 + \left[\frac{\delta U_o}{U_o}\right]^2 + \left[\frac{\delta d_c}{d_c}\right]^2} \tag{4-17}$$

The relative errors in the particle size d_p are given by the above calculation for each particle size, while the errors associated in measuring the velocity U_o is estimated to be ±2.5%. The total uncertainty in the calculated value of the Stokes number is presented in Tables 4.4 to 4.6 based on the error related in measuring the characteristic length (wire diameter and effective slack length) for each screen (electroformed-wire, woven-wire, and perforated-sheet).

Table 4.4. The total predicted uncertainty in the calculated value of Stokes number for electroformed-wire.

Particle Size (AD μm)	$\delta dp/dp$	$\delta U_o/U_o$	$\delta d_c/d_c$	w_{stk}
1 to 5 μm	4.2%	2.5%	3.0%	7.7%
6 to10 μm	3.4%	2.5%	3.0%	7.4%
11 to15 μm	3.2%	2.5%	3.0%	7.2%
< 16 μm	3.2%	2.5%	3.0%	7.3%

Table 4.5. The total predicted uncertainty in the calculated value of Stokes number for woven-wire.

Particle Size (AD µm)	$\delta dp/dp$	$\delta U_o/U_o$	$\delta d_c/d_c$ $d_w < 0.005$-inch	w_{stk}	$\delta d_c/d_c$ $0.005 \leq d_w \leq 0.01$	w_{stk}	$\delta d_c/d_c$ $d_w > 0.01$	w_{stk}
1 to 5 µm	4.2%	3%	2.1%	7.4%	3.5%	7.9%	2.5%	7.5%
6 to10 µm	3.4%	3%	2.1%	7.0%	3.5%	7.6%	2.5%	7.2%
11 to15µm	3.2%	3%	2.1%	6.9%	3.5%	7.4%	2.5%	7.0%
< 16 µm	3.2%	3%	2.1%	6.9%	3.5%	7.5%	2.5%	7.1%

Table 4.6. The total predicted uncertainty in the calculated value of Stokes number for perforated-sheet.

Particle Size (AD µm)	$\delta dp/dp$	$\delta U_o/U_o$	$\delta d_c/d_c$	w_{stk}
1 to 5 µm	4.2%	2.5%	3.0%	7.7%
6 to10 µm	3.4%	2.5%	3.0%	7.4%
11 to15 µm	3.2%	2.5%	3.0%	7.2%
< 16 µm	3.2%	2.5%	3.0%	7.3%

CHAPTER V

NUMERICAL STUDIES

Three-dimensional numerical simulations corresponding to the various experimental investigations were conducted using commercial computational fluid dynamics (CFD) software, Fluent (version 6.1.22), as a tool. The deposition process was modeled as a dilute and disperse two-phase flow problem under the Eulerian-Lagrangian framework, with an assumed one-way coupling between the phases. This implies that a convergent flow field is first obtained for the domain of interest and aerosol particles are released at appropriate locations and their trajectories computed as a post-processing operation, to determine deposition on the screen. The predicted numerical results were then compared with the experimental results.

Different configurations were investigated in scoping simulations with the appropriate boundary conditions to determine the right combination of configuration and boundary conditions (computational model), that is a proper numerical representation of the aerosol particle deposition process on a screen. Figure 5.1 shows the different models that were investigated. The computational model deduced from the results of the scoping simulations was used as the base model for subsequent investigations.

A block-structured body-fitted coordinate system was used for discretization of the simulation domain to suit the nature of the domain and a structured, hexahedral grid was generated on the domain. The total number of nodes was different depending on each screen configuration in this study. Gambit (the topology-generating a grid-

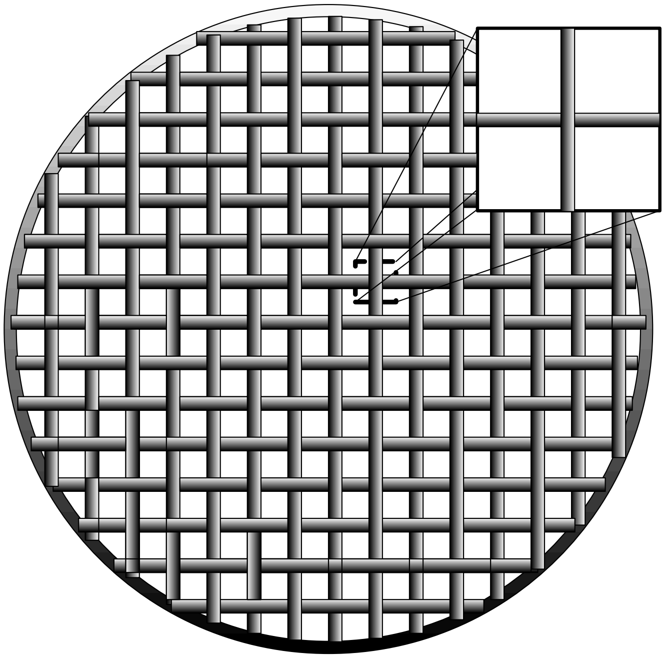

(a) Wire screen

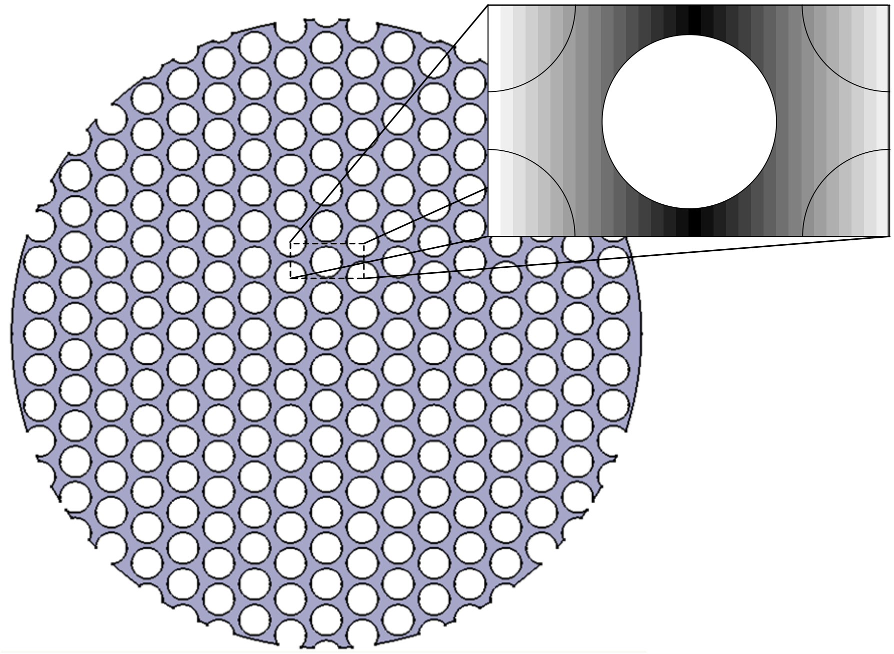

(b) Perforated-sheet screen

Figure 5.1. Schematic for the idealization of numerical analysis on the screen.

generating module of Fluent) was used to create the mesh which consisted of 1.8 to 2.2 million computational nodes. Effect of different solution algorithms for the pressure-velocity coupling such as SIMPLE, SIMPLEC (SIMPLE-Consistent), PISO, and different discretization schemes for the convective terms on the resolution of the flow-field and the consequent impact on the particle deposition process were analyzed. The acronym SIMPLE stands for Semi-Implicit Method for Pressure-Linked Equations (Patankar 1980). The condition of convergence, called residuals, was selected as 1×10^{-5} of the overall conservation of the flow properties.

Flow Field Simulation

The flow field is setup through the use of Fluent. The continuity equation used for steady state, incompressible, Newtonian flow is:

$$\frac{\partial(u_i)}{\partial x_i}=0 \tag{5-1}$$

Here, u_i is the flow velocity in the i^{th} direction.

The momentum equation is given as:

$$\frac{\partial(\rho u_i u_j)}{\partial x_i}=-\frac{\partial P_s}{\partial x_i}+\frac{\partial}{\partial x_i}\left[\mu(\frac{\partial u_i}{\partial x_j}+\frac{\partial u_j}{\partial x_i})\right] \tag{5-2}$$

where P_s is the static pressure.

In viscous flows, the no-slip boundary condition is imposed by default on all wall surfaces in the computational grid. A uniform velocity profile is specified at the inlet, based on the experimental conditions. As shown in Figure 5.2, a channel is isolated for

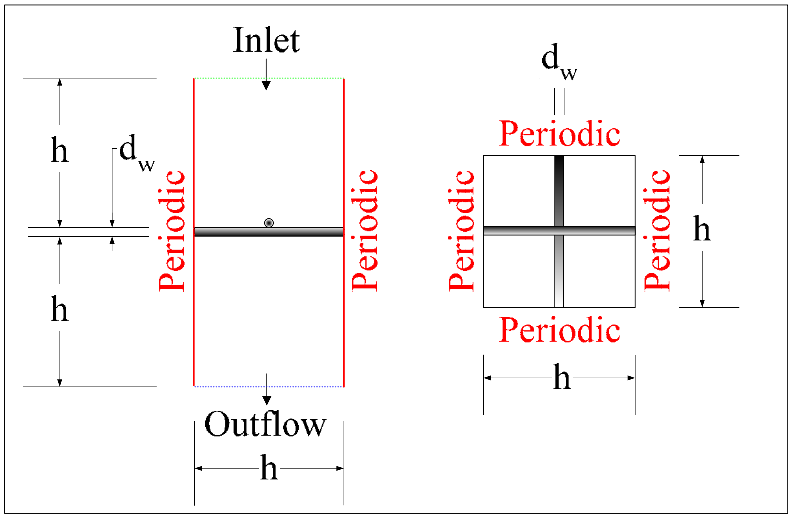

(a) Wire screen

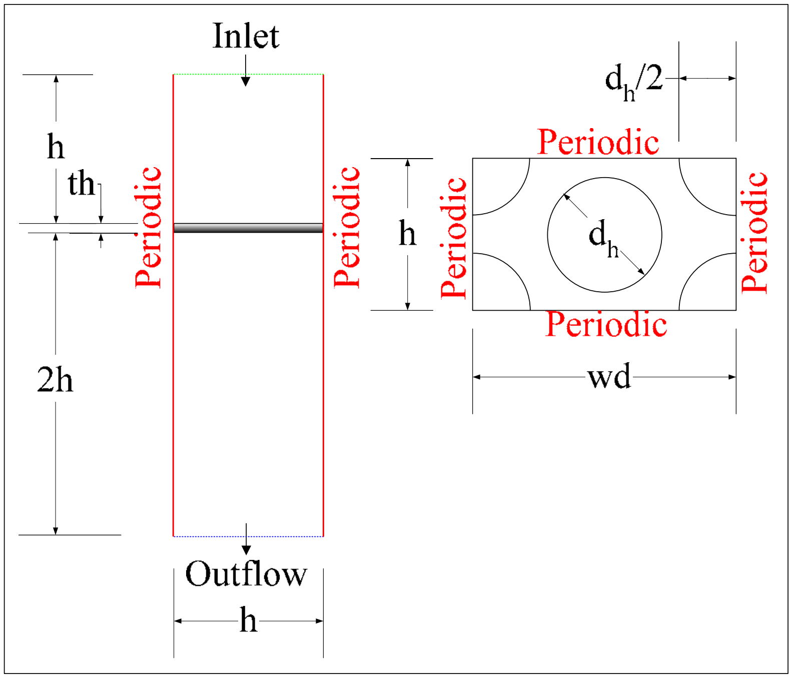

(b) Perforated-sheet screen

Figure 5.2. Schematic of the numerical setup used to study the screen deposition process.

analysis purposes by employing periodic boundary conditions at the interfaces with the neighbor channels. Outflow boundary conditions in Fluent are imposed to model flow exits, where the details of the flow velocity and pressure are not known prior to solution of the flow problem. With this boundary condition, no other conditions are needed at the outflow boundaries: Fluent extrapolates the required information from the interior of the flow field.

Particle Tracking Methodology

In addition to solving transport equations for the continuous phase, Fluent allows simulation of a discrete second phase in a Lagrangian frame of reference. This second phase consists of spherical aerosol particles. Coupling between the phases and its impact on both the discrete phase trajectories and the continuous phase flow can be included.

The trajectory of a particle is predicted through the use of Newton's equation with time integration of the forces acting on the particle, and is written in a Lagrangian reference frame, i.e.:

$$\frac{du_v}{dt} = F_D(u_u - u_v) + \frac{g_i(\rho_p - \rho)}{\rho_p} \tag{5-3}$$

Here, u_v is the particle velocity, and F_D is the drag force on the particle and is given by

$$F_D = \frac{1}{2}\rho C_D(\frac{\pi}{4}d_P{}^2)\rho(\overrightarrow{u_u} - \overrightarrow{u_v})|u_u - u_v| \tag{5-4}$$

Re_p is the particle Reynolds number and is expressed as:

$$\mathrm{Re}_p = \frac{\rho d_p \left| u_v - u_u \right|}{\mu} \tag{5-5}$$

The particle drag coefficient, C_D is a function of the particle Reynolds number.

$$C_D = f(Re_p) \tag{5-6}$$

Once the particle velocity components are calculated using the above equations, particle trajectories can be obtained by solving:

$$\frac{dx_v}{dt} = u_v \tag{5-7}$$

Numerical Results

Physical conditions pertaining to numerical simulations performed in this study are presented in Table 5.1, which summarizes the tested particle sizes, flow rates (*Q*), flow Reynolds number (*Re*), characteristic length Reynolds number (Re_C), interception parameter (*R*) and Stokes number (*Stk*) ranges.

Results of scoping simulations performed to determine the appropriate base configuration, along with details of the different model configurations investigated are presented in Figure 5.3, for the reference screen material of two different wire diameters and fraction of open area (a. 20×20 mesh size, $d_w = 65$ µm, $f_{OA} = 0.90$, b. 64×64 mesh size, $d_w = 114$ µm, $f_{OA} = 0.51$) at a wire Reynolds number of 1.0, and compared against experimental data. The total number of nodes was 1.5 million to 2.1 million depending on the model configuration. It is evident from Figure 5.3 that predictions obtained for Model-II-B are in very good agreement to experimental data, compared to the other models. Hence, Model-II-B was chosen as the base configuration for the present study.

Table 5.1. Operation condition of numerical simulations for each screen.

	Screen Type	**Wire diameter Hole diameter** (dw or d_h) inch	μm	**Fraction of Open Area** (f_{OA}) %	**Mesh Size** (M)	**Particle size** **AD** μm	***Q*** Min-Max L/min	***Re*** Min-Max	***Re*** $_C$ Min-Max	***R*** Min-Max	***Stk*** Min-Max
1	Electroformed	0.00629	160	56.0	40	4-20	164-1644	1542-15424	3-30	0.025-0.125	0.51-12.29
2	Electroformed	0.00268	68	75.0	50	4-20	86-861	808-8080	0.5-5	0.059-0.294	0.49-15.11
3	Electroformed	0.00138	35	88.0	45	3-20	78-1960	732-18392	0.5-5	0.057-0.571	0.54-20.34
4	Electroformed	0.00257	65	90.0	20	4-20	44-1080	408-10135	0.5-5	0.061-0.307	0.58-19.80
						3-20	44-1960	408-18392	0.5-30	0.025-0.571	0.49-20.34
1	Woven	0.01700	432	43.6	20	3-20	47-2368	444-22217	3-150	0.007-0.046	0.12-6.55
2	Woven	0.00450	114	50.7	64	4-20	69-693	651-6507	1-10	0.035-0.175	0.23-7.25
3	Woven	0.01800	457	50.7	16	2-20	52-2600	488-24399	3-150	0.007-0.044	0.08-6.79
4	Woven	0.00950	241	51.1	30	3-20	33-1655	311-15532	1-50	0.012-0.083	0.11-8.19
5	Woven	0.01600	406	55.4	16	3-20	64-3196	600-29994	3-150	0.007-0.049	0.13-9.39
6	Woven	0.01700	432	58.1	14	3-20	63-3155	592-29605	3-150	0.007-0.046	0.11-8.73
7	Woven	0.00950	241	71.9	16	3-20	140-2329	1311-21854	3-50	0.017-0.083	0.34-9.35
						2-20	33-3196	311-29994	1-150	0.007-0.175	0.08-9.39
1	Welded	0.01700	432	74.6	8	3-20	270-2700	2534-25342	10-100	0.007-0.046	0.15-7.47
1	Perforated	0.01500	381	21.0	N/A	3-20	81-2423	758-22739	10-341	0.007-0.047	0.16-6.80
2	Perforated	0.18750	4763	51.0	N/A	6-20	502-2510	4712-23562	115-575	0.003-0.011	0.15-1.64
						3-20	81-2510	758-23562	10-575	0.003-0.047	0.15-6.80

*Note: Grey highlight is for the overall ranges for each screen.

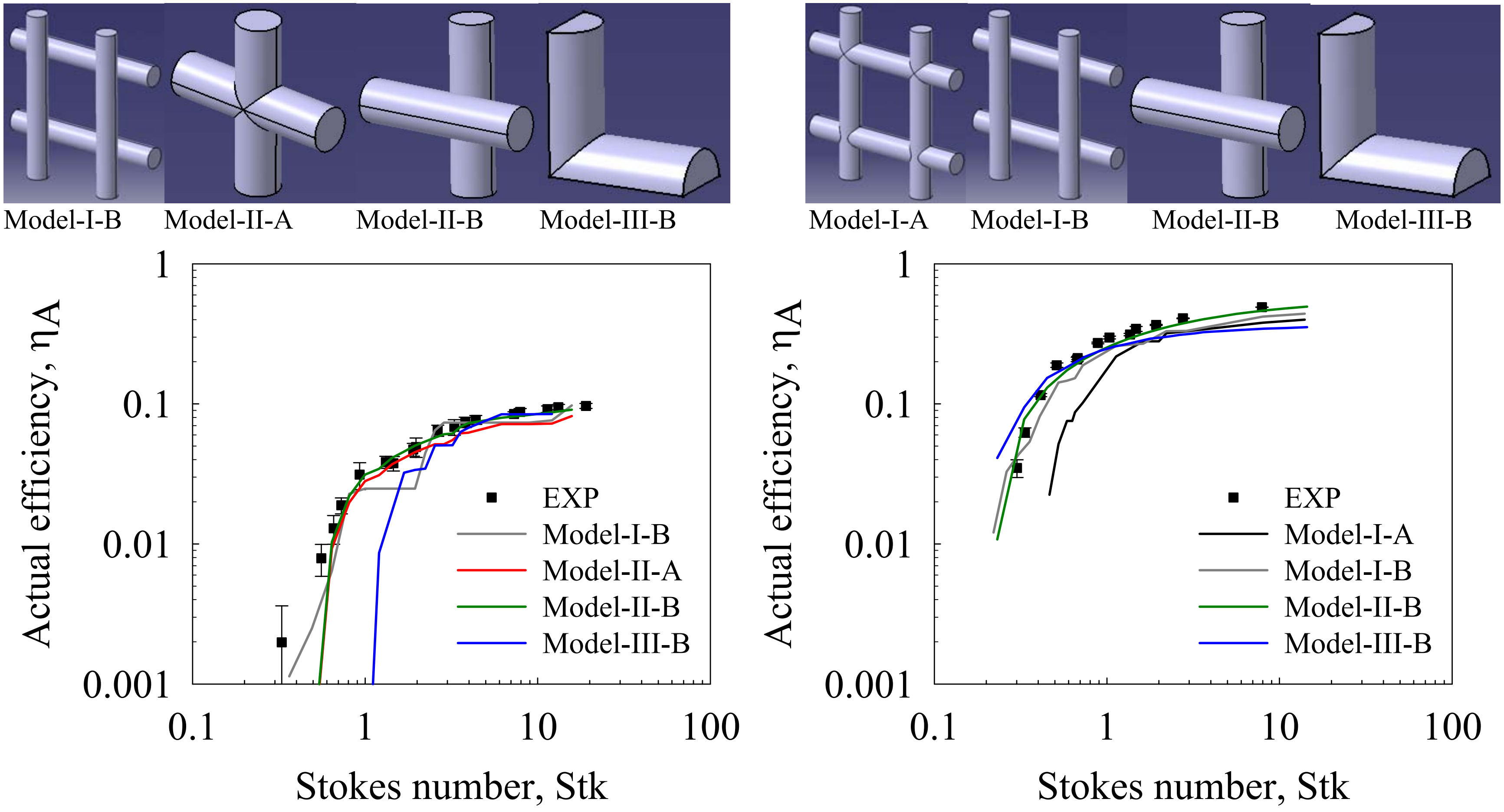

(a) 20×20 mesh size, d_w = 65 µm, f_{OA} = 0.90

(b) 64×64 mesh size, d_w = 114 µm, f_{OA} = 0.51

Figure 5.3. Result of the numerical model iteration.

Additionally in Figure 5.4, the comparison of collection efficiency between the ideal model (with symmetric BC's) and the actual model (with symmetric BC's) was carried out with one of the woven-wires (14×14-mesh size, $d_w = 0.017$-inch, $f_{OA} = 0.581$).

For 14 screens (4 electroformed-wire, 7 woven-wire, 1 welded-wire screen and 2 perforated-sheet screens), the actual efficiency calculations were made with particle sizes ranging from 2 to 20 μm and Stokes number ranging from 0.08 to 20.34. The actual efficiency is plotted as a function of particle size for different Reynolds numbers (Re_C) and as a function of Stokes number, as shown in Figures 5.5 through 5.18.

It is seen that in all cases the curves are similar in shape and the log-log plot of actual efficiency against particle size leads to a curve whose slope and critical particle size both depend on characteristic length Reynolds number. The minimum particle size decreases with increasing Reynolds number, showing the increasingly important role of the inertial impaction mechanisms. There are certain very interesting features to be observed from the presented results. The obtained results show that the same Stk values lead to the same collection behavior on the screen. This emphasizes that characteristic length Reynolds number is not a unique parameter to describe the collection behavior in that regime. These results will be discussed further when comparison with the experimental results is made.

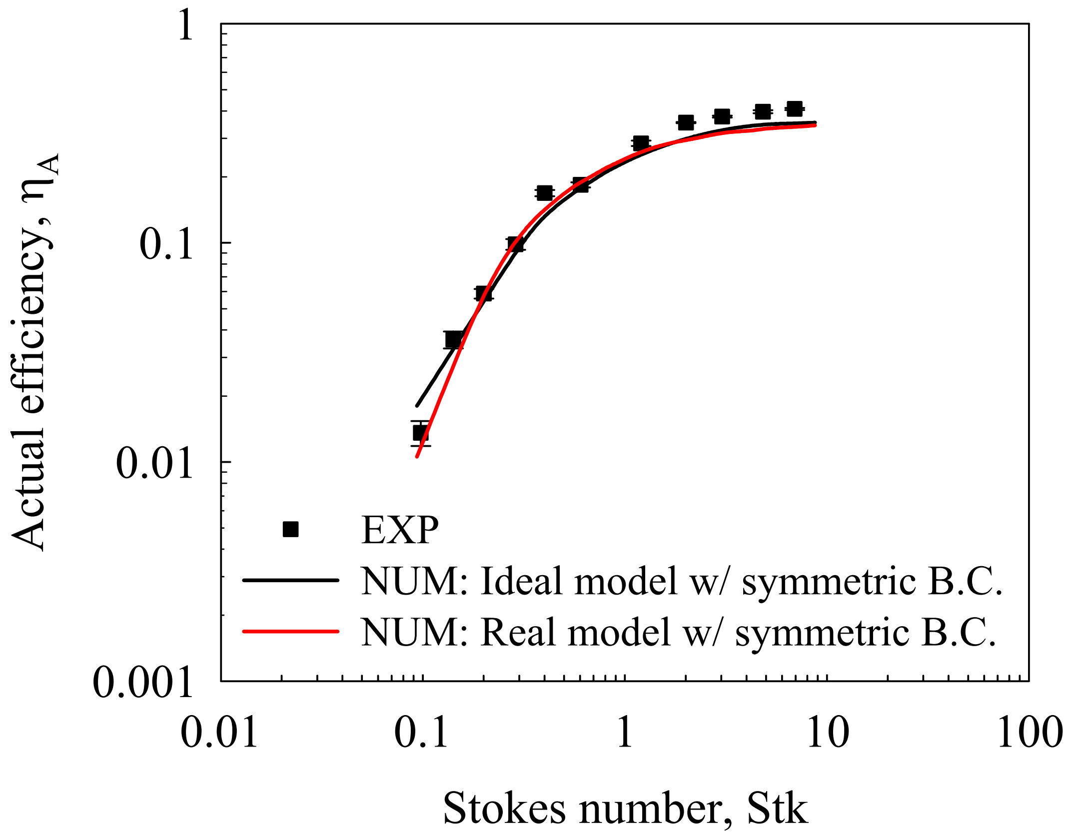

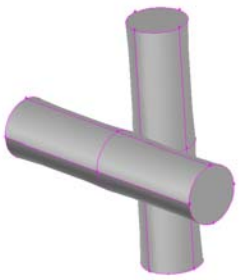

(a) Ideal model

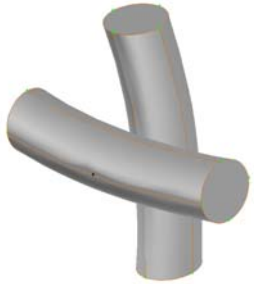

(b) Real model

Figure 5.4. Comparison of efficiency as a function of Stokes number between the ideal model (with symmetric boundary condition) and the real model (with symmetric boundary condition) of numerical simulation with one of woven-wire screen (14×14 mesh, d_w = 0.017-inch, f_{OA} = 0.581).

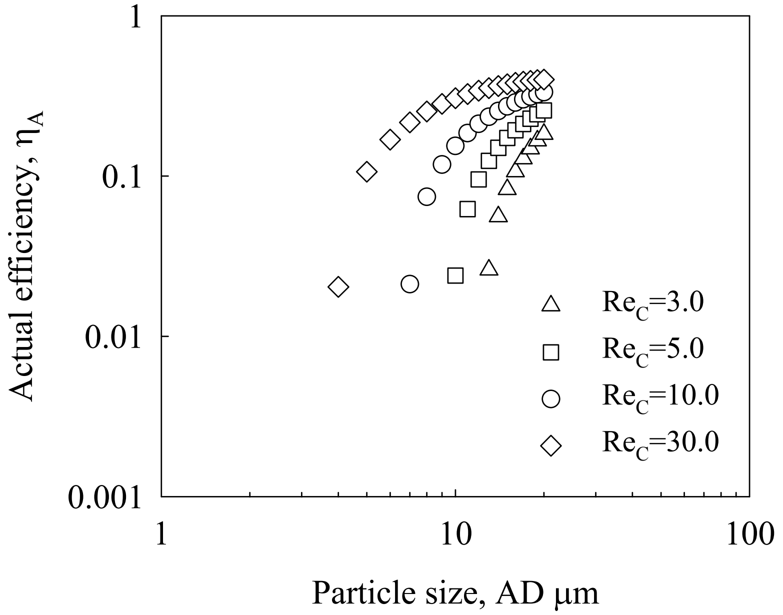

(a) η_A vs. Particle size (AD μm)

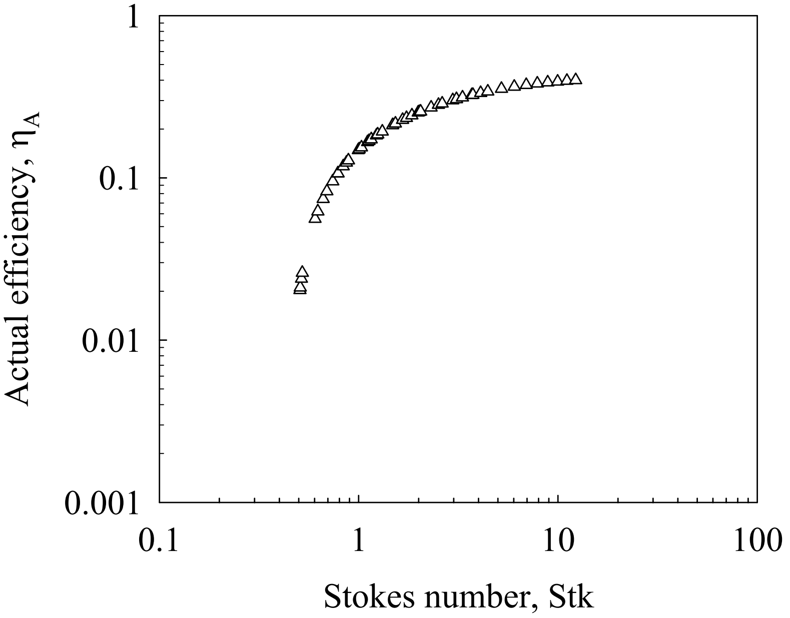

(b) η_A vs. *Stk*

Figure 5.5. Actual efficiency as a function of (a) particle size (AD μm), (b) Stokes number (*Stk*) for electroformed-wire screen (40×40, 0.00629-inch, 0.56).

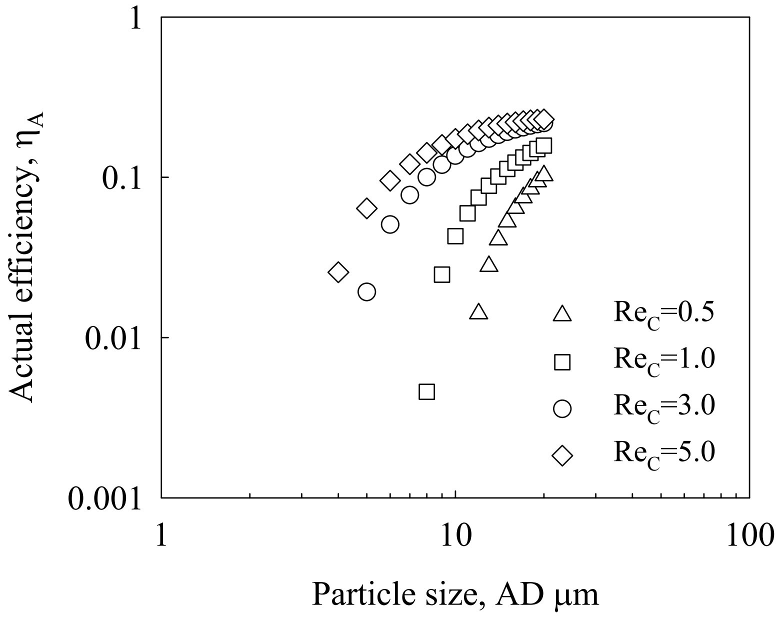

(a) η_A vs. Particle size (AD µm)

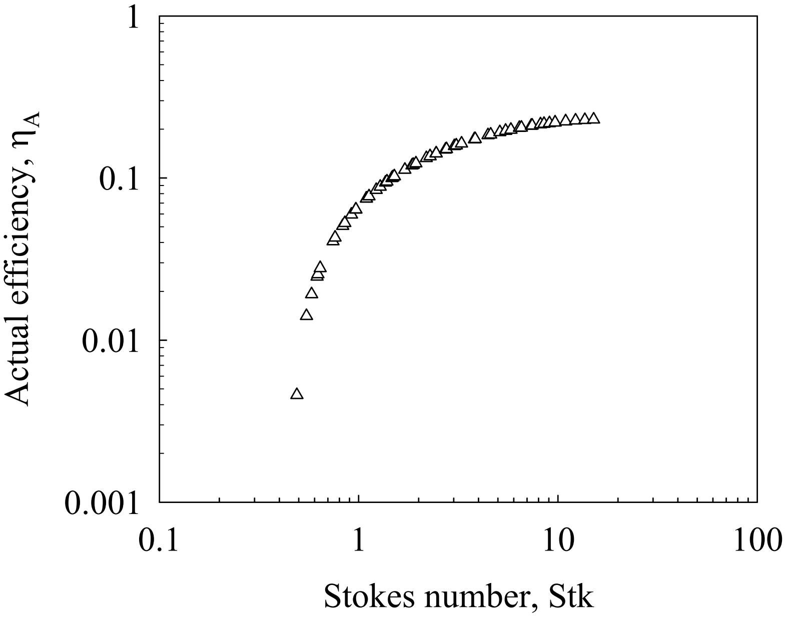

(b) η_A vs. *Stk*

Figure 5.6. Actual efficiency as a function of (a) particle size (AD µm), (b) Stokes number (*Stk*) for electroformed-wire screen (50×50, 0.00268-inch, 0.75).

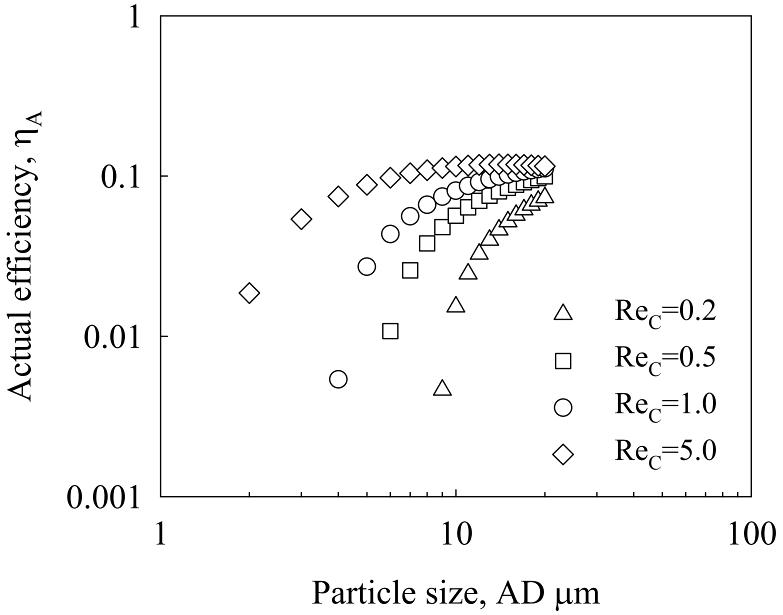

(a) η_A vs. Particle size (AD µm)

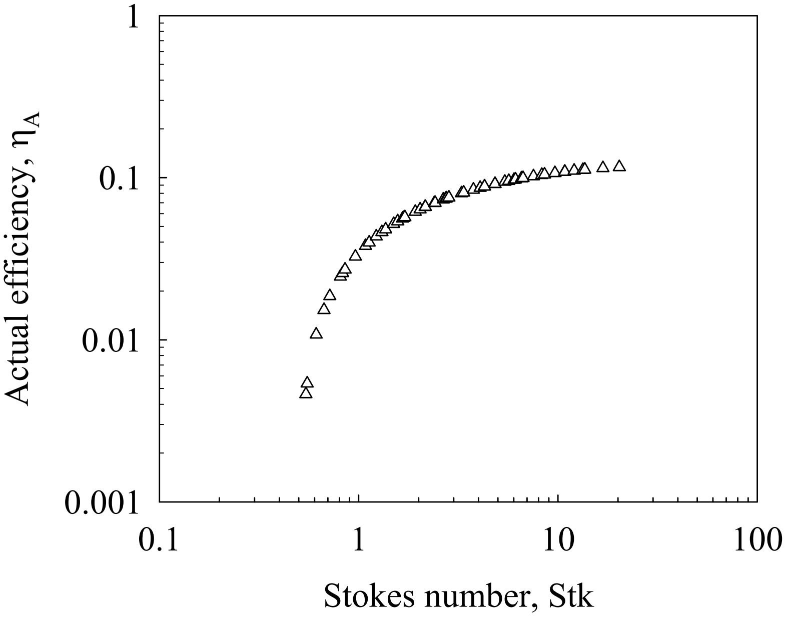

(b) η_A vs. *Stk*

Figure 5.7. Actual efficiency as a function of (a) particle size (AD µm), (b) Stokes number (*Stk*) for electroformed-wire screen (45×45, 0.00138-inch, 0.88).

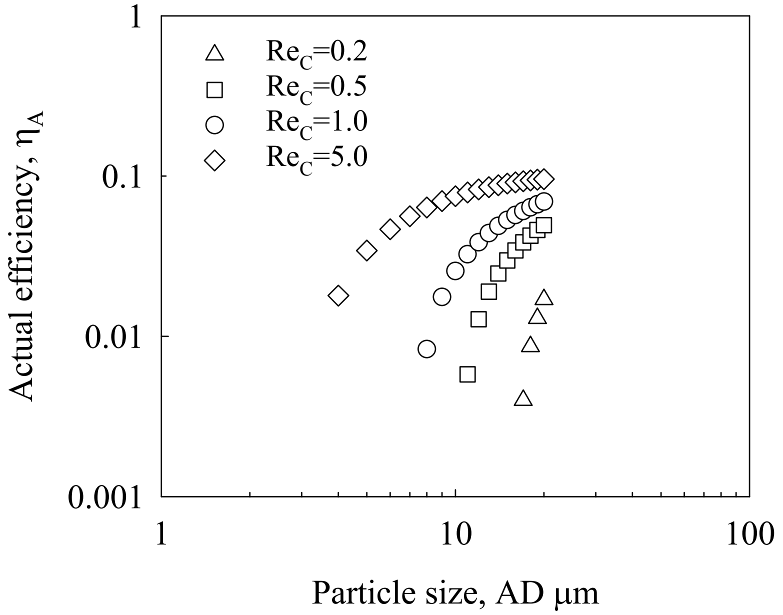

(a) η_A vs. Particle size (AD μm)

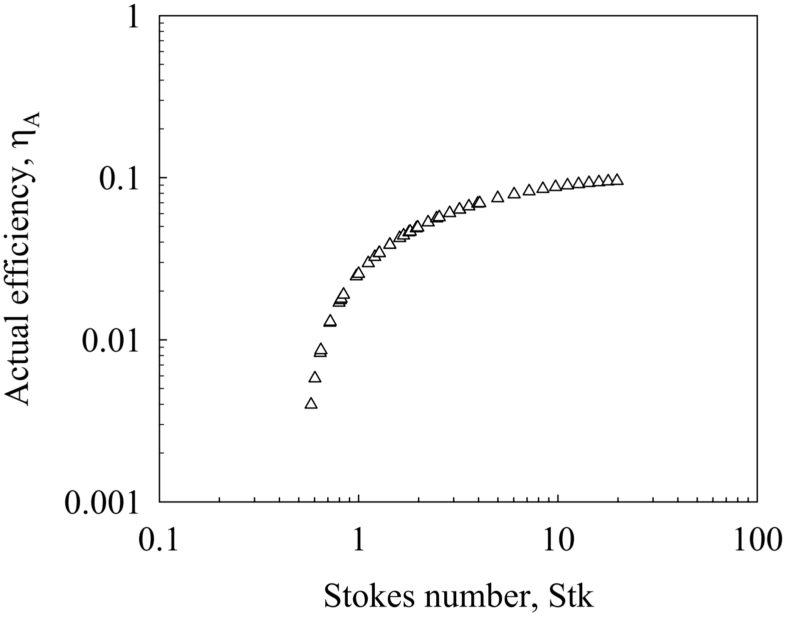

(b) η_A vs. *Stk*

Figure 5.8. Actual efficiency as a function of (a) particle size (AD μm), (b) Stokes number (*Stk*) for electroformed-wire screen (20×20, 0.00257-inch, 0.90).

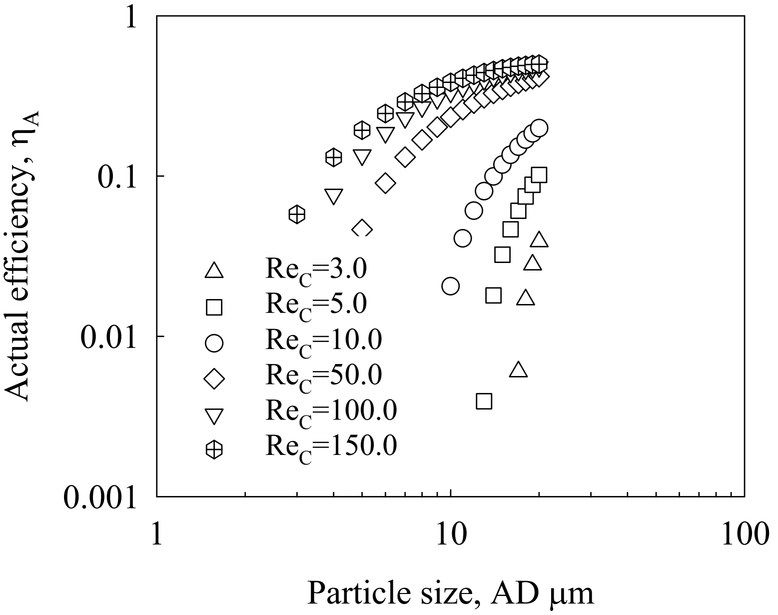

(a) η_A vs. Particle size (AD μm)

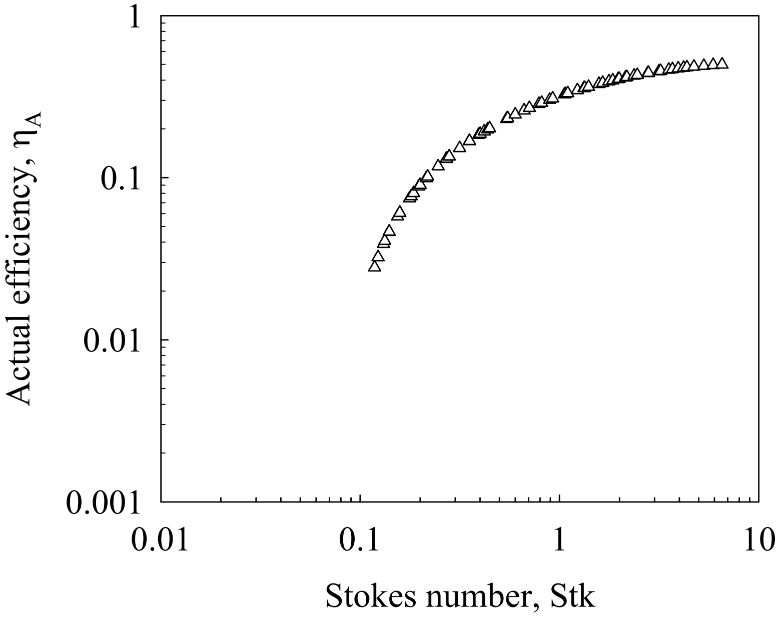

(b) η_A vs. *Stk*

Figure 5.9. Actual efficiency as a function of (a) particle size (AD μm), (b) Stokes number (*Stk*) for woven-wire screen (20×20, 0.017-inch, 0.436).

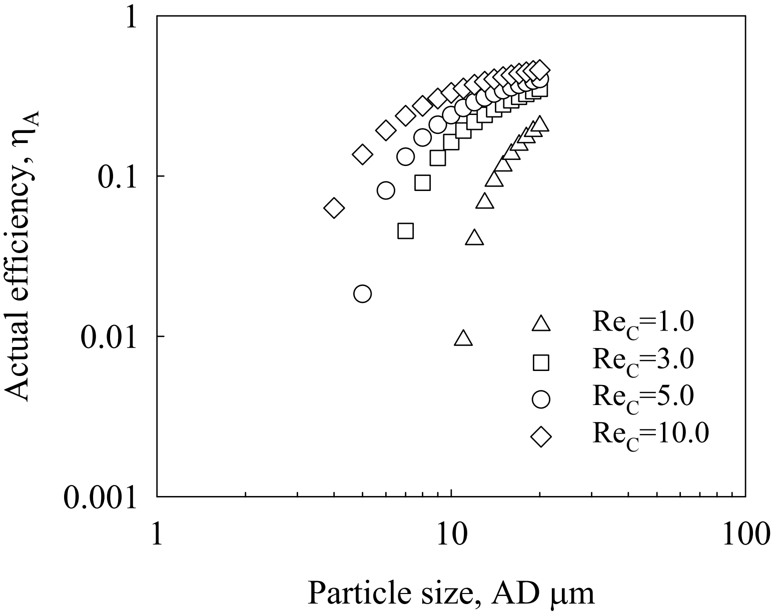

(a) η_A vs. Particle size (AD μm)

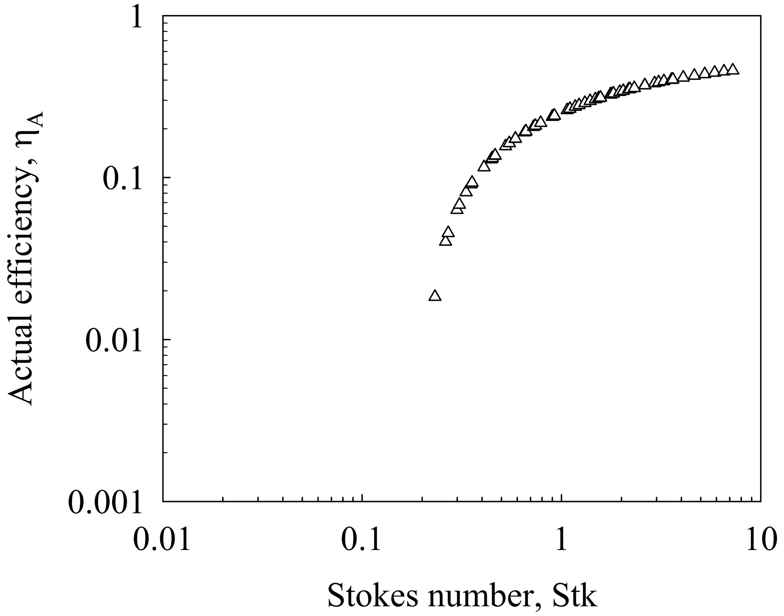

(b) η_A vs. *Stk*

Figure 5.10. Actual efficiency as a function of (a) particle size (AD μm), (b) Stokes number (*Stk*) for woven-wire screen (64×64, 0.0045-inch, 0.507).

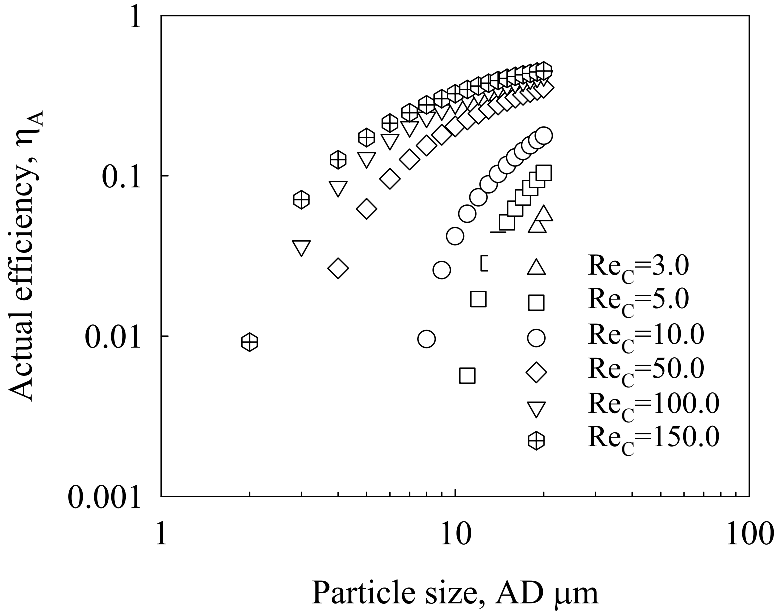

(a) η_A vs. Particle size (AD μm)

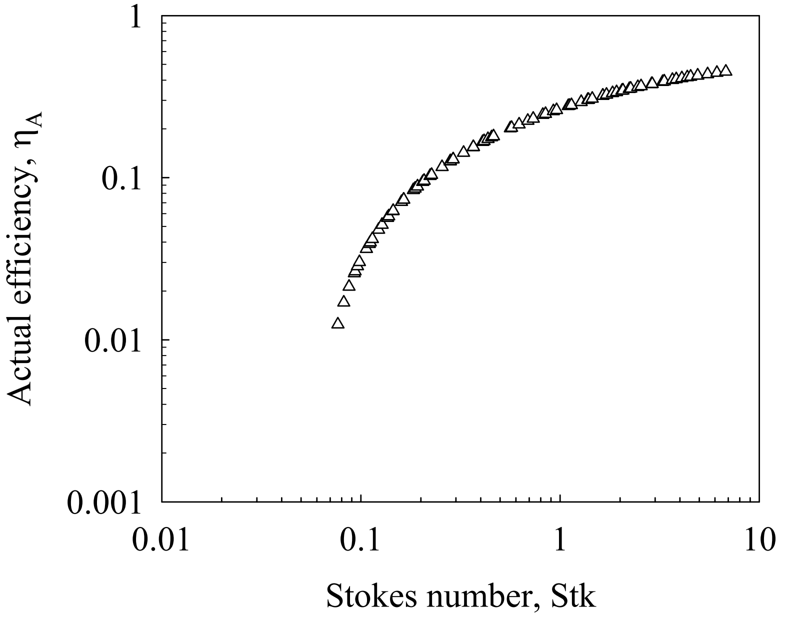

(b) η_A vs. *Stk*

Figure 5.11. Actual efficiency as a function of (a) particle size (AD μm), (b) Stokes number (*Stk*) for woven-wire screen (16×16, 0.018-inch, 0.507).

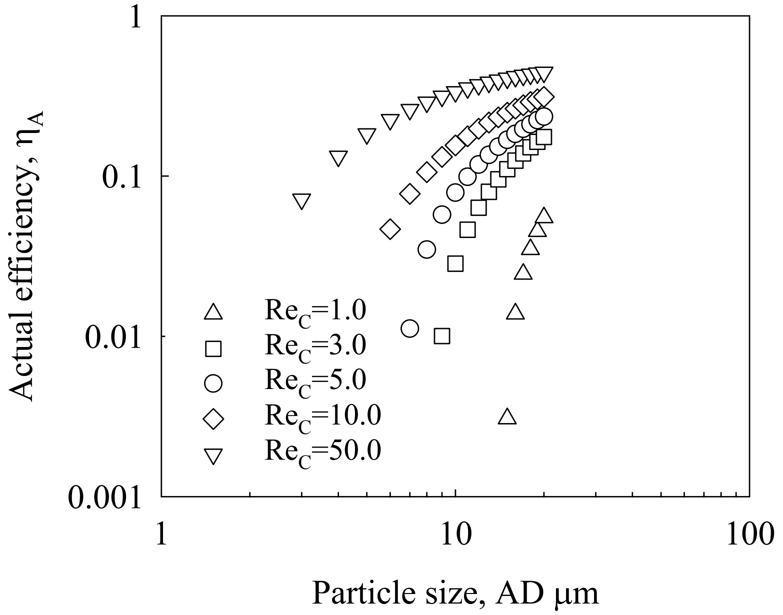

(a) η_A vs. Particle size (AD μm)

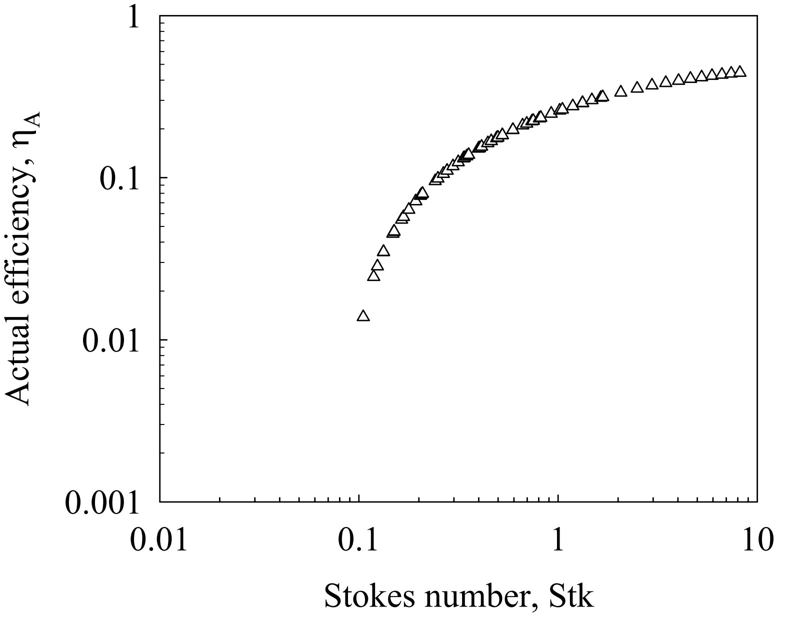

(b) η_A vs. *Stk*

Figure 5.12. Actual efficiency as a function of (a) particle size (AD μm), (b) Stokes number (*Stk*) for woven-wire screen (30×30, 0.0095-inch, 0.511).

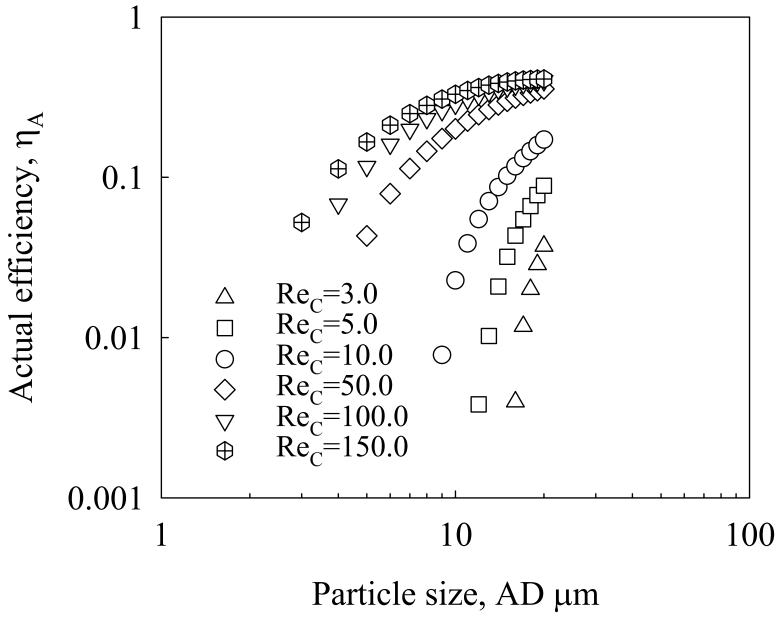

(a) η_A vs. Particle size (AD μm)

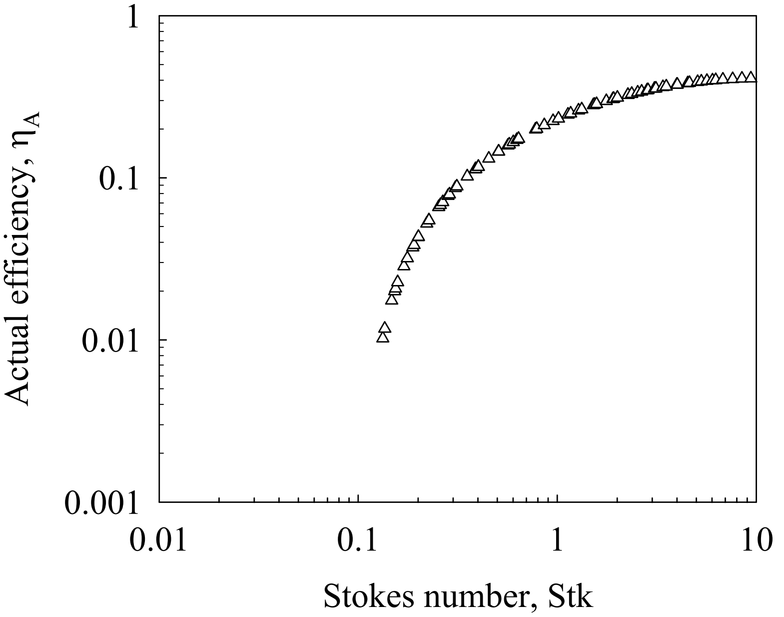

(b) η_A vs. *Stk*

Figure 5.13. Actual efficiency as a function of (a) particle size (AD μm), (b) Stokes number (*Stk*) for woven-wire screen (16×16, 0.016-inch, 0.554).

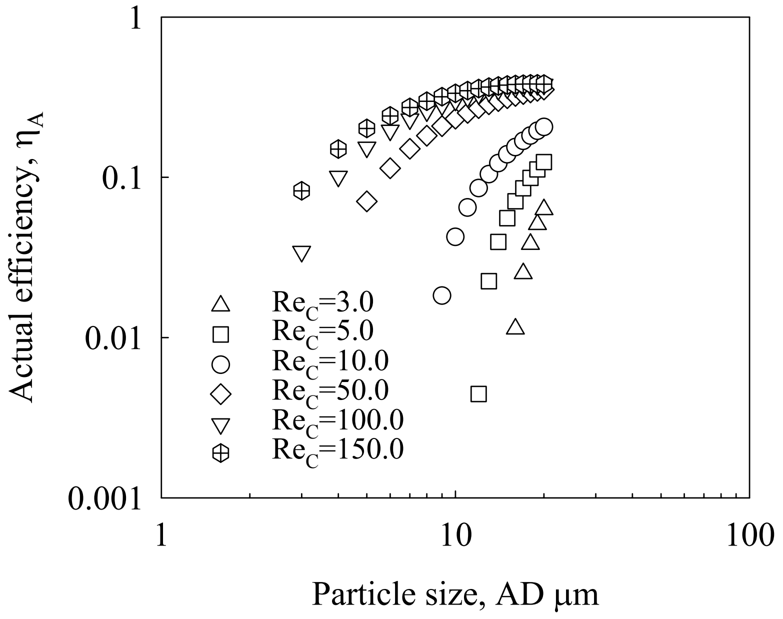

(a) η_A vs. Particle size (AD μm)

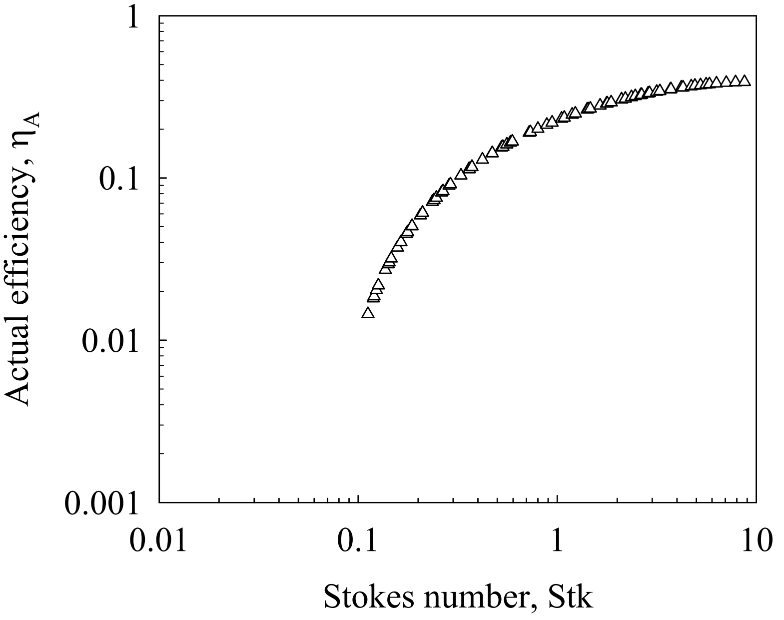

(b) η_A vs. *Stk*

Figure 5.14. Actual efficiency as a function of (a) particle size (AD μm), (b) Stokes number (*Stk*) for woven-wire screen (14×14, 0.017-inch, 0.581).

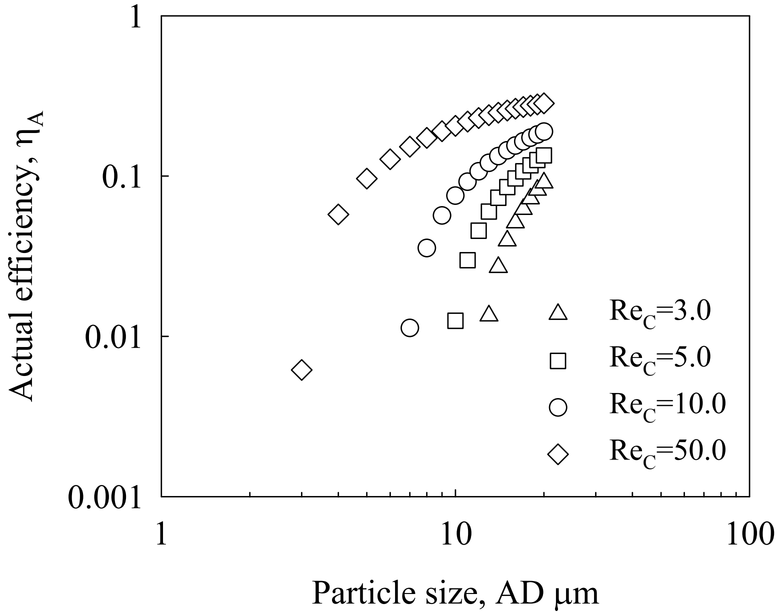

(a) η_A vs. Particle size (AD μm)

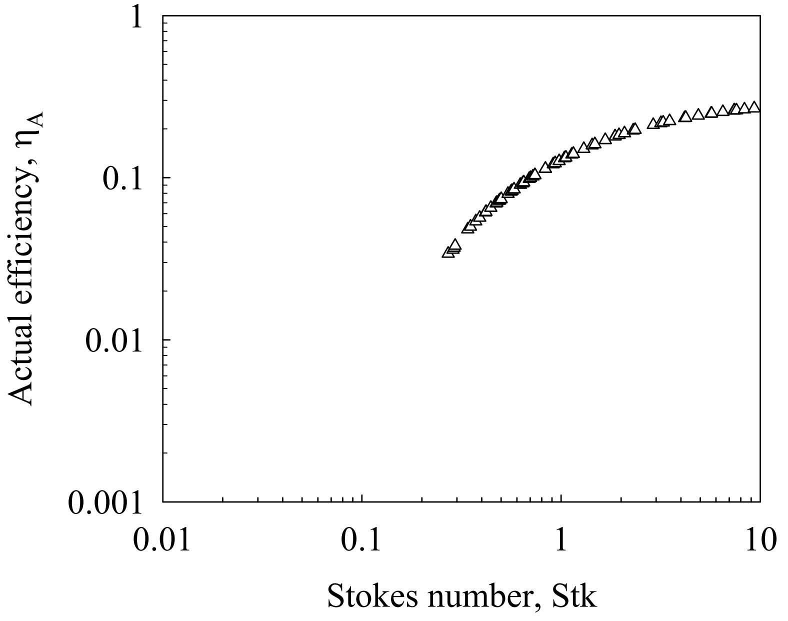

(b) η_A vs. *Stk*

Figure 5.15. Actual efficiency as a function of (a) particle size (AD μm), (b) Stokes number (*Stk*) for woven-wire screen (16×16, 0.0095-inch, 0.719).

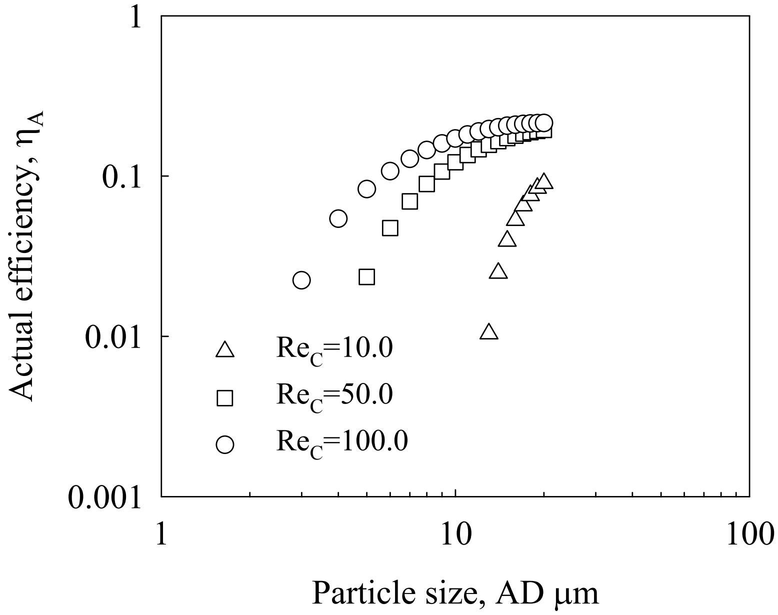

(a) η_A vs. Particle size (AD μm)

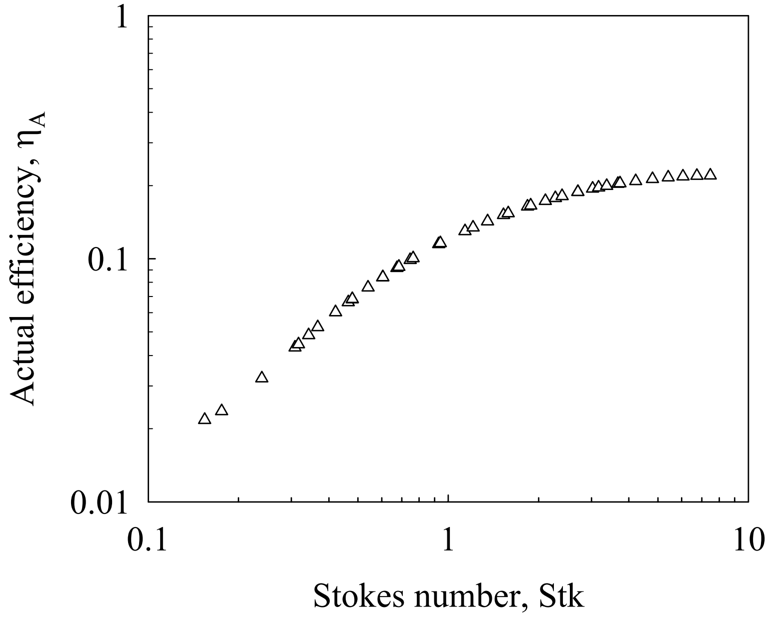

(b) η_A vs. *Stk*

Figure 5.16. Actual efficiency as a function of (a) particle size (AD μm), (b) Stokes number (*Stk*) for welded-wire screen (8×8, 0.017-inch, 0.746).

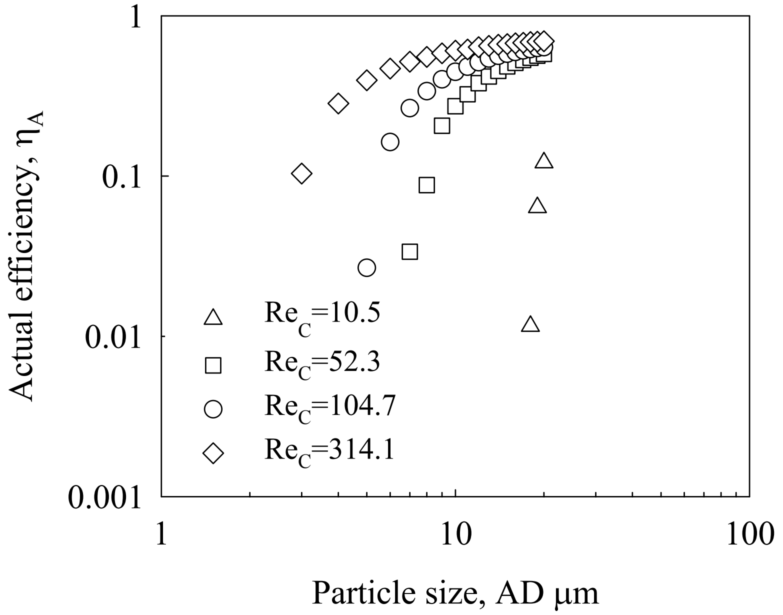

(a) η_A vs. Particle size (AD μm)

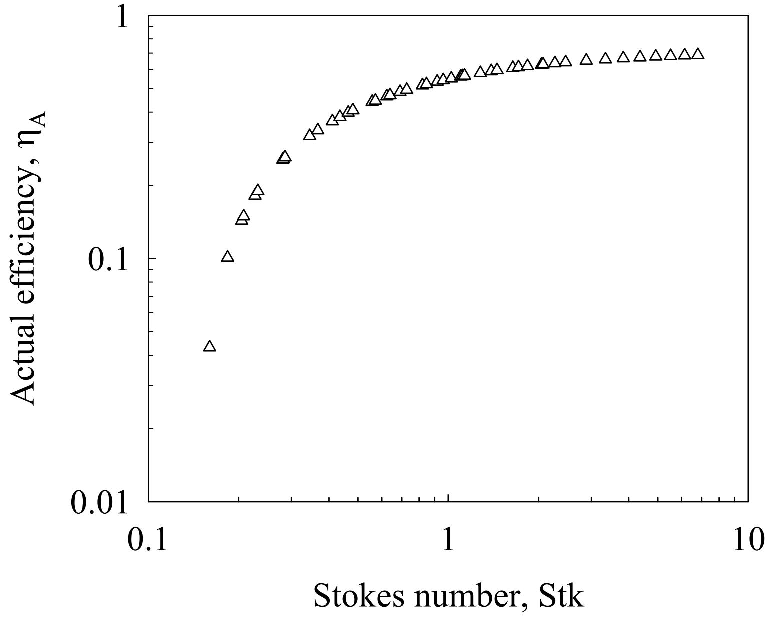

(b) η_A vs. *Stk*

Figure 5.17. Actual efficiency as a function of (a) particle size (AD μm), (b) Stokes number (*Stk*) for perforated-sheet screen (0.017-inch, 0.21).

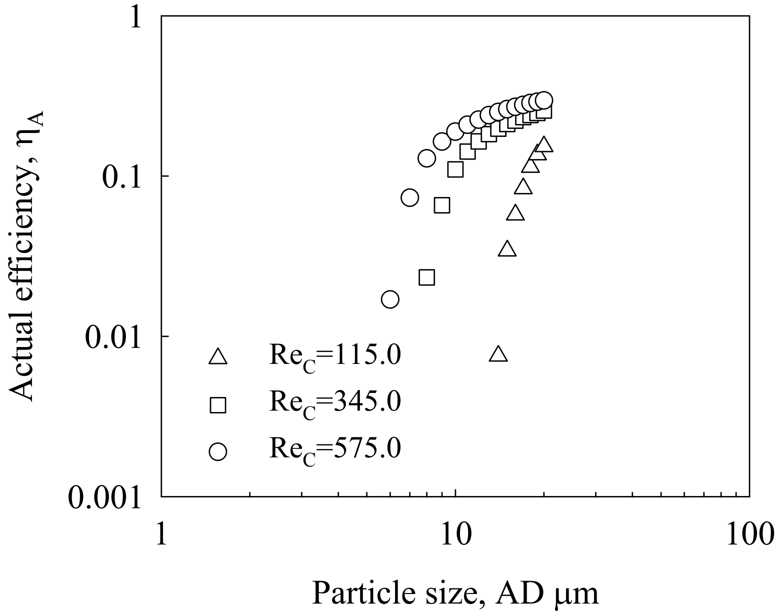

(a) η_A vs. Particle size (AD μm)

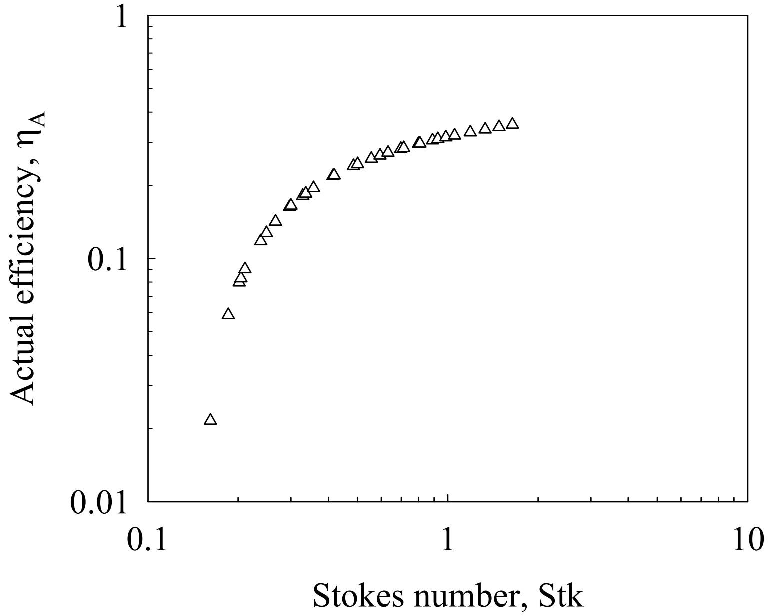

(b) η_A vs. *Stk*

Figure 5.18. Actual efficiency as a function of (a) particle size (AD μm), (b) Stokes number (*Stk*) for perforated-sheet screen (0.072-inch, 0.51).

CHAPTER VI

COMPARISON OF EXPERIMENTAL AND NUMERICAL STUDIES

It was seen in the previous chapter that in the process of short-listing the computational model to be used in the current research, we used experimental data as the basis for determination. The purpose of this chapter is to carry forward from that approach and compare the experimental and numerical results presented in the previous chapters (IV and V). The first comparisons are made on the basis of the actual efficiency and then the data collected during the experimental and numerical portions of this study are used to develop mathematical models. Multiple-regression analysis and curve fitting was used to develop the models by fitting experimental and numerical data and determining correlation coefficients. The first empirical models expressed the actual efficiency in terms of the solidity (α_A) and Stokes number (Stk). A theoretical methodology is subsequently developed based on the above data to standardize collection characteristics of each screen type, whereby, aerosol deposition is expressed as a function of non-dimensional parameters such as the interception parameter (R), Reynolds number (Re_C), and Stokes number (Stk), that govern the deposition. Further, experimental measurements and numerical predictions of pressure drop across the screen are used to develop models for the pressure coefficient in terms of the fraction of open area (f_{OA}) and Reynolds number.

Comparison with Actual Efficiencies

Both numerical and experimental studies have been conducted on electroformed-wire, woven-wire, welded-wire screens and perforated-sheet screens. Results for all the cases, presented as a log-log plot of the actual efficiency (η_A) against *Stk*, leads to a curve whose slope depend on the solidity (α_A). The plots are provided with bi-directional error bars for experimental measurements, where, vertical error bars represent the standard deviation in the estimated collection efficiency values, while the horizontal error bars represent the uncertainty involved in the calculation of Stokes number values (based on the discussion of errors in Chapter IV).

Figure 6.1 presents a direct comparison of the numerical predictions with experimental results for the 20×20 and 45×45 mesh screens, over a wide range of wire Reynolds numbers (0.5 to 30). It can be seen that the agreement is very good, indicating that the computations are able to reproduce the actual trend. The above results validate the accuracy of the numerical approach and indicate that the procedure can be used with confidence in the future research. Having validated the numerical procedure, simulations were performed to obtain predictions of collection characteristics of 40×40 and 50×50 mesh screens and the results are also presented in Figure 6.1.

Figure 6.2 shows comparisons of the actual efficiency from experimental measurements and numerical predictions for eight woven-wire screens with mesh sizes ranging from 14×14 to 64×64 and fraction of open area from 0.436 to 0.719 in the wire Reynolds number range of 1 to 158. Figure 6.3 shows comparisons of the individual actual efficiencies versus Stokes number. It can be seen that there is a fairly good agreement between experimental and numerical results, even though the ideal model was

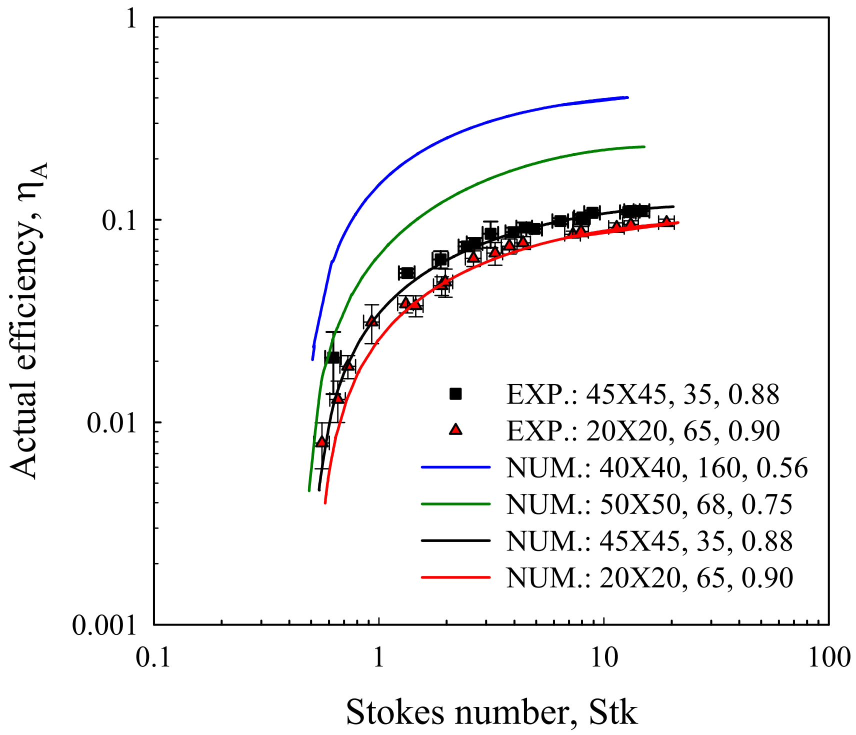

Figure 6.1. Comparison of actual efficiency predictions for electroformed-wires to experimental and numerical data (Re_C = 0.5 to 30). Parameters in legend are mesh size, wire diameter (μm) and fraction of open area (f_{OA}).

used in the numerical study instead of the real woven-wire model. The slight discrepancy noticed for some of the case may be explained by the non-ideal nature of the woven-wire screen, as in a real screen, the wires are not distributed uniformly and not all are perpendicular to the flow direction.

Figure 6.4 shows a comparison of the actual efficiencies for the experimental and numerical cases for the welded screen with a mesh size of 8×8 and fraction of open area at 0.746 for wire Reynolds numbers from 10 to 100.

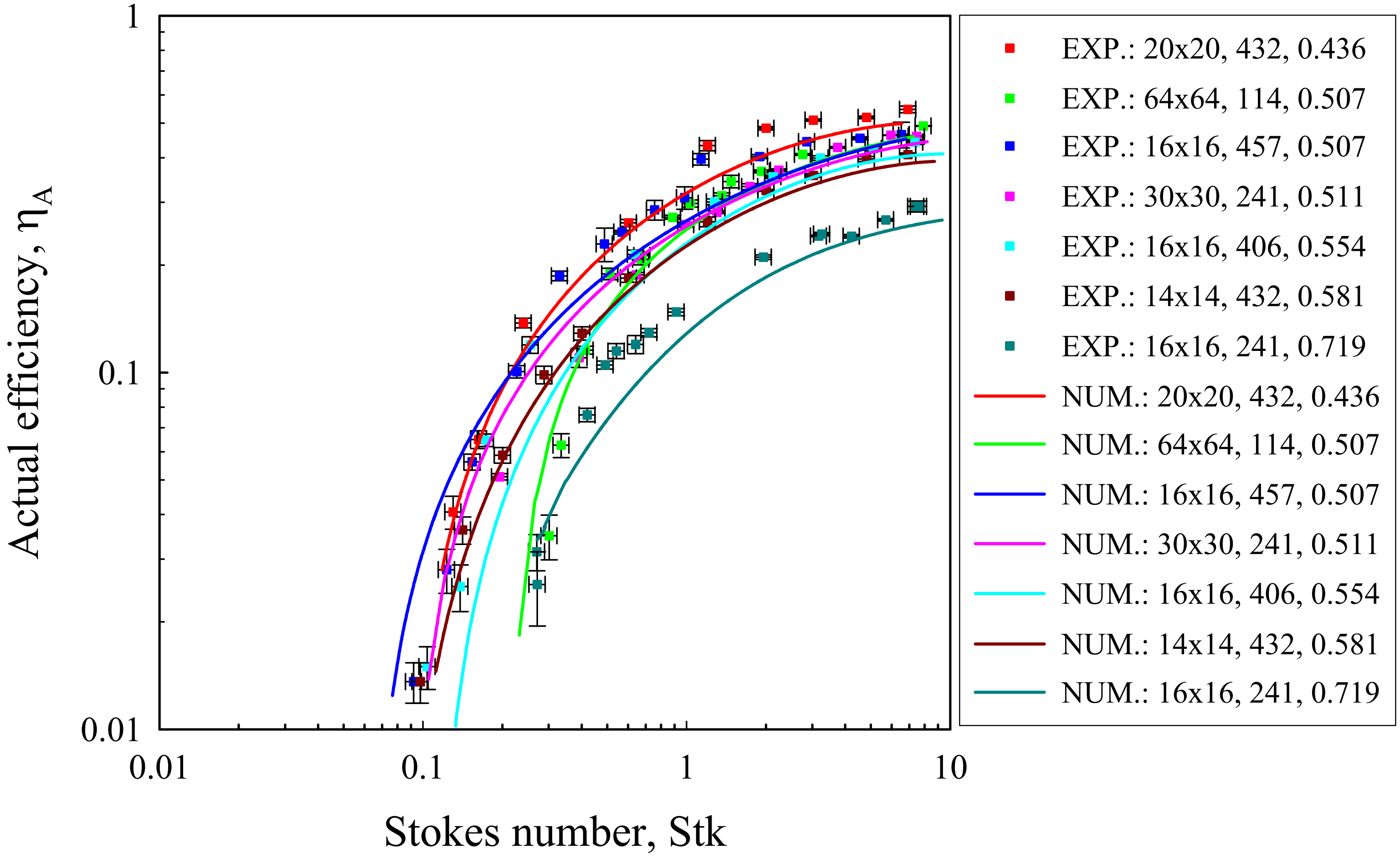

Figure 6.2. Comparison of actual efficiency predictions for woven-wires to experimental and numerical data (Re_C = 1 to 158). Parameters in label are mesh size, wire diameter (μm) and fraction of open area.

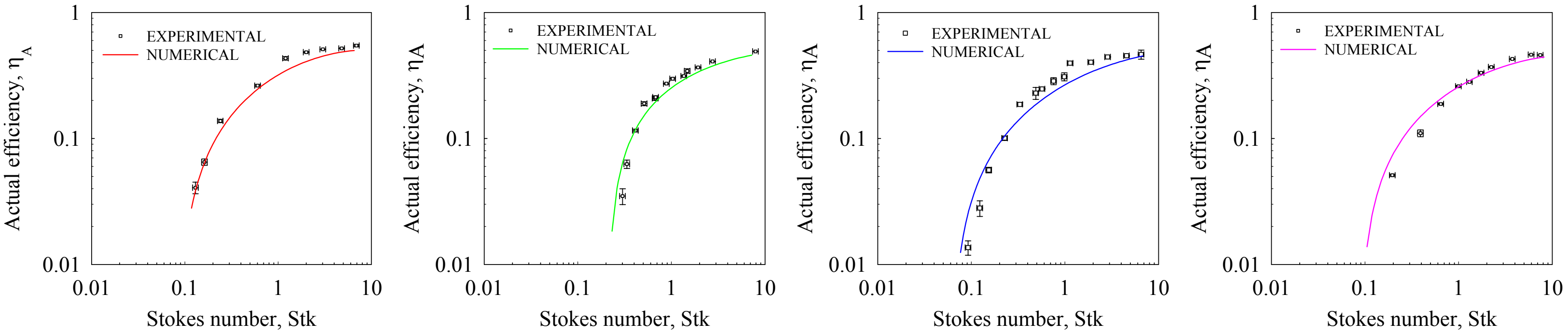

(a) 20×20, 0.017, 0.436 (b) 64×64, 0.0045, 0.507 (c) 16×16, 0.018, 0.507 (d) 30×30, 0.0095, 0.511

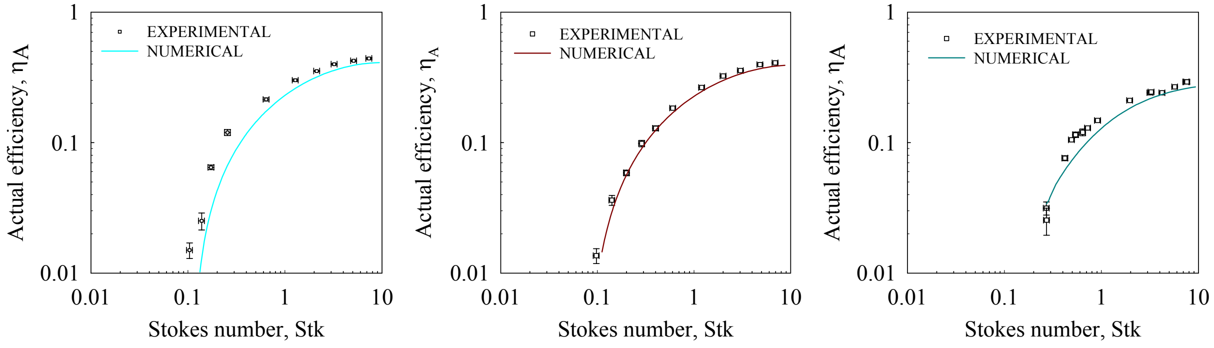

(e) 16×16, 0.016, 0.554 (f) 14×14, 0.017, 0.581 (g) 16×16, 0.0095, 0.719

Figure 6.3. Comparison of actual efficiency predictions for woven-wires to experimental data (Re_C = 1 to 158). Parameters in label are mesh size, wire diameter (μm) and fraction of open area.

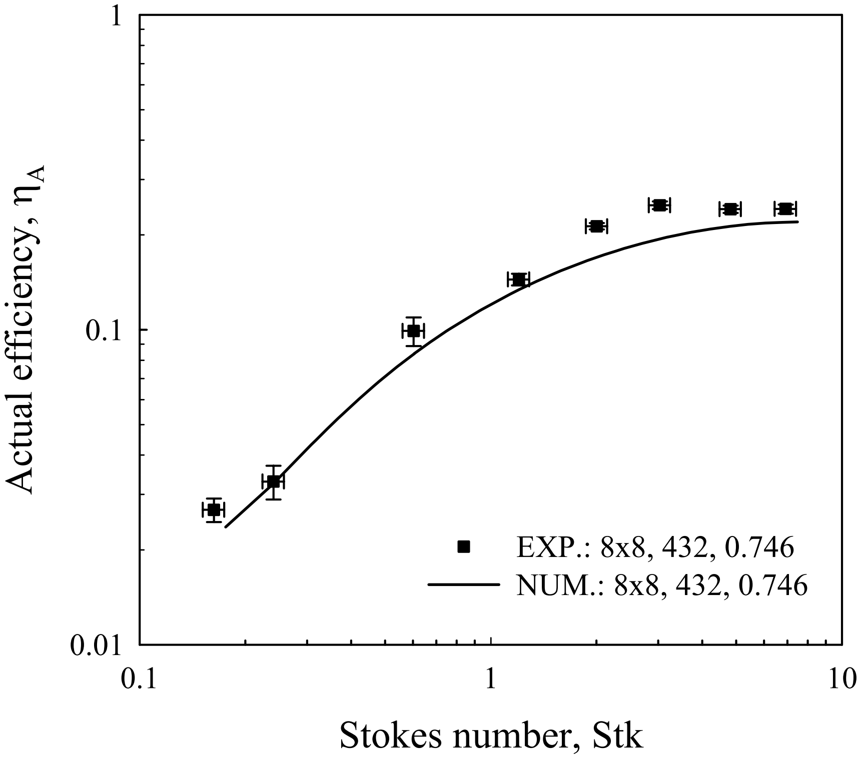

Figure 6.4. Comparison of actual efficiency predictions for welded-wires to experimental and numerical data (Re_C = 10 to 100). Parameters in label are mesh size, wire diameter (μm) and fraction of open area.

Figure 6.5 shows a comparison of actual efficiency from experimental and numerical studies for perforated-sheets with two different fractions of open area (0.21 and 0.51) in the effective slack Reynolds number ranging from 10 to 575.

Numerical predictions are seen to be in very good agreement to the experimental data. There are certain very interesting features to be observed from the presented results. First, it can be seen that the log-log plot of η_A against *Stk* leads to a curve whose slope depend on the areal solidity (α_A). An increase in the collection efficiency through a reduction of the opening size to a neighboring wire may be explained by the compression

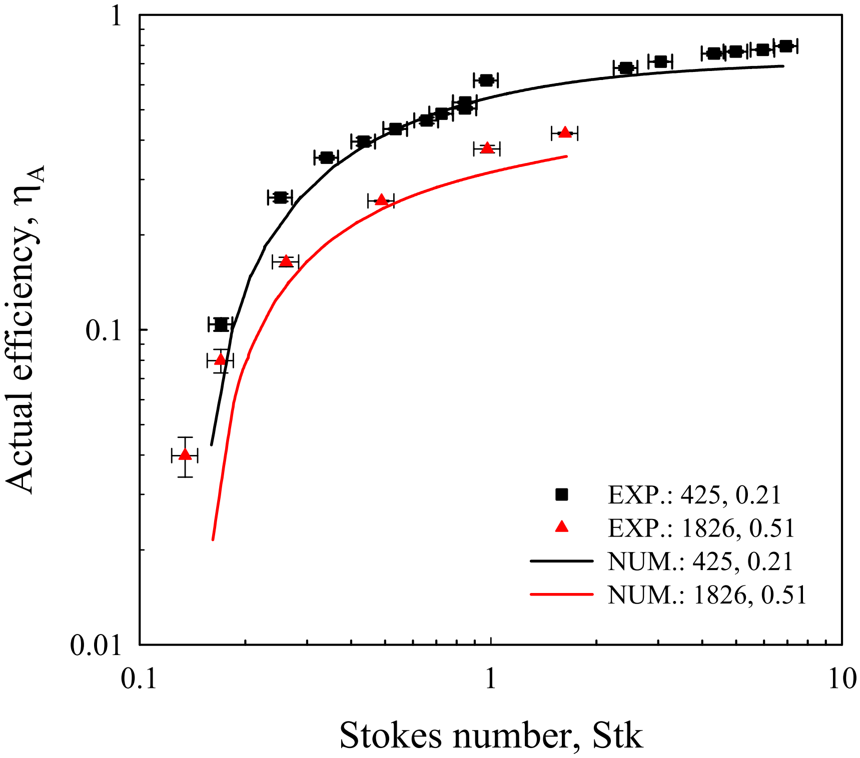

Figure 6.5. Comparison of actual efficiency predictions for perforated-sheet to experimental and numerical data (Re_C=10 to 575). Parameters in label are effective slack length (μm) and fraction of open area.

of the fluid streamlines in the vicinity of the wires as a result of continuity. Second, results show that beginning at critical Stokes number (Stk_c), efficiency increased gradually to its maximum value that was almost asymptotic to its solidity for that particular screen, at higher Stokes numbers.

Actual Efficiency Modeling

Literature presents relatively few studies that have developed mathematical models for screens to describe collection efficiency. Most of the earlier studies were performed with fibrous filter under conditions where diffusion, interception and inertial impaction effects were considered. The present study examined flow at low and intermediate characteristic length Reynolds number conditions to obtain a better understanding of the factors that influence variation in screen efficiency.

In all the cases, the log-log plot of actual efficiency (η_A) against Stokes number leads to a curve whose slope and y-intercept both depend on the solidity (α_A) as shown in Figures 6.1 through 6.5. The relationship between the actual efficiency and Stokes number can be obtained in initial form (Hyperbolic, 3 parameters) using a commercial graphing software (SigmaPlot 2004).

$$\eta_A = C_1 + \frac{C_2}{1 + \frac{Stk}{C_3}} \tag{6-1}$$

Where C_1, C_2, and C_3 are functions of the solidity (α_A). The values of C_1, C_2, and C_3 are obtained by a regression analysis of the combined experimental and numerical data and are listed in Table 6.1 for each screen. Further regression analyses for C_1, C_2, and C_3 were performed as a function of the solidity (α_A). These are shown in Figures 6.6 and 6.8 respectively. The functions C_1, C_2, and C_3 turned out to be a function of the solidity, at least in the range of α_A tested in this study ($0.10 \le \alpha_A \le 0.79$). Therefore, Equation (6-1) is modified to the following.

$$\eta_A = (z_0 + z_1\alpha_A) + \frac{(z_2 + z_3\alpha_A)}{1 + \frac{Stk}{(z_4 + z_5\alpha_A)}} \tag{6-2}$$

With further regression, the constants, z_0, z_1, z_2, z_3, z_4, and z_5 for all screens were calculated and are listed in Table 6.2 due to express a final correlation between the actual efficiency and the solidity and Stokes number. Therefore, the final correlation for each screen can be expressed as

Table 6.1 Values of C_1, C_2, and C_3 in Equation (6-1) obtained by regression analysis.

Screen Type	**Wire diameter Hole diameter (dw or d_h)** inch	μm	**Fraction of Open Area (f_{OA})**	**Mesh Size**	**Solidity (α_A)**	C_1 **Value**	**StdErr**	C_2 **Value**	**StdErr**	C_3 **Value**	**StdErr**	R^2
Electroformed	0.00629	160	0.56	40	0.44	0.4370	0.0008	-0.7260	0.0052	0.6677	0.0107	0.9997
Electroformed	0.00268	68	0.75	50	0.25	0.2578	0.0005	-0.3561	0.0012	1.1680	0.0134	0.9998
Electroformed	0.00138	35	0.88	45	0.12	0.1213	0.0010	-0.1880	0.0028	0.8679	0.0431	0.9969
Electroformed	0.00257	65	0.90	20	0.10	0.1038	0.0006	-0.1450	0.0024	1.1660	0.0552	0.9962
Woven	0.0170	432	0.44	20	0.56	0.5601	0.0069	-0.6322	0.0075	0.5857	0.0360	0.9908
Woven	0.0045	114	0.51	64	0.49	0.4958	0.0065	-0.6700	0.0160	0.5474	0.0432	0.9892
Woven	0.0180	457	0.51	16	0.49	0.4819	0.0078	-0.5201	0.0073	0.6222	0.0454	0.9826
Woven	0.0095	241	0.51	30	0.49	0.4893	0.0048	-0.5263	0.0048	0.7654	0.0329	0.9944
Woven	0.0160	406	0.55	16	0.45	0.4623	0.0049	-0.5226	0.0051	0.7719	0.0396	0.9928
Woven	0.0170	432	0.58	14	0.42	0.4340	0.0023	-0.4785	0.0043	0.7458	0.0140	0.9980
Woven	0.0095	241	0.72	16	0.28	0.3083	0.0103	-0.3422	0.0083	1.0520	0.1180	0.9828
Welded	0.0170	432	0.75	8	0.25	0.2685	0.0073	-0.2955	0.0076	0.9604	0.1256	0.9733
Perforated	0.0150	381	0.21	N/A	0.79	0.7445	0.0081	-1.3220	0.0886	0.1669	2.10E-02	0.9830
Perforated	0.1875	4763	0.51	N/A	0.49	0.4425	0.0147	-0.7329	0.0610	0.1859	4.05E-02	0.9755

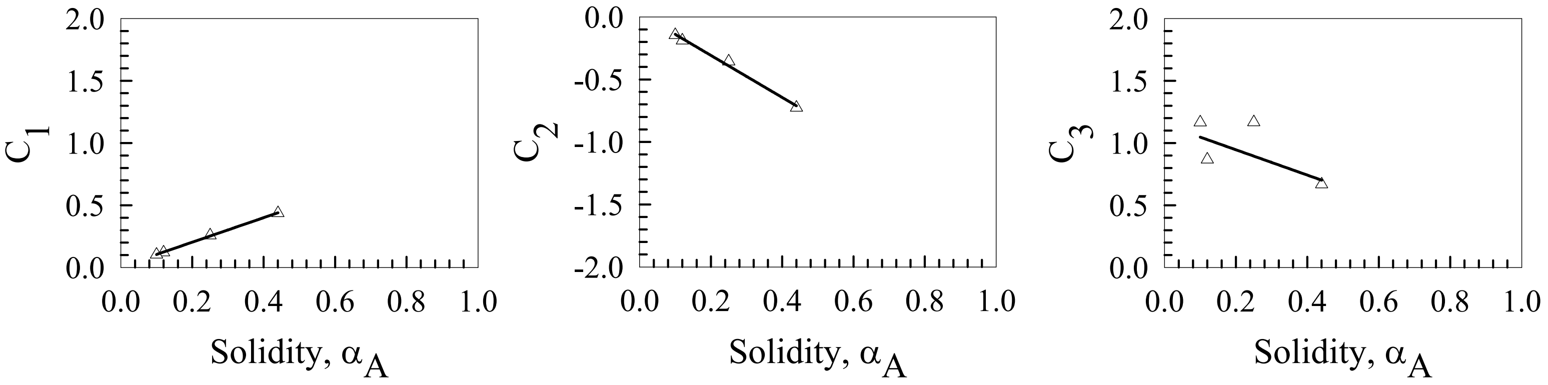

(a) C_1 vs. α_A (b) C_2 vs. α_A (c) C_3 vs. α_A

Figure 6.6. The functions C_1, C_2, and C_3 of Equation (6-1) for electroformed-wire screens.

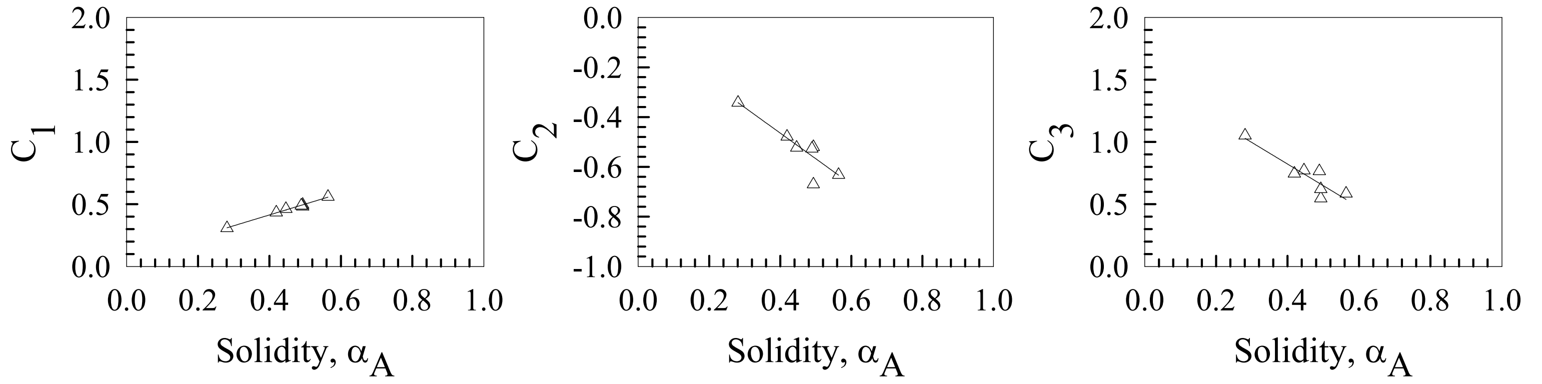

(a) C_1 vs. α_A (b) C_2 vs. α_A (c) C_3 vs. α_A

Figure 6.7. The functions C_1, C_2, and C_3 of Equation (6-1) for woven-wire and welded-wire screens.

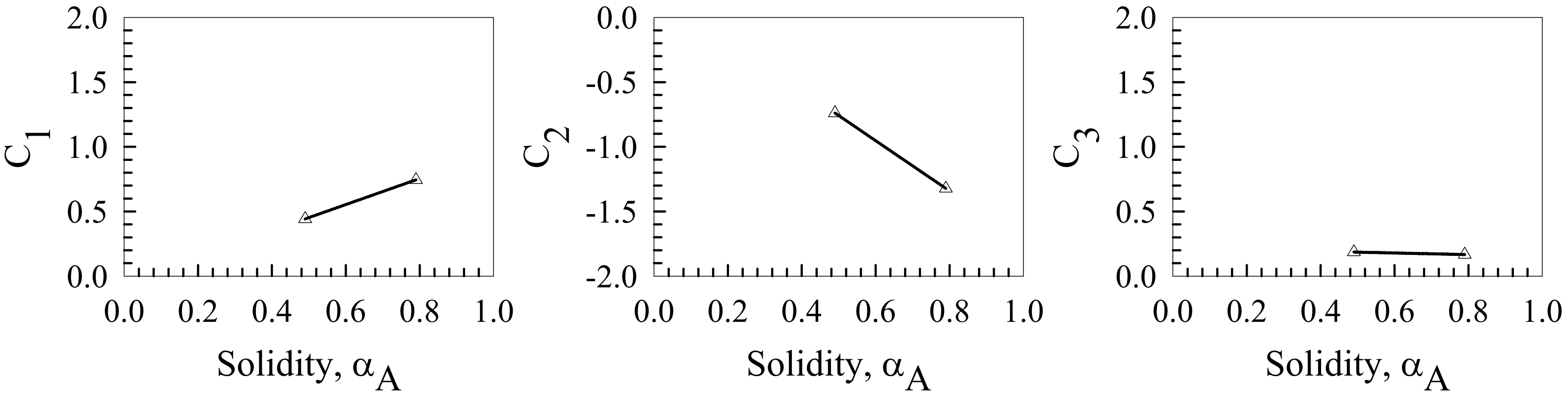

(a) C_1 vs. α_A (b) C_2 vs. α_A (c) C_3 vs. α_A

Figure 6.8. The functions C_1, C_2, and C_3 of Equation (6-1) for perforated-sheet screens.

Table 6.2 Values of z_0, z_1, z_2, z_3, z_4, and z_5 in Equation (6-2) obtained by regression analysis.

Screen	$C_1=z_o+z_1\alpha_A$					$C_2=z_2+z_3\alpha_A$					$C_3=z_4+z_5\alpha_A$				
Type	z_0		z_1		R^2	z_2		z_3		R^2	z_4		z_5		R^2
	Value	**StdErr**	**Value**	**StdErr**		**Value**	**StdErr**	**Value**	**StdErr**		**Value**	**StdErr**	**Value**	**StdErr**	
Electroformed	0.006	0.005	0.985	0.018	0.999	0.029	0.029	-1.682	0.109	0.998	1.149	0.210	-1.018	0.661	0.542
Woven	0.066	0.016	0.870	0.034	0.993	-0.053	0.071	-1.029	0.165	0.886	1.516	0.163	-1.735	0.352	0.829
Perforated	-0.051	0.000	1.007	0.000	1.000	0.213	0.000	-1.943	0.000	1.000	0.217	0.000	-0.063	0.000	1.000

electroformed-wires:

$$\eta_A = (0.005838 + 0.9852\alpha_A) + \frac{(0.02889 - 1.682\alpha_A)}{1 + \frac{Stk}{(1.149 - 1.018\alpha_A)}}$$

$0.10 \le \alpha_A \le 0.44$, $0.49 \le Stk \le 20$ (6-3)

woven-wires:

$$\eta_A = (0.06565 + 0.8704\alpha_A) + \frac{(-0.05282 - 1.029\alpha_A)}{1 + \frac{Stk}{(1.516 - 1.735\alpha_A)}}$$

$0.28 \le \alpha_A \le 0.56$, $0.11 \le Stk \le 9.39$ (6-4)

welded-wire:

$$\eta_A = 0.2685 + \frac{(-0.2955)}{1 + \frac{Stk}{0.9604}}$$

$\alpha_A = 0.25$, $0.16 \le Stk \le 7.47$ (6-5)

perforated-sheets:

$$\eta_A = (-0.05077 + 1.007\alpha_A) + \frac{(0.2132 - 1.943\alpha_A)}{1 + \frac{Stk}{(0.2169 - 0.0633\alpha_A)}}$$

$0.49 \le \alpha_A \le 0.79$, $0.13 \le Stk \le 6.93$ (6-6)

Figures 6.9 to 6.12 present correlation plots between the measured and calculated efficiencies that provide a confidence estimate on these correlations. Actual efficiency values obtained from experimental and numerical results are plotted as function of the correlated actual efficiency based on these correlations with error bar which are calculated with the uncertainty ($w\eta_A$, measured).

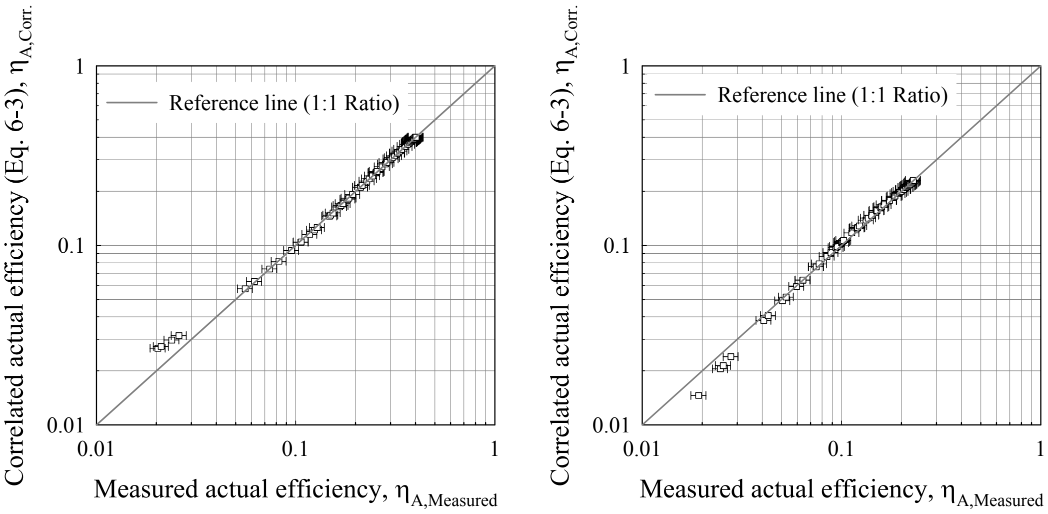

SSE = 0.003 < 0.086 = $w\eta_{A,Measured}$
(a) 40×40, 160, 0.56

SSE = 0.006 < 0.086 = $w\eta_{A,Measured}$
(b) 50×50, 68, 0.75

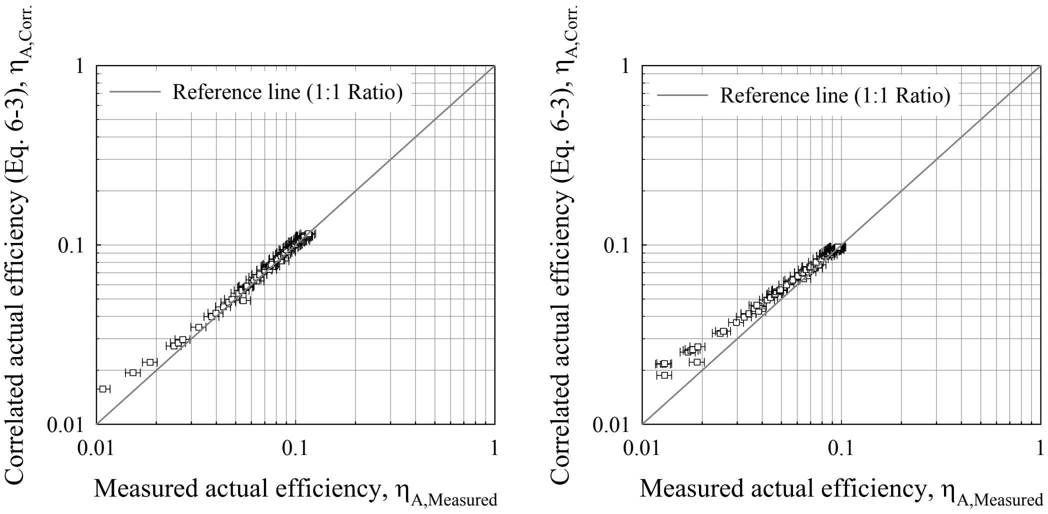

SSE = 0.0004 < 0.086 = $w\eta_{A,Measured}$

(c) 45×45, 35, 0.88

SSE = 0.002 < 0.086 = $w\eta_{A,Measured}$

(d) 20×20, 65, 0.90

Figure 6.9. Comparison between the experimentally and numerically measured actual efficiency and correlated actual efficiency based on correlation (Equation 6-3) for electroformed-wire screens.

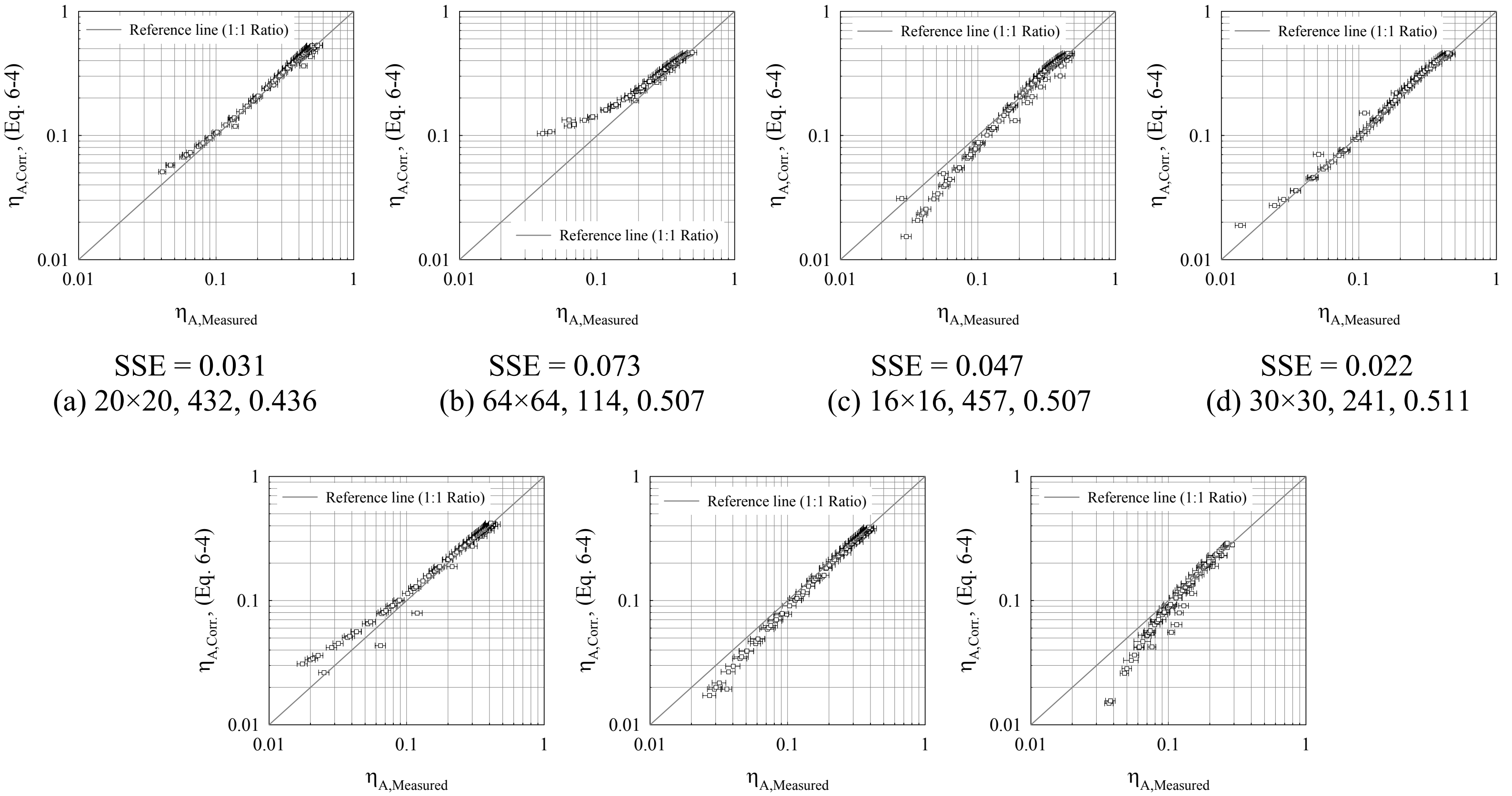

SSE = 0.031
(a) 20×20, 432, 0.436

SSE = 0.073
(b) 64×64, 114, 0.507

SSE = 0.047
(c) 16×16, 457, 0.507

SSE = 0.022
(d) 30×30, 241, 0.511

SSE = 0.021
(e) 16×16, 406, 0.554

SSE = 0.011
(f) 14×14, 432, 0.581

SSE = 0.024
(g) 16×16, 241, 0.719

Figure 6.10. Comparison between the experimentally and numerically measured actual efficiency and correlated actual efficiency based on correlation (Equation 6-4) for woven-wire screens.

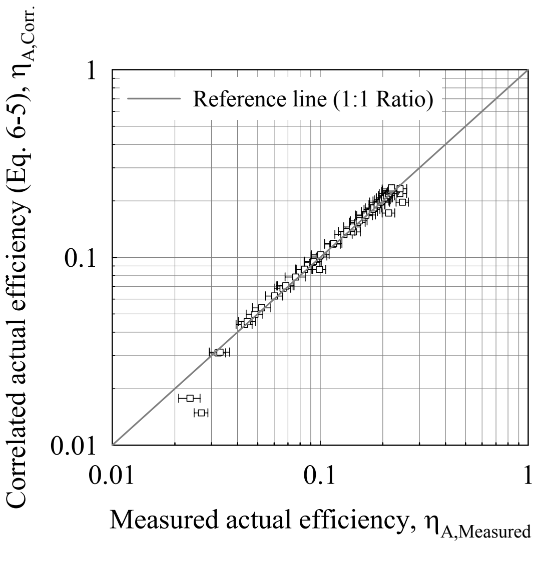

SSE = 0.006

Figure 6.11. Comparison between the experimentally and numerically measured actual efficiency and correlated actual efficiency based on correlation (Equation 6-5) for welded-wire screen.

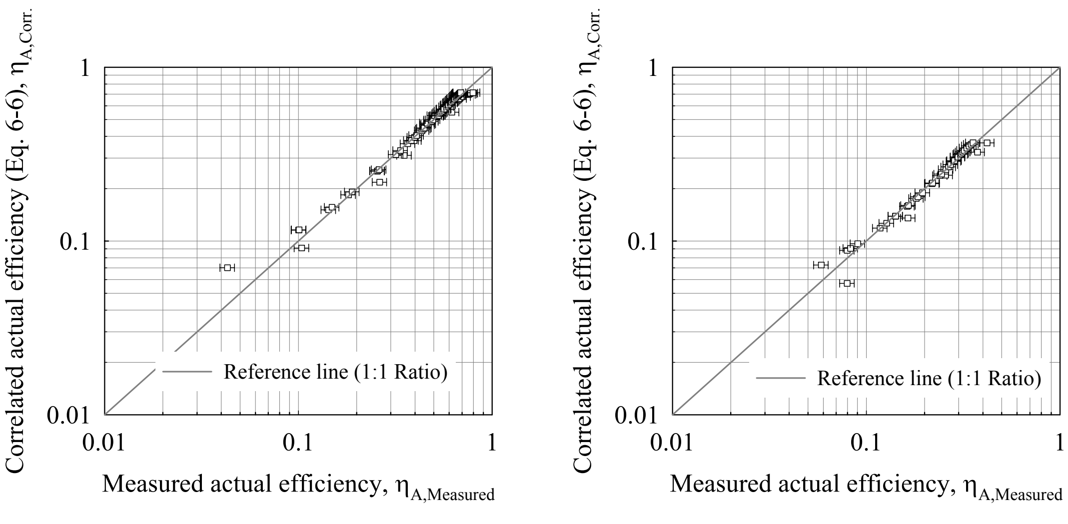

SSE = 0.039

SSE = 0.010

(a) 425, 0.21

(b) 1826, 0.51

Figure 6.12. Comparison between the experimentally and numerically measured actual efficiency and correlated actual efficiency based on correlation (Equation 6-6) for perforated-sheet screens.

The solid line is a reference line which has a ratio of one between the two efficiencies. There are certain very interesting features to be observed from the presented results. First, it can be seen visually whether the calculated actual efficiency under-predicts or over-predicts based on the reference line. Second, a residue is the difference between the measured and correlated value of a function. Some residues are positive and others negative. If we add up the squares of the residues, we get a measure of how well the line fits, called the Sum-of-Squares error (SSE). The SSE of the measured data is approximated by a function that is given by

$$\begin{aligned} \text{SSE} &= \text{Sum of squares of residues} \\ &= \text{Sum of } (y_{\text{measured}} - y_{\text{correlated}})^2 \end{aligned} \tag{6-7}$$

The smaller SSE, the better the approximating function fits the data. Additionally, in all the cases (Figures 6.9 to 6.12) the SSE should be less than the uncertainty of measured value. If the SSE is larger than the experimental uncertainty value, the correlation equation is not valid for predicting values. There is another statistical approach to report this result whether mathematical models (Equations 6-3 to 6-6) are best-fit for measured results. The p value from a paired t-test in statistic was less than 0.01 for these models (Equations 6-3 to 6-6) in the case of 99% confidence intervals. Figures 6.13 to 6.16 were re-plotted to compare with the experimentally and numerically measured efficiency and the calculated efficiency, in addition to gray curves that were based on correlation Equations (6-3 to 6-6). They can be seen that the gray curves indicate exactly similar collection trends compared to measured data, are spaced proportionally apart from their neighbors, and asymptotically approach a maximum efficiency value that is equal to their areal solidity.

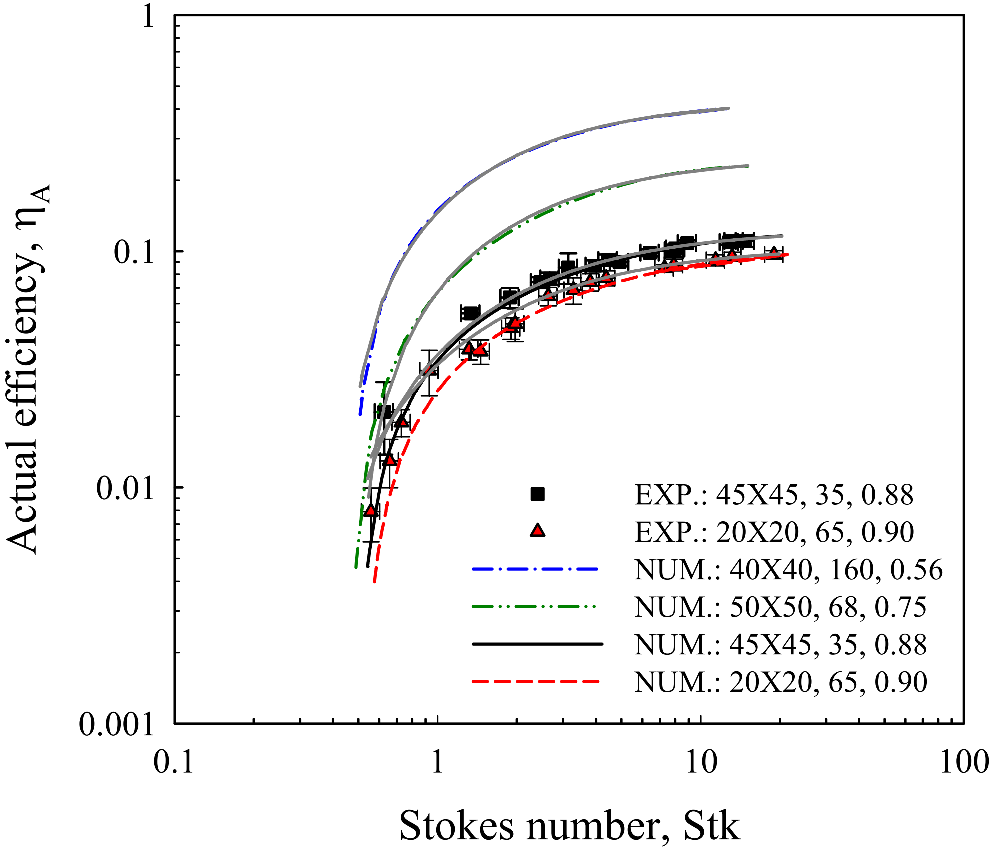

Figure 6.13. Comparison of actual efficiency predictions for electroformed-wires (Re_C = 0.5 to 30). Parameters in legend are mesh size, wire diameter (μm), and fraction of open area (f_{OA}).

Note: The gray curves were plotted by correlation

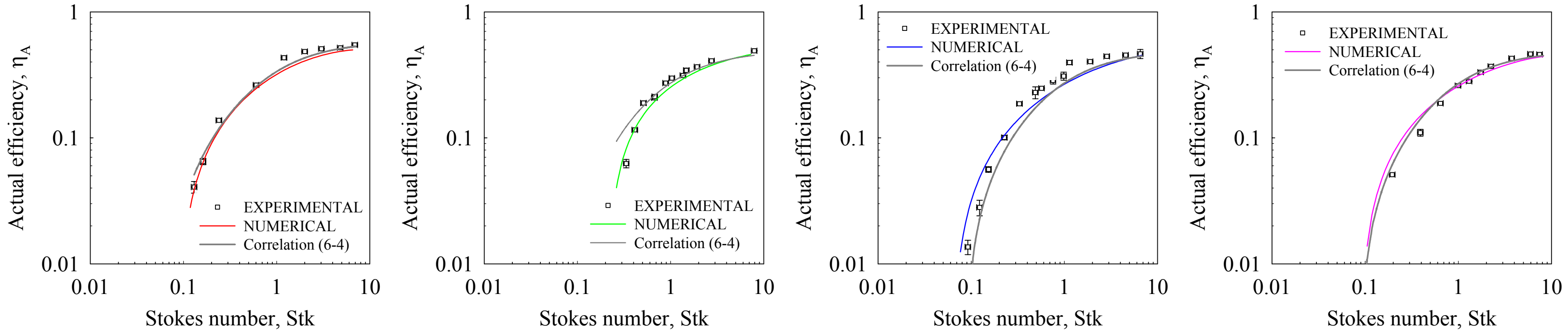

(a) 20×20, 432, 0.436 (b) 64×64, 114, 0.507 (c) 16×16, 457, 0.507 (d) 30×30, 241, 0.511

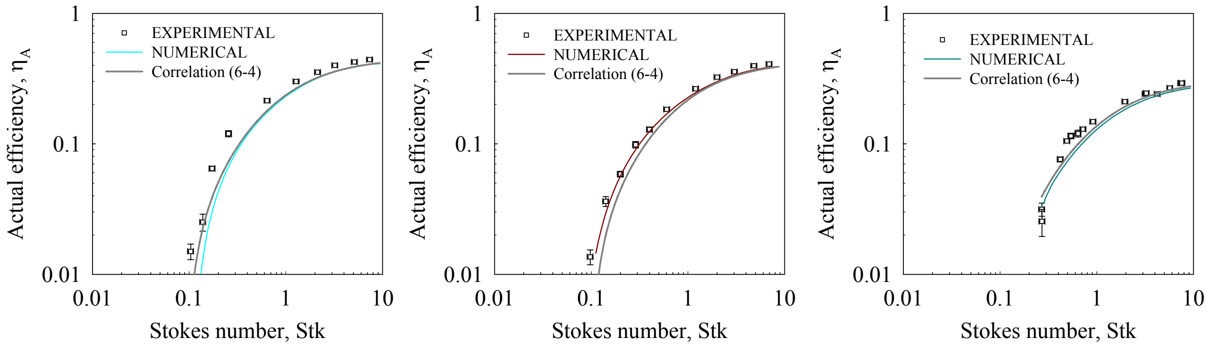

(e) 16×16, 406, 0.554 (f) 14×14, 432, 0.581 (g) 16×16, 241, 0.719

Figure 6.14. Comparison of actual efficiency predictions for woven-wires (Re_C = 1 to 158). Parameters in legend are mesh size, wire diameter (μm), and fraction of open area (f_{OA}).
Note: The gray curves were plotted by correlation Equation (6-4).

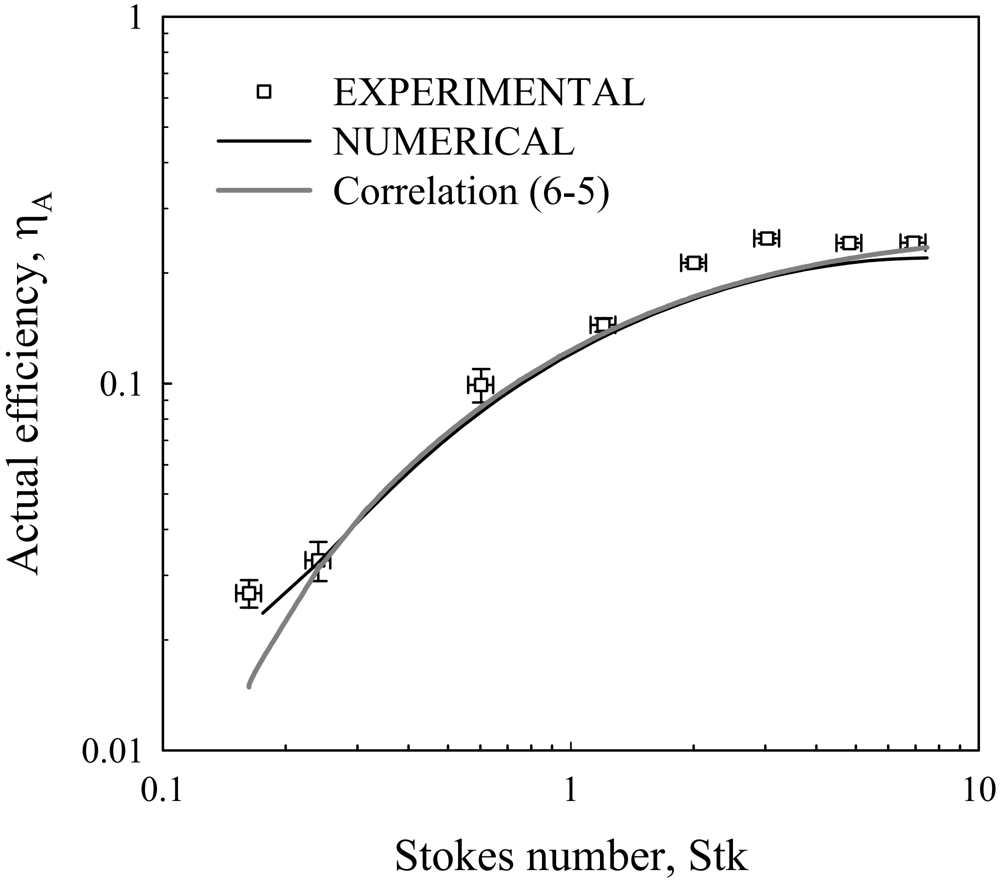

Figure 6.15. Comparison of actual efficiency predictions for welded-wires (Re_C = 10 to 100).
Note: The gray curves were plotted by correlation Equation (6-5).

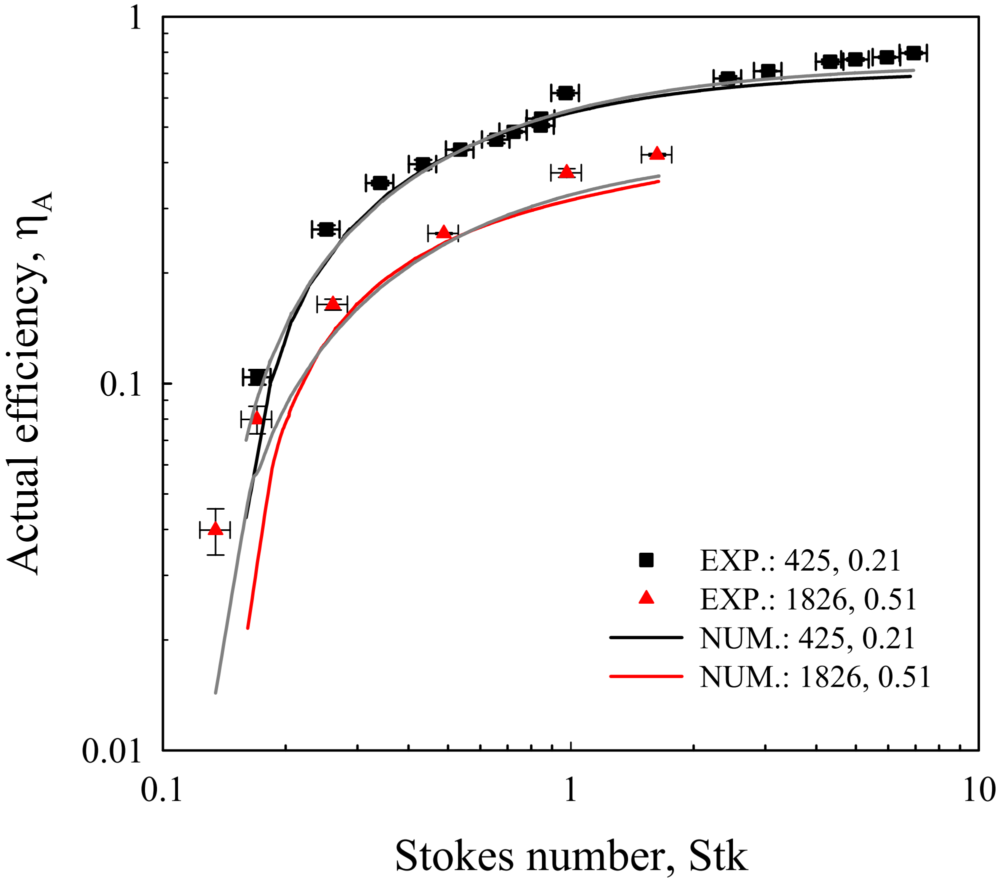

Figure 6.16. Comparison of actual efficiency predictions for perforated-sheet ($Re_C = 10$ to 575). Parameters in legend are effective slack length (μm) and fraction of open area (f_{OA}).
Note: The gray curves were plotted by correlation Equation (6-6).

Modeling for Standardized Screen Efficiency

Efforts were taken to see if a common basis can be evolved to standardize the experimental data obtained on the different screen types (as well as the numerical predictions obtained on the different screen types) that was spread over a wide range of Stokes numbers depending on their characteristic nature (solidity). As seen in previous Figures 6.1 to 6.4, the y-intercept and slope increase with the solidity (α_A) or, equivalently, the actual efficiency increase with solidity for a given value of Stokes number. It was seen that a new parameter "standardized efficiency" (η_{SS}) that non-dimensionalizes the actual collection based on the corresponding screen solidity, would nearly collapse the aerosol deposition data on screens with four different solidity values to a single performance curve. The standardized screen efficiency, η_{SS}, is defined as follows:

$$\eta_{SS} = \frac{\eta_A}{1 - f_{OA}} = \frac{\eta_A}{\alpha_A} \qquad (6\text{-}8)$$

Aerosol deposition on different screen materials collapsed to a single performance curve as shown with experimental and numerical data points in Figure 6.17. Especially, in the case of woven-wire screen the data looks scattered at less than Stokes number 1.0.

With these results, the correlation between the standardized screen efficiency and Stokes number can be expressed as this form (Sigmoidal, Logistic, 4-parameter)

$$\eta_{SS,Corr.} = \frac{\eta_A}{\alpha_A} = f(Stk) = x_0 + \frac{x_1}{1 + (\frac{Stk}{x_2})^{x_3}} \quad \text{(subscript } \textit{corr.} \text{ for correlation)} \qquad (6\text{-}9)$$

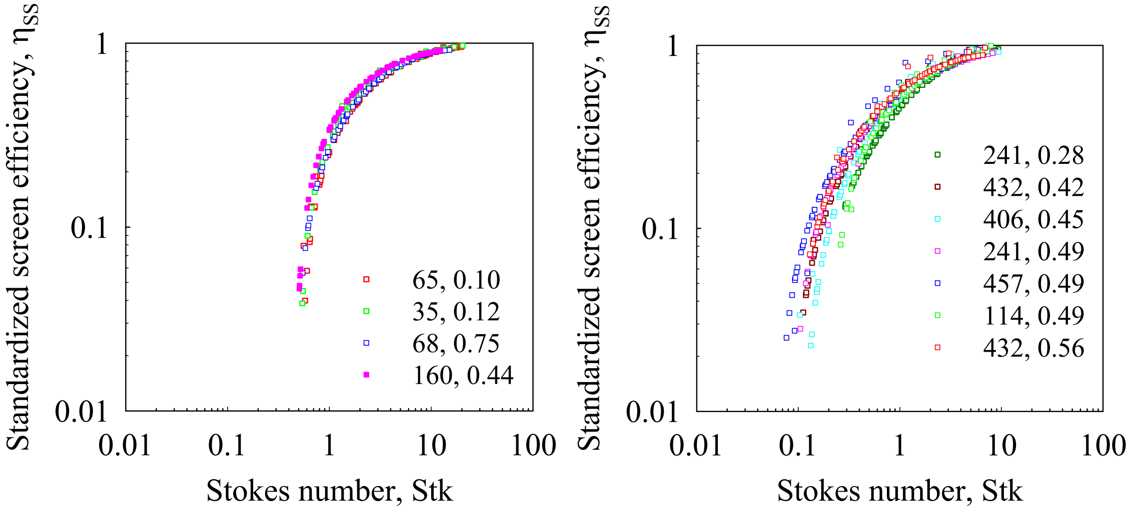

(a) Electroformed-wire

(b) Woven-wire

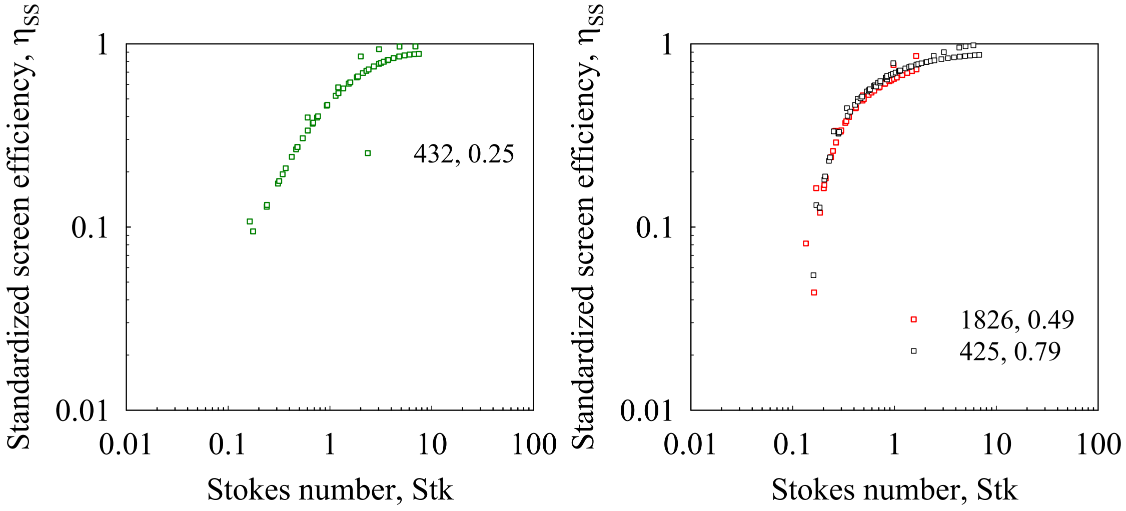

(c) Welded-wire

(d) Perforated-sheet

Figure 6.17. Comparison of standardized screen efficiency predictions for four screens (a. electroformed-wire, b. woven-wire, c. welded-wire, and d. perforated-sheet) to experimental and numerical data.
Note: The solid curves were plotted by correlation.

To verify the confidence for standardizing all data points using linear regression method was compared with both measured standardized screen efficiency and correlated standardized screen efficiency (Figure 6.18) so that R^2 value was provided.

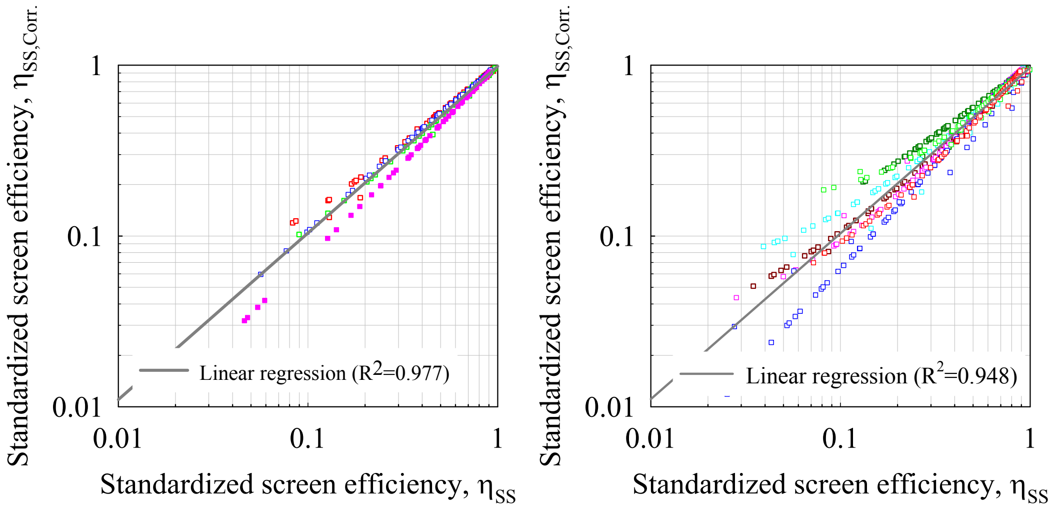

(a) Electroformed-wire (b) Woven-wire

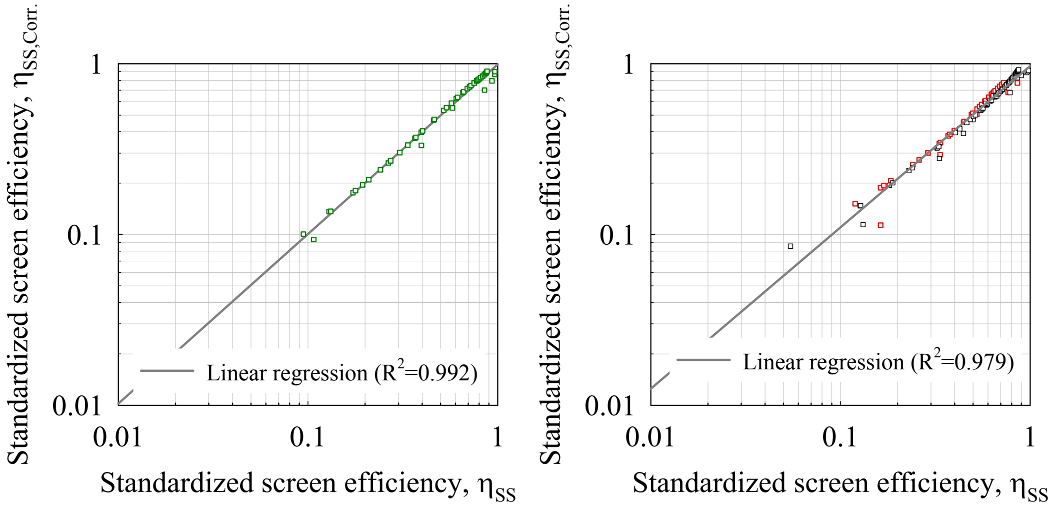

(c) Welded-wire (d) Perforated-sheet

Figure 6.18. Plot for verifying the standardizing data points with linear regression method.

The constants, x_0, x_1, x_2, and x_3 for all screens were provided in Table 6.3 to express a final correlation between the standardized screen efficiency and Stokes number.

Table 6.3 Values of x_0, x_1, x_2, and x_3 in Equation (6-9) obtained by regression analysis.

Screen	$x_0+x_1/(1+(Stk/x_2)^{x3}$									Remark
Type	x_0		x_1		x_2		x_3		R^2	
	Value	**StdErr**	**Value**	**StdErr**	**Value**	**StdErr**	**Value**	**StdErr**		
Electroformed	-0.714	0.124	1.777	0.136	0.742	0.108	-0.852	0.062	0.992	(0.50≤Stk≤20)
Woven	-0.089	0.022	1.156	0.037	0.878	0.023	-0.963	0.040	0.981	(0.08≤*Stk*≤12)
Perforated	-0.900	0.384	1.858	0.413	0.141	0.058	-0.908	0.132	0.985	(0.15≤*Stk*≤7)

As a practical matter, Equation (6-9) can be re-expressed with Stk_{50} (Table 6.4), the Stokes number that corresponds to 50% collection efficiency value, as follows:

$$\eta_{SS,corr.} = x_o + \frac{x_1}{1+x_4(\frac{Stk}{Stk_{50}})^{x_3}} \tag{6-10}$$

Table 6.4 Values of Stk_{50}, and x_4 in Equation (6-10).

Screen Type	Stk_{50}	x_4
Electroformed	1.829	0.464
Woven	0.913	0.963
Perforated	0.483	0.327

In principle, it is not obvious whether standardized screen efficiency correlates with only solidity for the screens with different geometrical values even if the same fraction of open area (f_{OA}) is given. Here, as shown the Figure 6.19 that presented the comparison of actual efficiency with the same solidity, about 49% among the results of woven-wire screens in this Chapter. From this plot one can easily see that the set of data are distributed in three different trends (slope and y-intercept), one for 64×64 mesh size (wire diameter 114 μm, fraction of open area 0.51), another for 16×16 mesh size (wire diameter 457 μm, fraction of open area 0.51) and the other for 30×30 mesh size (wire diameter 241 μm, fraction of open area 0.51). These groups of data appear to follow three different distributions, particularly for Stokes number less than 1.0. It is known that the collection process is a combination of several different mechanisms. In the process of analyzing the original results and its non-dimensional form, it became apparent that collection characteristics for three screens with the same areal solidity value but different wire dimensions would be different. This suggests that solidity may not be the only parameter that influences collection. While Stokes number accounts for the collection due

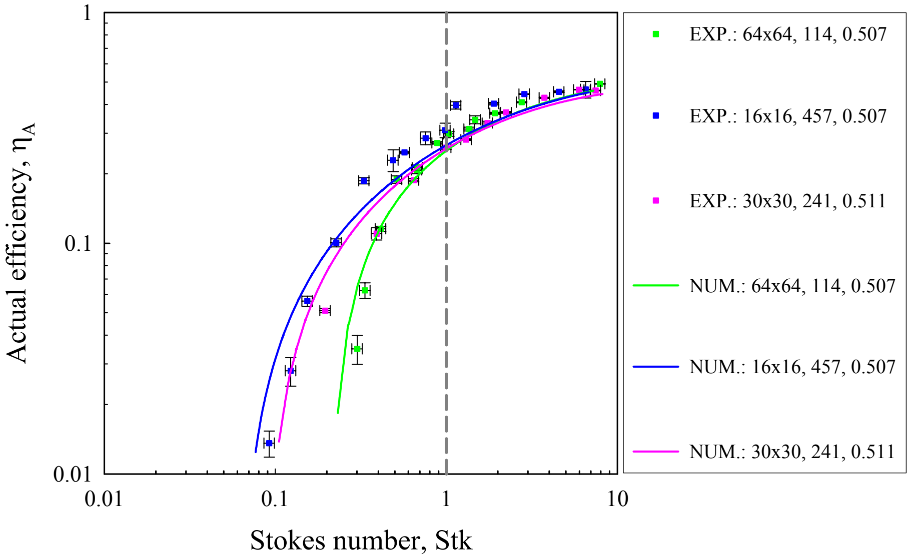

Figure 6.19. Comparison of actual efficiency predictions for woven-wires to experimental and numerical data with the same fraction of open area (0.51). Parameters in label are mesh size, wire diameter (μm) and fraction of open area.

to impaction which is the primary collection mechanism, other mechanisms such as interception as well as flow effects may contribute to the overall collection. With this examination, the definition of η_{SS} can be re-expressed as

$$\eta_{SS} = \frac{\eta_A}{\alpha_A} \times H \tag{6-11}$$

The above discussion indicated that a closer introspection of the developed correlation needed to be undertaken. Subsequently, a correction factor to account for the two effects was evolved in terms of the respective non-dimensional parameters (*R, Re$_C$*), that would act as a multiplier to the standardized efficiency presented in Equation (6-11), as below:

$$H = f(R, Re_C) : \text{correction factor for standardizing} \tag{6-12}$$

where *R* is the interception parameter; Re_C is the Reynolds number.

With multiple trial-and-error attempts, we could make standardizing the actual efficiency data for each screen collapsed. It was seen that when the actual efficiency (η_A) is converted to standardizing basis by defining a standardized screen efficiency, η_{SS}

$$\eta_{SS} = \frac{\eta_A}{\alpha_A} \times H = \frac{\eta_A}{\alpha_A} \times (1+R)^{\beta 1} \times (1 + \frac{\beta 2}{Re_C{}^{\beta 3}}) \tag{6-13}$$

where $\beta 1$, $\beta 2$, and $\beta 3$ are unknown constant values for a single performance curve.

It was seen that the final form of the standardized screen efficiency, η_{SS}, as presented in Equation (6-13) was successfully able to narrow the scatter observed in the original non-dimensional form presented in Equation (6-10), indicating that these parameters have a minor effect on collection. Equation (6-13) should be asymptotically relevant when we obtain the actual efficiency from standardized screen efficiency and correction factors. The constants, *β1*, *β2*, and *β3* for all screens were provided in Table 6.5 to express an interim correlation.

Table 6.5 Values of *β1*, *β2*, and *β3* in Equation (6-13) obtained by trial-and-error and the evaluation of linear regression.

Screen	$(1+R^{\beta 2})$	$(1+\beta 3/Re_C{}^{\beta 4})$	
Type	$(R=d_p/d_C)$	$(Re_C=Ud_C/\nu)$	
	$\beta 2$	$\beta 3$	$\beta 4$
Electroformed	0.10	-0.03	0.01
Woven	0.10	-0.03	0.01
Perforated	0.10	-0.03	0.01

With all previous relationship, the standardized screen efficiency, $\eta_{SS,i}$, can be finally expressed as

$$\eta_{SS,i} = f(Stk) \times H = \left[x_o + \frac{x_1}{1 + x_4 (\frac{Stk}{Stk_{50}})^{x_3}} \right] \times \left[(1+R)^{\beta 1} \times (1 + \frac{\beta 2}{Re_C{}^{\beta 3}}) \right] \qquad (6\text{-}14)$$

The second product inside braces on the RHS of Equation (6-14) can be conceived as a correction factor that standardizes the absolute value of the collection efficiency with the physical and flow parameters associated with the collection process for the different screens. However, the areal solidity is a dominant factor for standardizing actual efficiency and the other factors as a minor factors help to collapse all actual efficiencies to a single performance curve. Aerosol deposition on different screen materials collapsed to a single performance curve as shown with experimental and numerical data points, and final regression curve in Figure 6.20.

To verify the confidence for standardizing all data points using linear regression method, an R^2 value was obtained by comparing the measured standardized screen

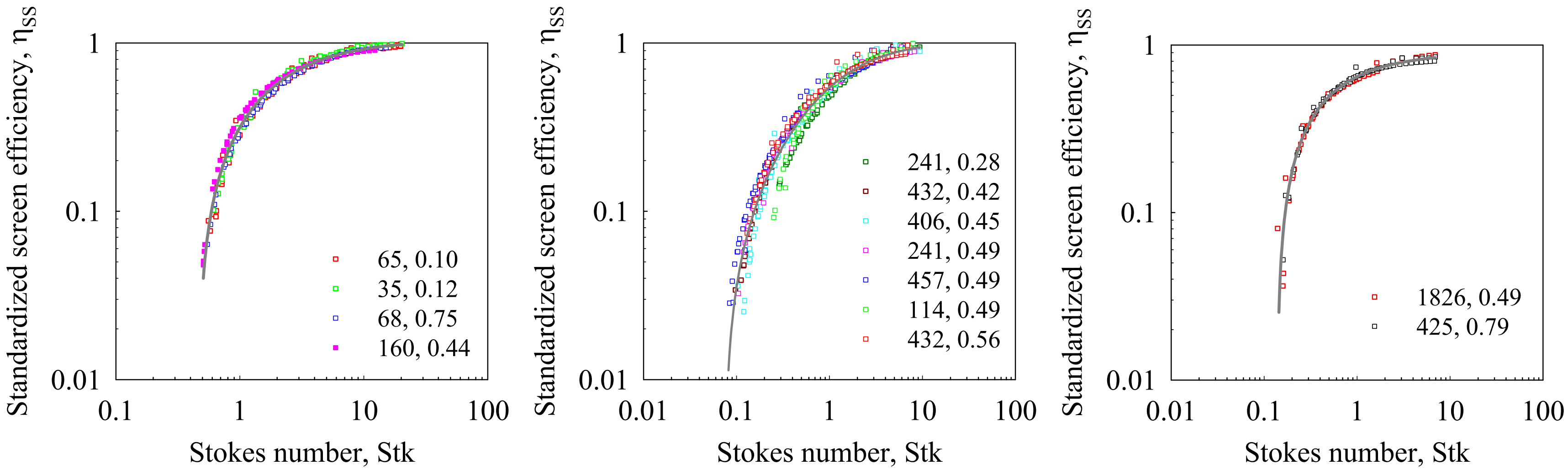

(a) Electroformed-wire (b) Woven-wire (c) Perforated-sheet

Figure 6.20. Comparison of standardized screen efficiency (Equation 6.13) predictions for screens (a. electroformed-wire, b. woven-wire, and c. perforated-sheet) to experimental and numerical data.
Note: The solid curves were plotted by Equation 6.14.

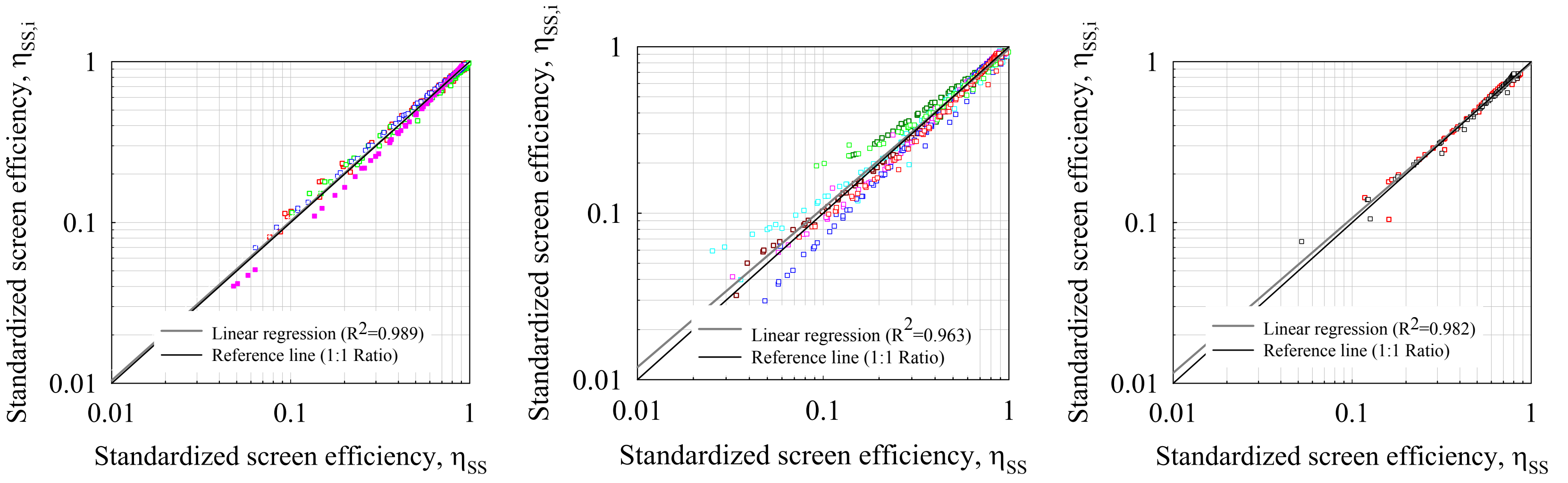

$(1\text{-}R^2) = 0.011 < 0.113 = w_{SS}$ $(1\text{-}R^2) = 0.037 < 0.113 = w_{SS}$ $(1\text{-}R^2) = 0.018 < 0.113 = w_{SS}$

(a) Electroformed-wire (b) Woven-wire (c) Perforated-sheet

Figure 6.21. Plot for verifying the standardizing data points with linear regression method. Comparison between the standardized screen efficiency (η_{SS}) of Equation 6.13 and correlated standardized screen efficiency ($\eta_{SS,i}$) of Equation 6.14, (a) electroformed-wire, (b) woven-wire, and (c) perforated-sheet.

efficiency (η_{SS}) of Equation (6-13) with correlated standardized screen efficiency ($\eta_{SS,i}$) of Equation (6-14) and is shown in Figure 6.21. We can see aerosol deposition on different screen materials collapsed to a single performance curve. There is small difference between Figure (6-17) and Figure (6-20), which the areal solidity is a dominant factor for standardizing actual efficiency. However, the other factors help to collapse all actual efficiencies to a single performance curve, especially the in the lower Stokes number regions (< 1.0). It is proved by the reference value for which R-square in Figure (6-21) is better than that in Figure (6-18). However, it was seen that the data could not be collapsed to a single performance curve even after multiple trial-and-error attempts and tuning for obtaining the best combination of correction factors. From Figures 6.20 (a and b) and 6.21(a and b) one can see that the whole set of data seems to be distributed into two different groups. Therefore, an additional plot is provided by analyzing the particular trends in Figure 6.22. It was seen that the two groups can be characterized in terms of a new parameter that can be called as the 'screen parameter' which is a product of the solidity and the circumference of a single wire. Among the parameters listed in Table 6.6, the wire diameter is probably the most critical of the factors, because the thickness of the knots where the wires with very small diameter cross over each other could be considered like the electroformed-wire screen. One (40×40 mesh screen) of groups on electroformed-wire screen appears to be highest screen parameter (0.009) and the other group (50×50, 20×20, and 45×45 mesh screens) appears to be almost the same value (0.001 to 0.002). In the case of woven-wire screen the screen parameter of one (64×64 and 16×16) of groups is 3 times higher than that of the other. As mentioned

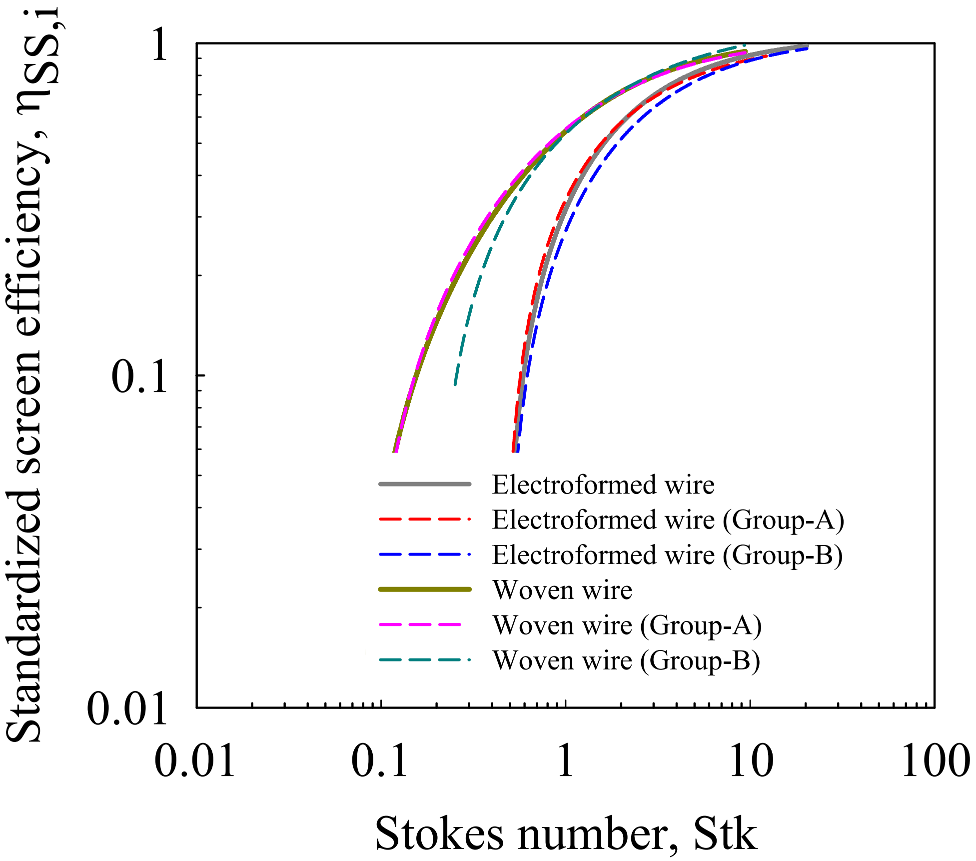

Figure 6.22. Plot for analyzing the characteristic of screen performance as a function of Stokes number. Curves are provided by Equation (6-14).

Table 6.6. The value of screen parameter for analyzing the characteristic of screen performance in Figure 6.24.

Type	d_w		f_{OA}	α_A	M	Screen Parameter ($\alpha_A \times \pi d_w$)
	inch	μm				
Electroformed wire	0.006290	160	0.56	0.44	40	**0.009**
	0.002680	68	0.75	0.25	50	0.002
	0.002565	65	0.90	0.10	20	0.001
	0.001380	35	0.88	0.12	45	0.001
Woven wire	0.0170	432	0.44	0.56	20	0.030
	0.0045	114	0.51	0.49	64	**0.007**
	0.0180	457	0.51	0.49	16	0.028
	0.0095	241	0.51	0.49	30	0.015
	0.0160	406	0.55	0.45	16	0.022
	0.0170	432	0.58	0.42	14	0.022
	0.0095	241	0.72	0.28	16	**0.008**

before in Figure 6.19, the collection efficiency at the low screen parameter (about less than 0.01) would have a low value in the case of the same Stokes number.

Finally, in Figure 6.23 a comparison of aerosol deposition process on the different screens is presented by Equation (6-14). There is a small difference in the collection characteristics between wire screens (electroformed-wire, woven-wire and welded-wire screens) and perforated-sheet screen. It can be explained on the nature of the manufacturing method.

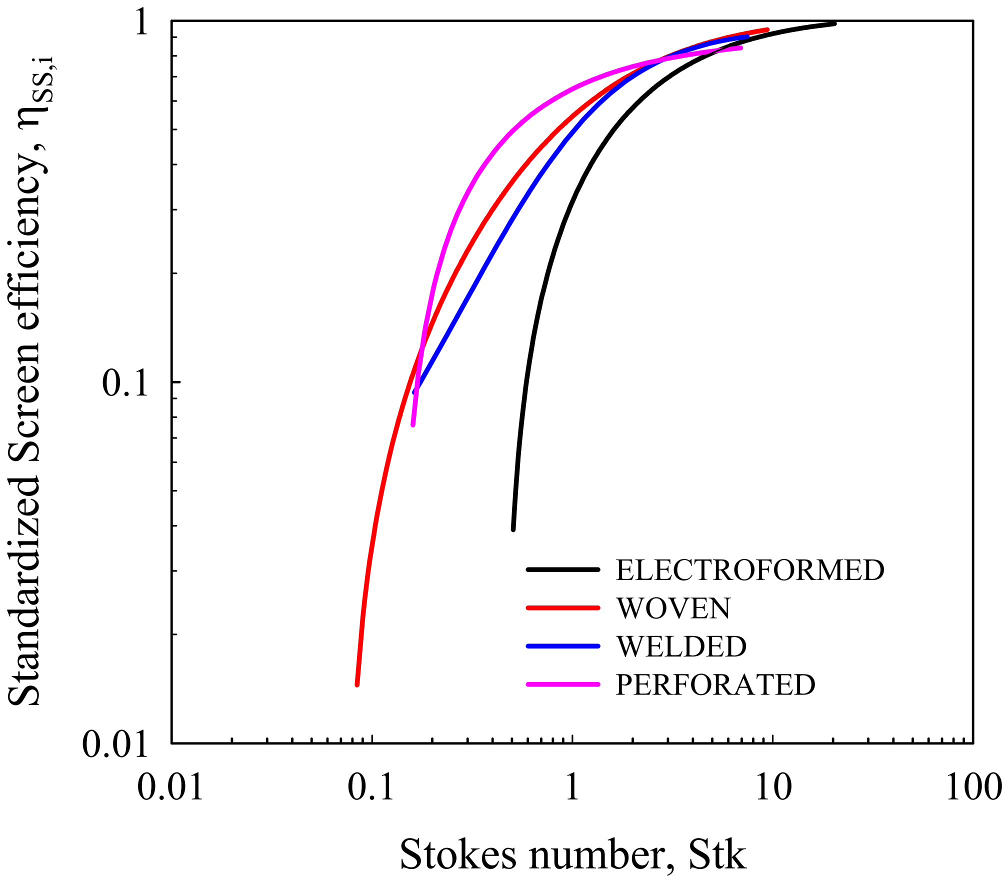

Figure 6.23. Comparison of standardized screen efficiency as a function of Stokes number. The solid curves are provided by Equation (6-14).

Comparison with Previous Studies

The focus of this section is to compare predictions obtained from mathematical models for the different screens developed in the current study to those of earlier researchers' models, obtained mostly for fibrous filters. The comparisons are made to put the results of the current research in proper perspective as even though there are physical differences between fibrous filters and screens, the single fiber (wire) approach was used for describing the physical mechanism of collection. Further, this effort would also serve to observe the discrepancies in the predictions obtained between the two models (wire and fiber).

The curve (black color) of ATL (Aerosol Technology Laboratory, TAMU) in Figure 6.24 represent our final expression (Equation 6-14), and the other curves are plotted based on our definition in terms of the standardized screen efficiency after applying for the total efficiency (Equation 2-3 in Chapter II), E, calculated based on the previous investigators' solution for the single fiber collection efficiency, η (Tables 2.1 to 2.3 in Chapter II) given below in Equations;

$$\eta_I = \frac{Stk^3}{Stk^3 + 0.77Stk^2 + 0.22} \quad \text{(Landahl \& Hermann, Theoretical, 1949)} \qquad (6\text{-}15)$$

$$\eta_{IR} = 0.16\left[R + (0.5 + 0.8R)Stk - 0.1052RStk^2\right] \quad \text{(Davies, Theoretical, 1952)} \qquad (6\text{-}16)$$

$$\eta_{IR} = \frac{1}{\left[1 + \frac{1.53 - 0.23\ln \mathrm{Re} + 0.0167(\ln \mathrm{Re})^2}{Stk}\right]^2} + \frac{2R}{3Stk} \quad \text{(Suneja \& Lee, Numerical, 1974)} \qquad (6\text{-}17)$$

$$\eta_I = \left(\frac{Stk}{Stk + 0.8} - \frac{2.56 - Log(Re) - 3.2R}{10\sqrt{Stk}}\right)(1 + R) \quad \text{(Schweers et al., Theoretical, 1994)} \qquad (6\text{-}18)$$

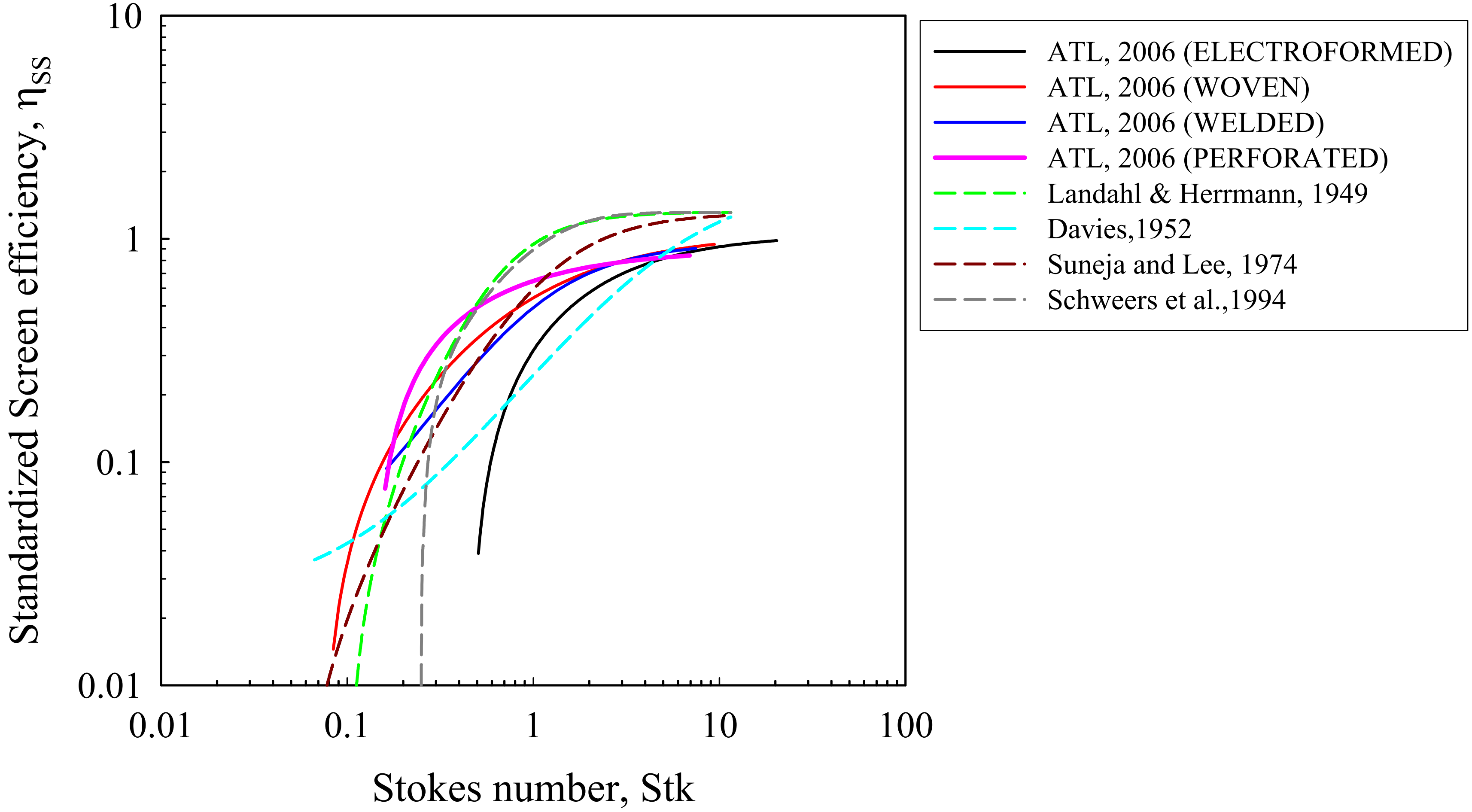

Figure 6.24. Comparison of standard screen efficiency for wire screens with those of the previous investigators' models ($Re_C = 0.5$ to 575).

The previous investigators' curves were also re-plotted by regression to achieve better comparison. It can be seen that the previous investigators' curves over-predict or under-predict the efficiency depending on the region of Stokes number. Results obtained for all the screen types (electroformed-wire, woven-wire, welded-wire screens, and perforate-sheet screen) are provided for comparison. These results suggest that the aerosol collection characteristic on different models is different and depends on the nature of the manufacturing process for a typical model (wire or fiber).

Pressure Coefficient Modeling

Numerical and experimental predictions of pressure drop across the wire screens (electroformed-wire and woven-wire screens), perforated-sheet screens at different flow conditions were used to calculate the pressure coefficient (C_p) for flow past the different screens (Figures 6.25 to 6.27).

$$Cp = \frac{\Delta P}{\frac{1}{2}\rho_a {U_O}^2} \tag{6-19}$$

Here, ΔP = pressure drop across screens; ρ_a = air density; U_o = face velocity.

At this point the purpose of a new definition for $Re_{C,f}$ is to compare with the Wakeland and Keolian model (2003). It can be seen that the relationship between the $Re_{C,f}$ and the pressure coefficient for each screen follows a correlation of the form $ARe_{C,f}^{-1}+B$, as shown by Wakeland and Keolian (2003), and can be expressed as

$$Cp = G_{f_{OA}} \times \left[\frac{A}{Re_{C,f}} + B \right],\ G_{f_{OA}} = f(f_{OA}),\ \mathrm{Re}_{C,f} = \frac{\rho_a U_o d_c}{\mu} \tag{6-20}$$

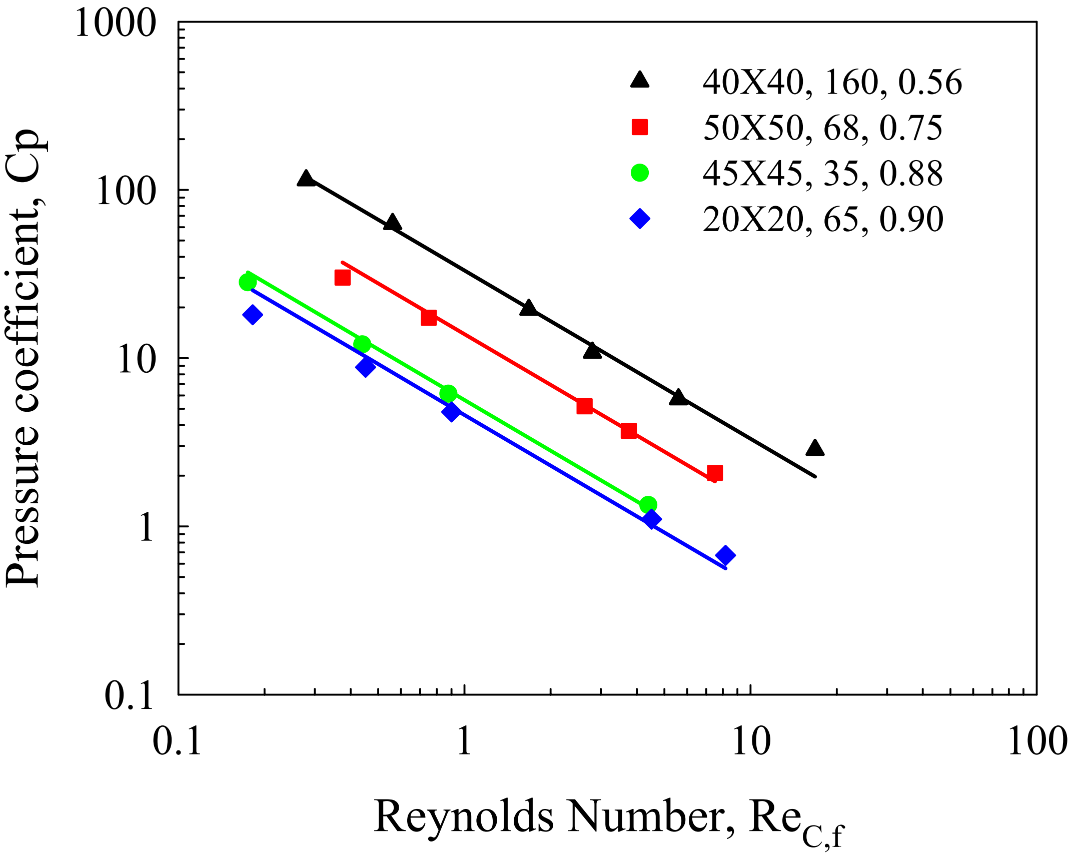

Figure 6.25. Pressure coefficient (*Cp*) as a function of wire Reynolds number ($Re_{C,f}$) for electroformed-wire screen, between 0.56 and 0.90 fraction of open areas.

Note: Symbols are numerical data and solid lines are plotted, based on the correlation Equation (6-20) and Table 6.7.

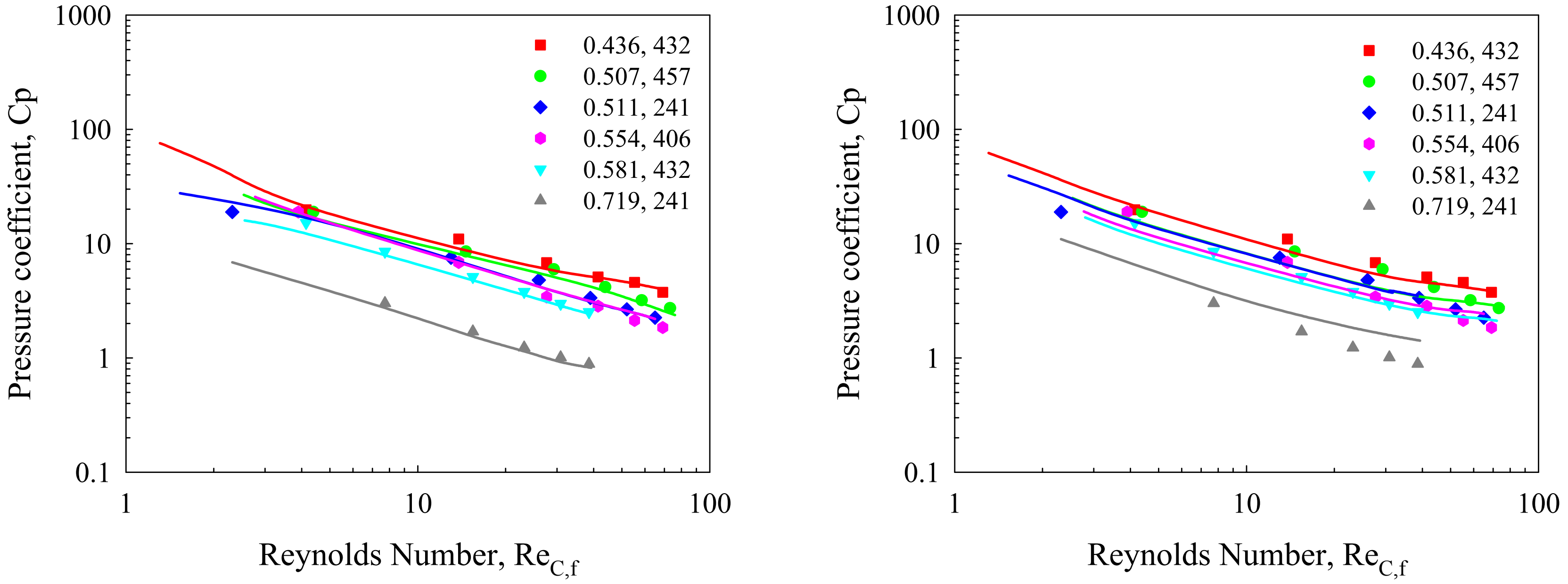

(a) Exp. vs. Num.

(b) Exp. vs. Correlation

Figure 6.26. Pressure coefficient (*Cp*) of experimental vs. numerical (a) and experimental vs. correlation (b) as a function of wire Reynolds number ($Re_{C,f}$) for woven-wire screen, between 0.436 and 0.719 fraction of open area.
Note: Symbols are numerical data and solid lines are plotted based on correlation Equation (6-20) and Table 6.7. Parameters in legend are fraction of open area and wire diameter (μm).

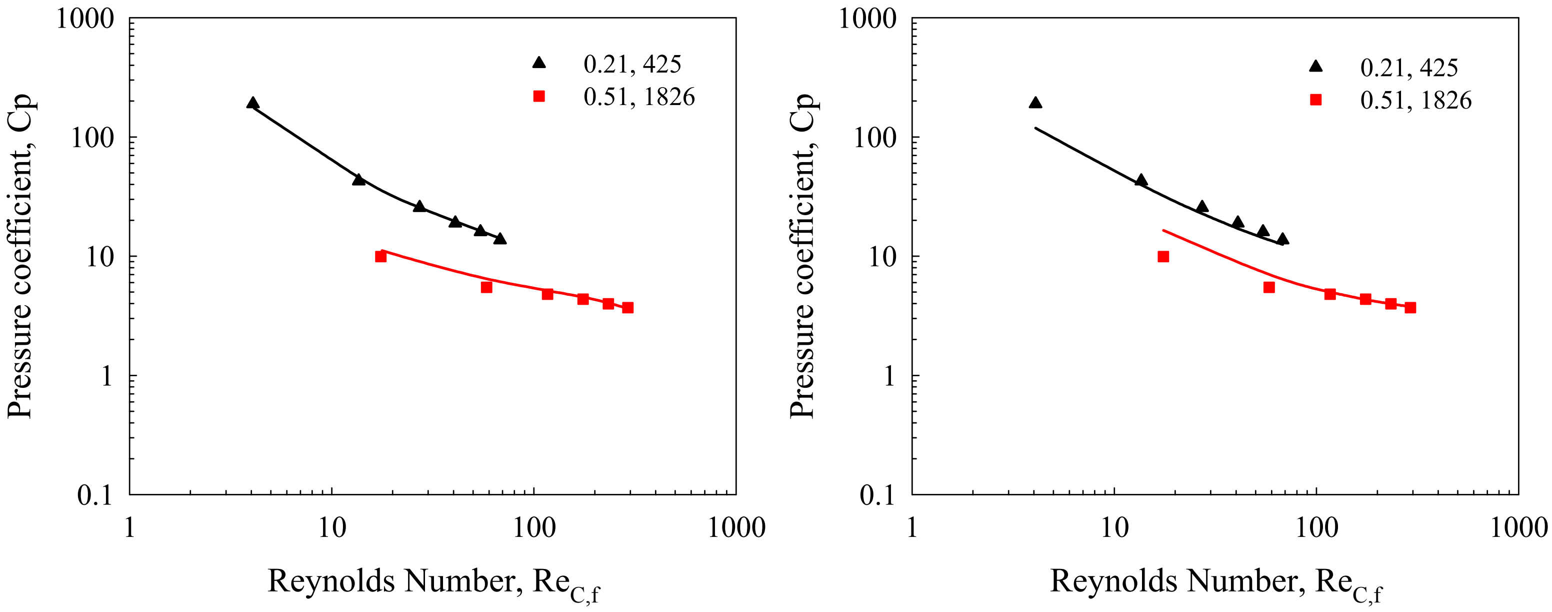

(a) Exp. vs. Num.

(b) Exp. vs. Correlation

Figure 6.27. Pressure coefficient (*Cp*) of experimental vs. numerical (a) and experimental vs. correlation (b) as a function of effective slack length Reynolds number ($Re_{C,f}$) for perforated-sheet screen, between 0.21 and 0.51 fraction of open area.

Note: Symbols are numerical data and solid lines are plotted based on correlation Equation (6-20) and Table 6.7. Parameters in legend are fraction of open area and wire diameter (μm).

where $G_{f_{OA}}$ is the correction factor. As shown in Equation (6-20), our data was seen to be best correlated using different $G_{f_{OA}}$ factor, $(1 \pm f_{OA})/f_{OA}$. With the correlating function $G_{f_{OA}}$, the different data collapse to a single curve that is presented in Figures 6.28 to 6.30 as a log-log plot of $Cp/G_{f_{OA}}$ versus $Re_{C,f}$, and compared with those of Wakeland and Keolian (2003). Table 6.7 summarizes the important deductions obtained from our study and compares the results to those of Wakeland and Keolian (2003). Figure 6.31 presents the comparison of $Cp/G_{f_{OA}}$ as a function of Reynolds number for the different screens (electroformed-wire, woven-wire, and perforated-sheet).

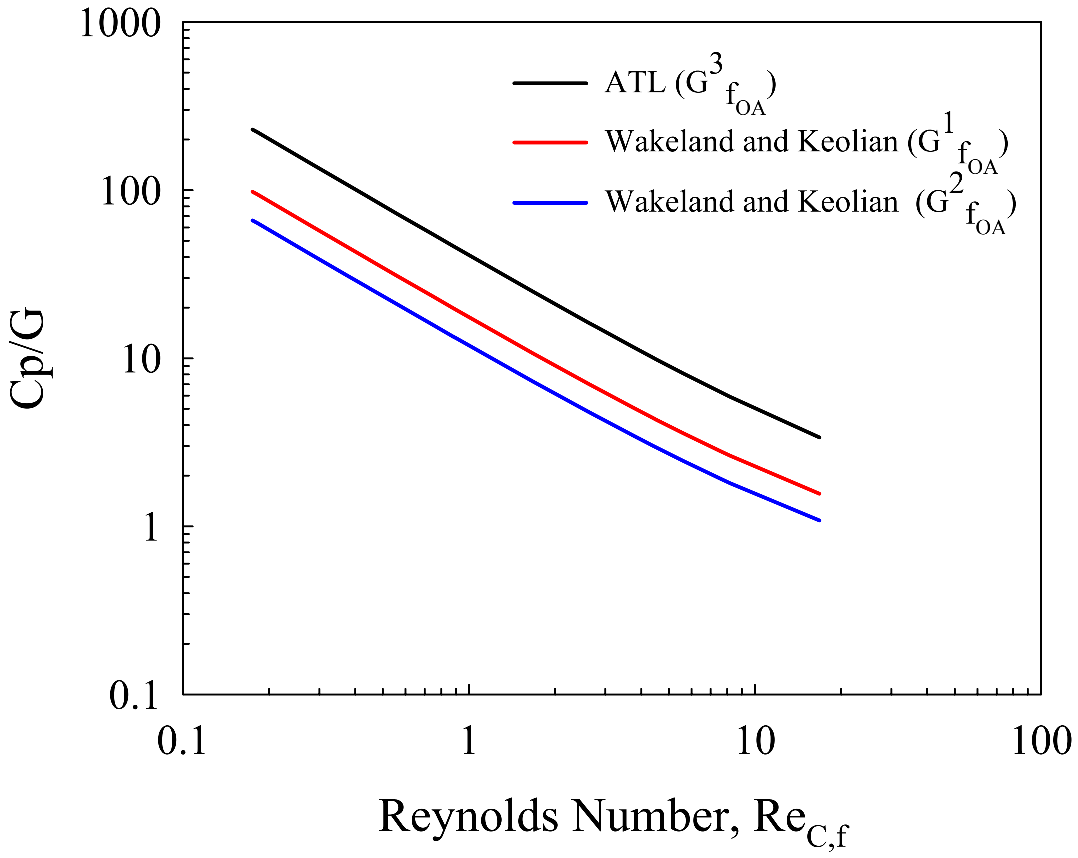

Figure 6.28. $Cp/G_{f_{OA}}$ as a function of wire Reynolds number ($Re_{C,f}$) for electroformed-wire screen, between 0.56 and 0.90 fraction of open area.

Note: Solid lines are plotted, based on correlation Equation (6-20) and Table 6.7.

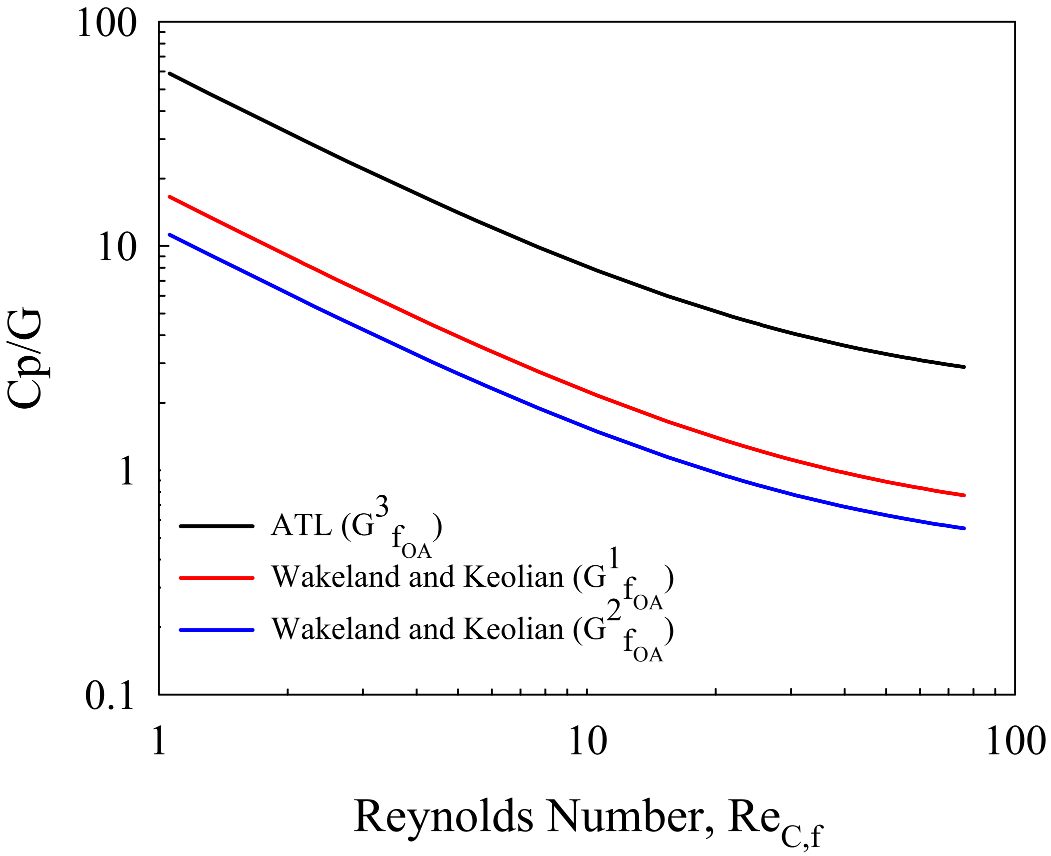

Figure 6.29. $Cp/G_{f_{OA}}$ as a function of wire Reynolds number ($Re_{C,f}$) for woven-wire screen, between 0.436 and 0.719 fraction of open area.
Note: Curves are plotted, based on correlation Equation (6-20) and Table 6.7.

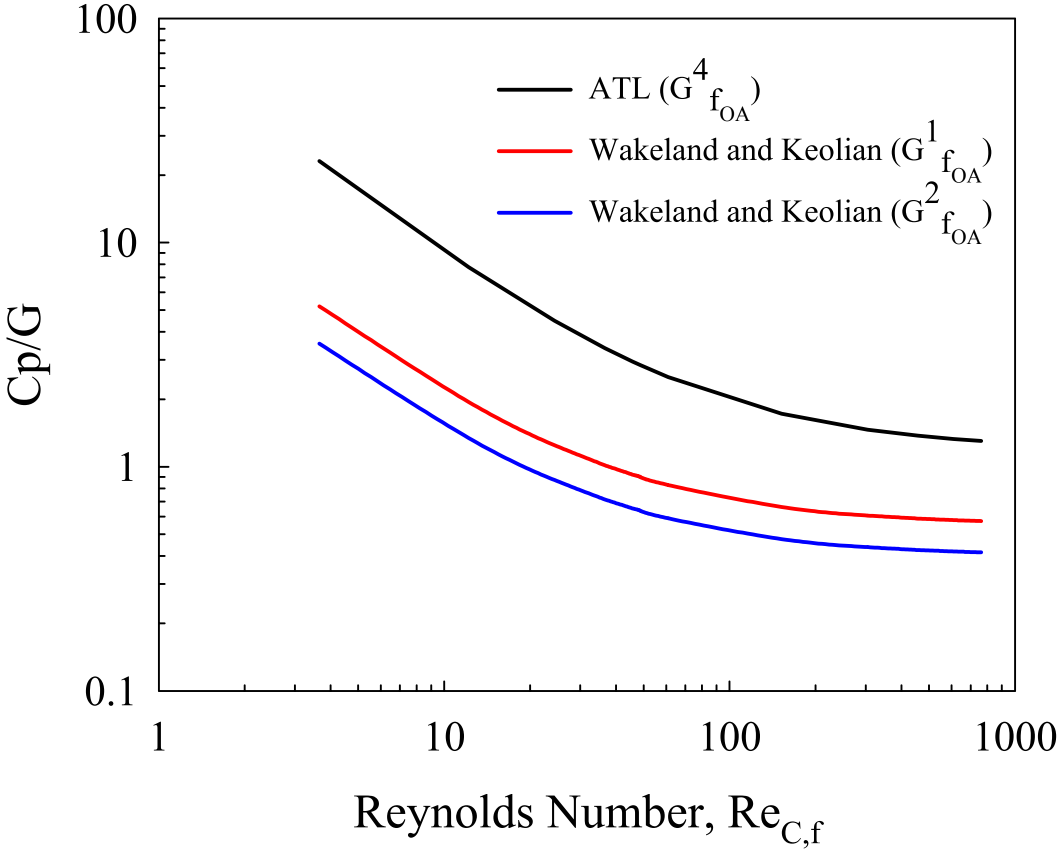

Figure 6.30. $Cp/G_{f_{OA}}$ as a function of effective slack length Reynolds number ($Re_{C,f}$) for perforated-sheet screen, between 0.21 and 0.51 fraction of open area.

Note: Curves are plotted, based on correlation Equation (6-20) and Table 6.7.

Table 6.7. Summary of the values of $G_{f_{OA}}$ (f_{OA}) and constants (A and B) for Wakeland and Keolian (2003). and our data (ATL: Aerosol Technology Laboratory at TAMU).

	$G_{f_{OA}}$	A	B	Ranges of $Re_{C,f}$	REMARKS
Wakeland and Keolian (2003)	$G^1_{f_{OA}} \equiv \frac{1-f_{OA}}{f_{OA}^2}$	17.0	0.55	$0.002 \leq Re_{C,f} \leq 400$	Oscillating Flow
	$G^2_{f_{OA}} \equiv \frac{1-f_{OA}^2}{f_{OA}^2}$	11.5	0.40		
ATL (2007)	$G^3_{f_{OA}} \equiv \frac{1-f_{OA}}{f_{OA}}$	40.0	1.00	$0.2 \leq Re_{C,f} \leq 20$ (Electroformed-wire)	Steady Flow
	$G^3_{f_{OA}} \equiv \frac{1-f_{OA}}{f_{OA}}$	60.0	2.10	$1.0 \leq Re_{C,f} \leq 90$ (Woven-wire)	
	$G^4_{f_{OA}} \equiv \frac{1+f_{OA}}{f_{OA}}$	70.0	1.00	$4.0 \leq Re_{C,f} \leq 300$ (perforated-sheet)	

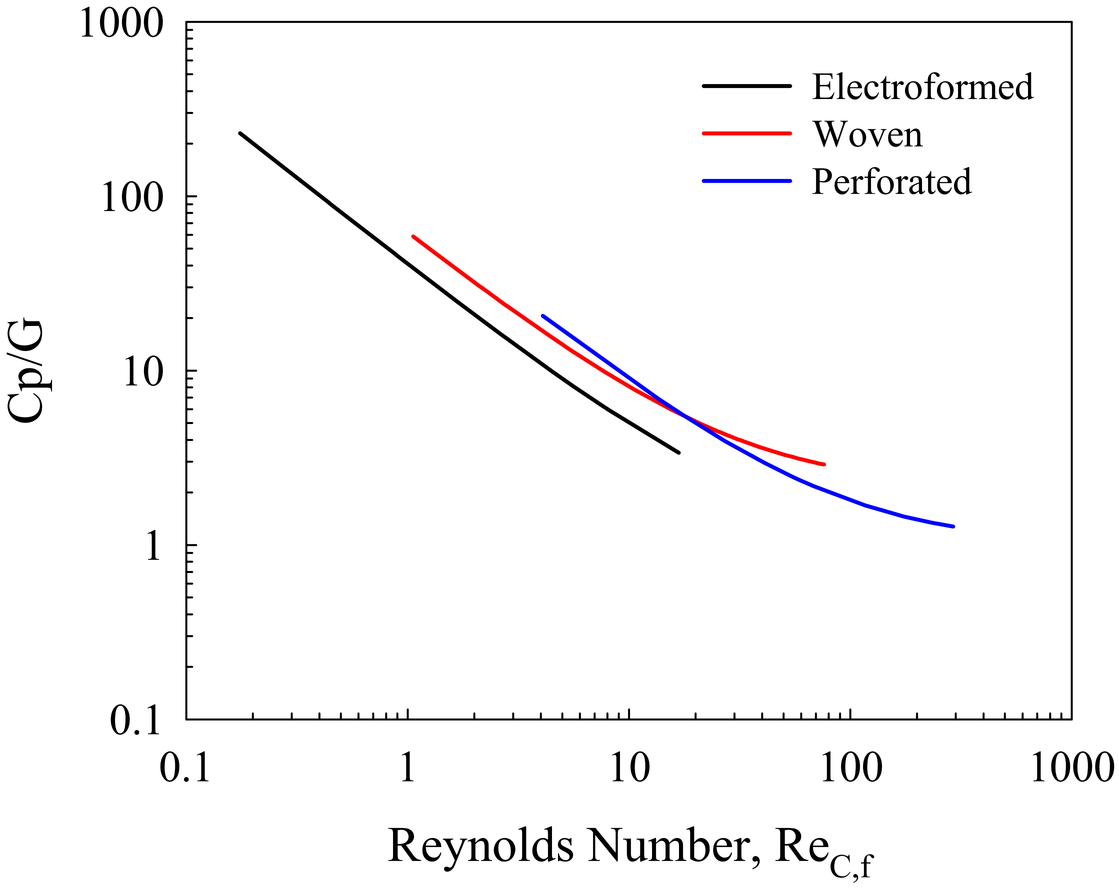

Figure 6.31. Comparison of $Cp/G_{f_{OA}}$ as a function of Reynolds number ($Re_{C,f}$) for all screens.

CHAPTER VII

APPLICATION TO THE PROBLEM OF AEROSOL COLLECTION ON A SCREEN

The principal objective of the present research was to develop correlations that would allow a *priori* estimation of the aerosol collection efficiency for flow past a screen. In this section, we provide a two-part demonstration of possible things that can be accomplished based on the results obtained from the above research.

Part 1: Validation of the developed procedure against experimental data

In the first part, we have considered conditions typical of experimental data obtained on the 20x20 mesh size screen. Starting from the initial conditions that characterized the above experiment, we work through the calculations in a step-wise manner to illustrate the methodology to compute the collection efficiency for one particle size.

STEP 0: Given Initial data: face velocity, mesh size, wire Diameter

U_o = 1.935 m/s, M = 45x45, d_w = 35 μm (0.00138-inch), d_p = 4.3 μm AD

STEP 1: Estimate the areal solidity (α_A) based on the above data as follows.

$$\alpha_A = 1 - f_{OA} = 1 - (1 - d_w \times \mathrm{M})^2 = 1 - (1 - 0.00138 \times 45)^2 = 0.12 \qquad (7\text{-}1)$$

STEP 2: Estimate the Stokes number, *Stk*, defined by Equation (2-4), provided the interested particle diameter (4.3 μm), air viscosity (0.0000185 kg/(m·s)) and the average velocity.

$$U = \frac{U_o}{(1-\alpha_A)} = \frac{1.935}{(1-0.12)} = 2.20 m/s \tag{7-2}$$

$$Stk = \frac{1.038 \times 1000 \times (4.3 \times 10^{-6})^2 \times 1.935}{18 \times 0.0000185 \times (0.00138 \times 0.0254)} = 3.182 \tag{7-3}$$

$$Re_w = \frac{2.2 \times (0.00138 \times 0.0254)}{0.000015416} = 5.0 \tag{7-4}$$

$$R = \frac{d_p}{d_w} = \frac{4.3}{35} = 0.12 \tag{7-5}$$

STEP 3: Estimate the standardize screen efficiency, $\eta_{SS,\mathrm{i}}$ defined by Equation (6-14) and Tables 6.3, 6.4, and 6.5 can be calculated,

$$\eta_{SS,i} = \left[-0.714 + \frac{1.777}{1 + 0.464 \times (\frac{1.828}{3.182})^{0.852}} \right] \times (1 + 0.123)^{0.1} \times (1 - \frac{0.03}{5.0^{0.01}}) = 0.652 \tag{7-6}$$

STEP 4: Estimate the actual collection efficiency on the screen.

$$\eta_A = \eta_{SS,i} \times \alpha_A = 0.684 \times 0.12 = 0.078 \tag{7-7}$$

We extend the above computation for other particle sizes and provided the results in Table 7-1. Figure 7-1 provides a comparison of the reconstructed efficiency curve to experimental data. It is seen from Figure 7-1 that the agreement to the experiment is excellent, validating the above procedure.

Table 7-1. Result of actual efficiency that was reconstructed based on the application to the case problem-A on a screen (M: 45×45, d_w: 35 μm, α_A: 0.12) and compared with experimental results.

	Correction factors			Correlation	Experiment
	(H)		$\eta_{SS,i}$	η_A	η_A
Stk	*Rew*	*R*		$\eta_{SS,i} \times H$	
0.63	1.0	0.122	0.109	0.013	0.021
1.34	0.5	0.254	0.389	0.047	0.055
1.88	3.0	0.122	0.500	0.060	0.064
2.46	0.5	0.345	0.591	0.071	0.074
2.67	1.0	0.254	0.611	0.074	0.077
3.14	5.0	0.122	0.648	0.078	0.085
3.97	0.5	0.439	0.724	0.087	0.087
4.44	0.5	0.465	0.751	0.090	0.092
4.91	1.0	0.345	0.766	0.092	0.090
6.41	0.5	0.559	0.830	0.100	0.099
7.94	1.0	0.439	0.860	0.103	0.101
8.02	3.0	0.254	0.850	0.102	0.103
8.89	1.0	0.465	0.879	0.106	0.108
12.83	1.0	0.559	0.932	0.112	0.109
13.37	5.0	0.254	0.917	0.110	0.111
14.76	3.0	0.345	0.934	0.112	0.111

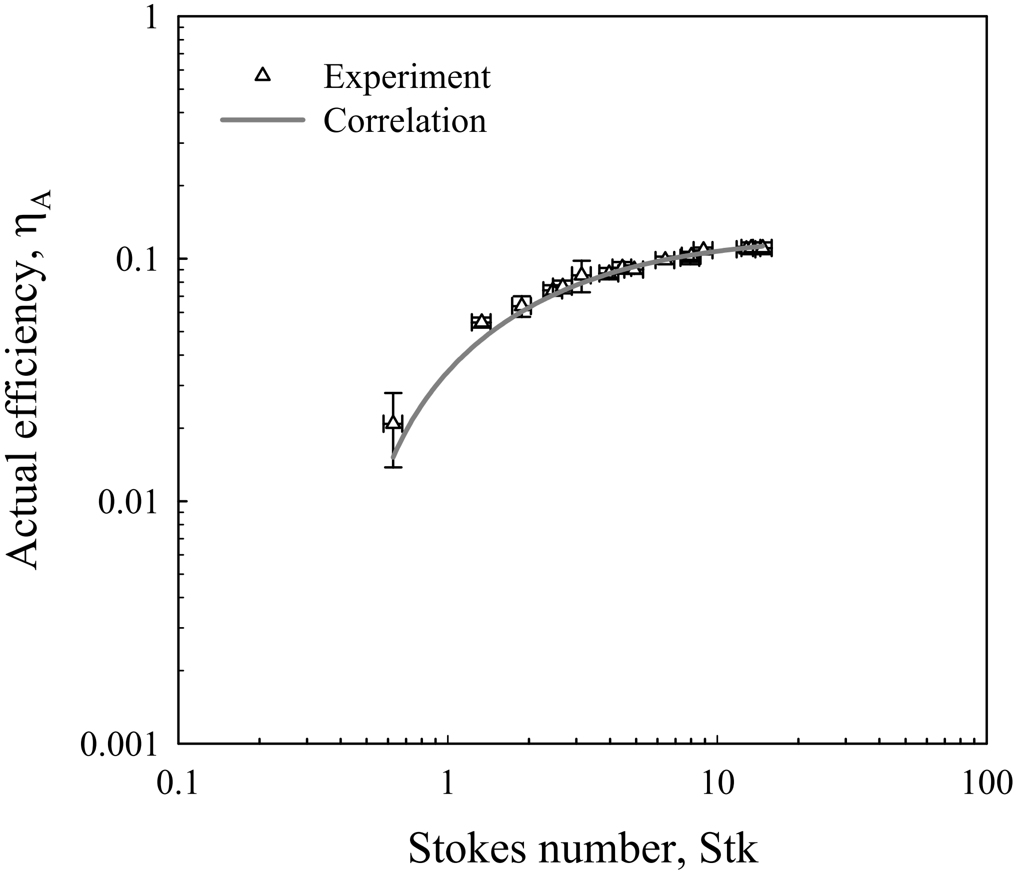

Figure 7-1. Comparison of the collection efficiency curves as a function of Stokes number reconstructed based on the developed procedure to experimental data.
Screen (M: 45×45, d_w: 35 µm, α_A: 0.12).

Part 2: Use of the developed procedure to generate collection efficiency data for intermediate screen sizes

We had presented the collection efficiency curves obtained on four different screens with areal solidity values (0.1, 0.12, 0.25, and 0.44) in Figure 6-13. While the first two were experimental results, the next two were generated from the validated numerical procedure. In this section, we consider a couple of screens with solidity values in the intermediate range, say 0.68 and 0.81 and generate the characteristic collection efficiency curve for a typical flow condition. For example, consider that the desired flow rate for 0.089 m (3.5-inch) diameter of test section is 1250 L/min (0.02083 m^3/s) and choose a commercially available screen of mesh size (M) 34×34 and wire diameter (d_w) of 131.8 μm (0.00519-inch) (values that are normally provided by the manufacturer).

STEP 0: Given Initial data: Flow rate, mesh size, wire Diameter

Q = 1250 L/min (0.02083 m^3/s), M = 34×34, d_w = 131.8 μm (0.00519-inch), d_p = 10 μm AD

$$U_o = \frac{Q}{A} = \frac{0.02083}{\frac{\pi \times (0.089)^2}{4}} = 3.348 m/s \tag{7-8}$$

STEP 1: Estimate the areal solidity (α_A) based on the above data as follows.

$$\alpha_A = 1 - (1 - 0.00519 \times 34)^2 = 0.3217 \tag{7-9}$$

STEP 2: Estimate the Stokes number, *Stk*, defined by Equation (2-4), provided the interested particle diameter (10 μm), air viscosity (0.0000185 kg/(m·s)) and the average velocity.

$$U = \frac{U_o}{(1 - \alpha_A)} = \frac{3.36}{(1 - 0.3217)} = 4.95 m/s \tag{7-10}$$

$$Stk = \frac{1.016 \times 1000 \times (10 \times 10^{-6})^2 \times 3.348}{18 \times 0.0000185 \times (0.00519 \times 0.0254)} = 7.749 \tag{7-11}$$

$$Re_w = \frac{4.936 \times (0.00519 \times 0.0254)}{0.000015416} = 42.21 \tag{7-12}$$

$$R = \frac{10}{131.8} = 0.076 \tag{7-13}$$

STEP 3: Estimate the standardize screen efficiency, η_{SS}, defined by Equation (6-14) and Tables 6.3, 6.4, and 6.5 can be calculated,

$$\eta_{SS} = \left[-0.714 + \frac{1.777}{1 + 0.464 \times (\frac{1.828}{7.749})^{0.852}} \right] \times (1 + 0.076)^{0.1} \times (1 - \frac{0.03}{42.21^{0.01}}) = 0.833 \quad (7\text{-}14)$$

STEP 4: Estimate the actual collection efficiency on the screen.

$$\eta_A = 0.833 \times 0.3217 = 0.268 \quad (7\text{-}15)$$

In Table 7-2, we have provided additional calculations that present the collection efficiency value for different sized particles, estimated from the above procedure. In Figure 7-2, we have included curves for the intermediate areal solidity values (0.68 and 0.81) generated based on the developed procedure for the two screens (M: 34×34, d_w: 132 µm, f_{OA}: 0.68 and M: 36×36, d_w: 71 µm, f_{OA}: 0.81), along with the curves presented in Figure 3.

As observed previously, it can be seen from Figure 7-2 that the new curves indicate exactly similar collection trends, are spaced proportionally apart from their neighbors, and asymptotically approach a maximum efficiency value that is equal to their areal solidity. The above result again is physically and intuitively appealing and demonstrates the soundness of the developed procedure.

Table 7-2. Additional calculations that present the collection efficiency value for different sized particles estimated from the application to the problem on a screen (M: 34×34, d_w: 132 μm, f_{OA}: 0.68).

d_p			Correction factors		$\eta_{SS,i}$	η_A
(AD)			(H)			$\eta_{SS,i} \times H$
μm	C_c	Stk	Rew	R		
3	1.054	0.7	42.3	0.023	0.161	0.052
5	1.033	2.0	42.3	0.038	0.511	0.165
7	1.023	3.8	42.3	0.053	0.694	0.223
10	1.016	7.8	42.3	0.076	0.833	0.268
16	1.010	19.8	42.3	0.121	0.944	0.304

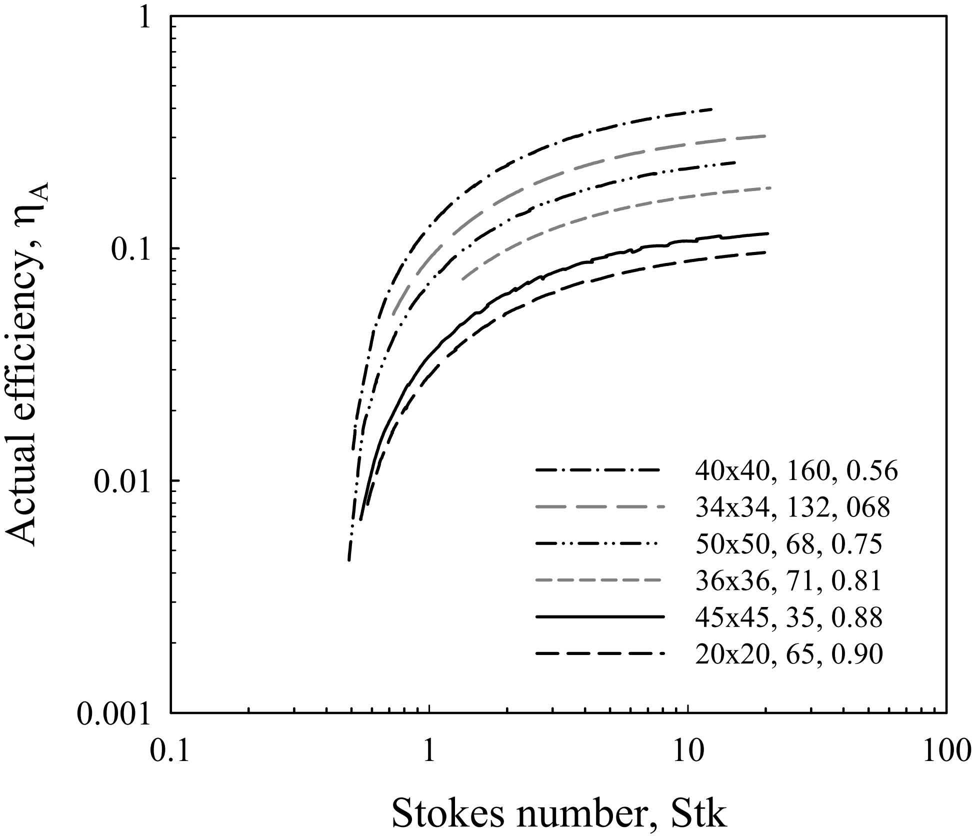

Figure 7-2. Comparison of collection efficiency curves presented in Fig. 6-13 to the new curves reconstructed based on the developed procedure for screens with intermediate solidity values.

Screens (M: 34×34, d_w: 132 μm, f_{OA}: 0.68 and M: 36×36, d_w: 71 μm, f_{OA}: 0.81).

CHAPTER VIII

CONCLUSIONS AND FUTURE WORK

The primary objectives of this study were to carry out experimental studies using commercially available screens (electroformed-wire, woven-wire, welded-wire, and perforated-sheet) planned to be used as filter media in sampling inlet applications, to characterize the aerosol deposition process of liquid aerosols. Three-dimensional numerical simulations were simultaneously performed to assess the capability of computational fluid dynamics as a predictive tool for the above application. It is seen that numerical predictions of the aerosol deposition process are in very good agreement with experimental results over a wide range of wire Reynolds numbers ($0.5 < Re_C < 575$), and Stokes numbers ($0.08 < Stk < 20$). This chapter summarizes the important conclusions that may be drawn based on the results of the present work.

1. The experimental approach used for this screen study was useful for evaluating collection efficiency. This approach enables the user to get easily get data for a wide range of conditions.
2. Results of the measurements of both approaches indicate a relationship between actual efficiency (η_A) and parameters (area solidity and Stokes number) on the range of Stokes numbers ($0.08< Stk <20$) and the areal solidity ($0.1< \alpha_A <0.79$).
3. Many factors influence the screen collection efficiency; however, geometrical factors (area solidity and characteristic length) and other

factors related to flow conditions (Reynolds numbers and Stokes number), on the screen played an important role.

4. There was a correction factor (*H*) to standardize all actual efficiencies for each screen. Non-dimensional parameters (*R* and Re_C) that standardize the collection efficiency on a particular screen were identified and used to evolve a new parameter known as standardized screen efficiency (η_{SS}) that collapses collection characteristics of different wire screens to a unique correlation.
5. A mathematical model was developed to express the standardized screen efficiency ($\eta_{SS,i}$) on different screens as a function of the Stokes number with correction factors.
6. Our correlation model for wire screens was compared to the standardized screen efficiency with the earlier researcher's model.
7. Finally, it was seen the pressure coefficient for flow across the screen can be expressed as a function of the Reynolds number and the fraction of open area (f_{OA}). Correlations expressing the actual relationships were evolved.
8. Additionally, a model was developed to relate pressure coefficient (*Cp*) in terms of correction factor ($G_{f_{OA}}$) and Reynolds number ($Re_{C,f}$).

Recommendations for Future Works

Aerosol penetration through screens has been widely encountered and has a variety of applications in the filtration and separation of liquid aerosol particles. In order further our understanding of this research area, the following recommendations are made for future work.

1. Most of the studies that were performed for conditions where the flow is perpendicular to the screen. It would be useful if new studies in which the flow is inclined ($0< \theta <90$) to the screen face are performed.
2. Additional work should be performed using solid aerosol particles. In particular, it would be helpful to understand the experimental methodology, the extent of loading that could be tolerated by the screen.
3. Further modeling work expanding upon the current correlations, supported by a more rigorous theoretical basis would be a nice contribution.

REFERENCES

Alonso, M., Alguacil, F.J., and Nomura, T. (2001). Turbulent deposition of aerosol nanoparticles on a wire screen. *Journal of Aerosol Science, 32*, 1359-1367.

American Society for Testing and Materials (2004a). Standard specification for precision electroformed sieves. ASTM Standard E-161-00. V 14.02.

American Society for Testing and Materials (2004b). Standard specification for wire cloth and sieves. ASTM Standard E-11-04. V 14.02.

American Society for Testing and Materials (2004c). Standard specification for perforated-plate sieves for testing purposes. ASTM Standard E-323-80. V 14.02.

Armour, J.C., and Cannon, J.N. (1968). Fluid flow through woven screens. *AICHE Journal*, 14/3, 415-420.

Baines, W.D., and Peterson, E.G. (1951). An investigation of flow through screens. *Transactions of the ASME*, *73*, 467-480.

Baron, Paul A. (1986). Calibration and use of the aerodynamic particle sizer (APS 3300), *Aerosol Science and Technology*, *5*, 55-67.

Berglund, R.N., and Liu, B.Y.H. (1973). Generation of monodisperse aerosol standards. *Environmental Science and Technology*, *7*, 147-153.

Capps, R.W. (1994). Properly specify wire-mesh mist eliminations. *Chemical Engineering Progress*, *90*, 49-55.

Chang, W.S. (1990). Porosity and effective thermal conductivity of wire screens. *ASME Journal of Heat Transfer*, *112*, 5-9

Cheng, Y.S. (1993). Willeke, K. and Baron, P.A. (Eds), *Aerosol measurement: principles, techniques, and applications*. New York:Van Nostrand Reinhold.

Cheng, Y.S., Yeh, H.C., and Brinsko, K.J. (1985). Use of wire screens as a fan model filter. *Aerosol Science and Technology*, *4*, 165-174.

Cheng, Y.S., and Yeh, H.C. (1980). Theory of a screen-type diffusion battery. *Journal of Aerosol Science, 11*, 313-320.

Cheng, Y.S., Yamada, Y., and Yeh, H.C. (1990). Diffusion deposition in model fibrous filters with intermediate porosity. *Aerosol Science and Technology*, *12*, 286-299.

Darcy, H. (1856). *Italiass Les Fontaines Publiques de la Ville de Dijon*. Paris. 647 p. & atlas. ("*The Public Fountains of the City of Dijon*". The famous Appendix - Note D appears here.")

Davies, C.N. (1952). The separation of airborne dust and particles. *Proceedings of the Institution of Mechanical Engineers*, London, 1B, 185-198.

Davies, C.N. (1973). *Air Filtration*. London: Academic Press.

Ehrhardt, G. (1983). Flow measurements for wire gauzes. *International Chemical Engineering*, *23*, 455-465.

Fluent, *FLUENT user's guide, Version 6.1.22*. Lebanon, NH: Fluent, Inc.

Friedlander, S.K. (1957). Mass and heat transfer to single spheres and cylinders at low Reynolds numbers. *AIChE Journal*, *3*, 43-48.

Fuchs, N.A. (1964). *The mechanics of aerosols*. Oxford: Pergamon Press.

Han, T., O'Neal, D., McFarland, A.R., Haglund, J. and Ortiz, C.A. (2005). Evaluation of mixing elements in an L-Shaped configuration for application to single point aerosol sampling in ducts. *HVAC&R Research Journal*, *11*, 657-672.

Happel, J. (1959). Viscous flow relative to arrays of cylinders. *AIChE Journal*, *5*, 174-177.

Hinds, W.C. (1998). *Aerosol technology: properties, behavior and measurements of airborne particles*, New York: Wiley.

Iberall, A.S. (1950). *Journal of Research National Bureau,* Standards, *45*, 938.

Kanaoka, C., Emi, H., and Aikura, T. (1978). Collection efficiency of aerosol by micro-perforated plates. *Journal of Aerosol Science, 10*, 29-41.

Kirsch, A.A., and Fuchs, N.A. (1968). Studies on fibrous aerosol filters. Diffusional deposition of aerosol in fibrous filters, *Annals of Occupational Hygiene*, *11*, 299-304.

Kline, S.J., and McClintock, F.A. (1953). Describing uncertainties in single sample experiments. *Mechanical Engineering*, *75*, 38.

Kuwabara, S. (1959). The forces experienced by or spheres in viscous flow at small Reynolds numbers. *Journal of the Physical Society of Japan*, *14*, 527-532.

Lamb, H. (1932). *Hydrodynamics*, New York: Dover.

Landahl, H.D., and Herrman, R.G. (1949). Sampling of liquid aerosols by wires, cylinders, and slides, and the efficiency of impaction of the droplets. *Journal of Colloid Science*, *4*, 103.

Langmuir, I. (1942). Report on smokes and filters. Part 4 of the collected works of Irving Langmuir. *10*, 394-436.

Laws, E.M., and Livesey, J.L. (1978). *Annual Review of Fluid Mechanics*, *10*, 247.

Lee, K.W., and Liu, B.Y.H. (1982). Experimental study of aerosol filtration by fibrous filters. *Aerosol Science and Technology*, *1*, 35-46.

Lee, K.W., and Ramamurthi, M. (1993). Filter collection. In K. Willeke and P.A. Baron (Eds) *Aerosol measurement: principles, techniques, and applications*, New York: Van Nostrand Reinhold.

Liu, B.Y.H., and Pui, D.Y.H. (1975). Efficiency of membrane and nuclepore filters for submicrometer aerosols. *Environmental Science Technology, 10*, 345.

Natanson, G.L. (1962). Influence of slip on the contact effect in capture of a microscopic aerosol particle by a cylinder from a gas stream. Kolloid Zh. *24*, 52; *Colloid Journal* USSR (English translation) *24*, 42-44.

Olan-Figueroa E., McFarland A.R., and Ortiz C.A. (1982). Flattening coefficients for dop and oleic-acid droplets deposited on treated glass slides. *American Industrial Hygiene Association Journal*, *43*, 395-399.

Patankar, S.V. (1980). *Numerical heat transfer and fluid flow*, Washington, Hemisphere Pub. Corp., New York, McGraw-Hill.

Scheibel, H.G., and Porstendorfer, J. (1984). Penetration measurements for tube and screen-type diffusion batteries in the ultrafine particle size range, *Journal of Aerosol Science, 15*, 673-687.

Schweers, E., Umhauer, H., and Loffler, F. (1994). Experimental investigation of particle collection on single fibers of different configurations. *Particle and Particle Systems Characterization*, *11*, 275-283.

Simon, T.W., and Seume, J.R. (1988). A survey of oscillating flow in stirling engine heat exchangers. NASA Contractor Report 182108.

Soar, R.K.H. (1991). Woven-wire cloth – Historical development and modern methods. *Wire Industry*. *58*, 197-199.

Stechkina, I.B., and Fuchs, N.A. (1966). Studies on fibrous aerosol filters-I. Calculation of diffusional deposition of aerosols in fibrous filters. *Annals of Occupational Hygiene*, *9*, 59-64.

Stechkina, I.B., Kirch, A.A., and Fuchs, N.A. (1969). Studies on fibrous aerosol filters-IV. Calculation of aerosol deposition in model filters in the range of maximum penetration. *Annals of Occupational Hygiene*, *12*, 1-8.

Suneja, S.K., and Lee, C.H. (1974). Aerosol filtration by fibrous filters at intermediate Reynolds number. *Atmospheric Environment*, *8*, 1081-1094.

Torgeson, W.K. (1964). The theoretical collection efficiency of fibrous filters due to the combined effects of inertia, diffusion, and interception. Paper No. J-1057, Applied Science Division, St. Paul, MN: Litton Systems, Inc.

Tomotika, S., and Aoi, T. (1951). *The Quarterly Journal of Mechanics and Applied Mathematics*, *4*, 404.

Wakeland R.S., and Keolian, R.M. (2003). Measurements of resistance of individual square-mesh screens to oscillating flow at low and intermediate Reynolds numbers. *Journal of Fluids Engineering*, *125*, 851-862.

Weighardt, K.E.G. (1953). On the resistance of screens. *The Aeronautical Quarterly*, *4*, 186-192.

Yarbrough, S.A., Flake, B.A., and Razani, A. (2004). Computational fluid dynamic modeling of pressure drop through wire, mesh screen regenerators. *Transactions of the Cryogenic Engineering Conference*, *49*, 1138-1145.

Yeh, H.C. (1972). A fundamental study of aerosol filtration by fibrous filters. Ph.D. Dissertation, Mechanical Engineering Department, University of Minnesota.

Yeh, H.C., and Liu, B.Y.H. (1974a). Aerosol filtration by fibrous filters-I. Theoretical. *Journal of Aerosol Science, 5*, 191-204.

Yeh, H.C., and Liu, B.Y.H. (1974b). Aerosol filtration by fibrous filters-II. Experimental. *Journal of Aerosol Science, 5*, 205-217.

APPENDIX-1

DEFINITION OF CHARACTERISTIC LENGTH FOR PERFORATED-SHEET SCREEN

In this section, methodology used to obtain an appropriate characteristic length for perforated-sheet screens is explained. Table A-1-1 presents the various possible definitions of characteristic length (CL) that can be conceived for perforated-sheet screens, computed based on the important geometrical features.

Table A-1-1. Estimation for the proper characteristic length on perforated-sheet screens.

Hole diameter	Fraction of Open Area	CS*	Characteristic Length			
			Group 1		Group 2	
			CL1	CL2**	CL3	CL4***
d_h	f_{OA}		d_h	$d_h/(\sqrt{f_{OA}})$	$C.S.\text{-}d_h$	$C.S.\text{-}0.95d_h$
inch		inch	inch	inch	inch	inch
0.0150	0.21	0.031	0.0150	0.033	0.0160	0.017
0.1875	0.51	0.250	0.1875	0.263	0.0625	0.072

*CS: Center-to-Center Spacing
**Kanaoka et al., (1978)
***Baines and Peterson, (1951)

The possible definitions can be organized into two groups, group 1 (CL1 and CL2) and group 2 (CL3 and CL4), based on either the open area or solid area. CL1 is defined by the hole diameter of perforated-sheet and CL2 is the length directly calculated by the fraction of open area. It was seen that collection efficiency curves plotted based on Stokes number estimates obtained using either definitions of the characteristic length adopted in group 1 were unphysical (Figure A-1-1 a, b). This result indicated that an alternative definition of the characteristic dimension needs to be evolved. This is the technical basis for the evolution of the definitions explored in group 2.

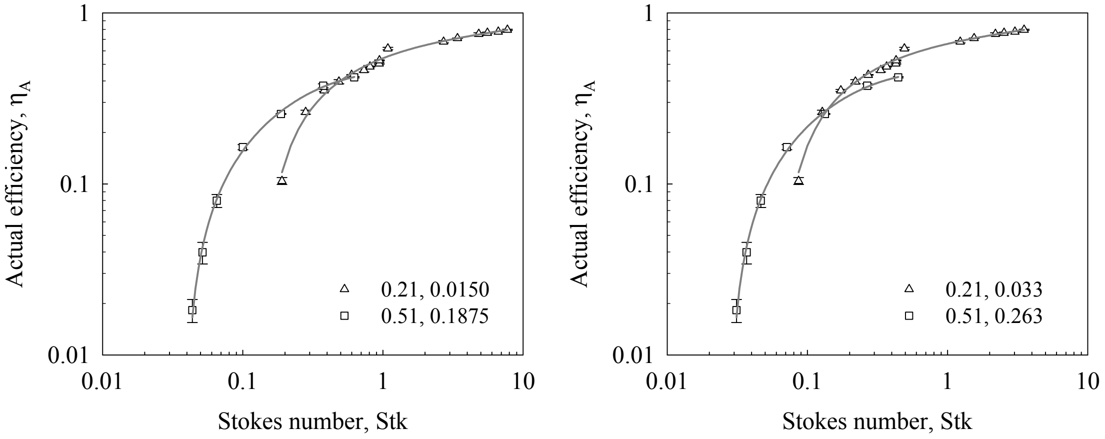

(a) CL1

(b) CL2

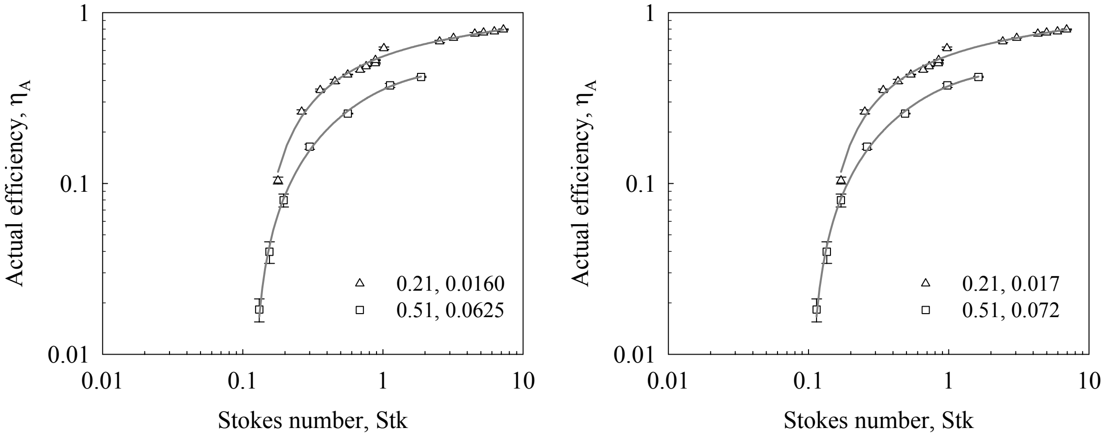

(C) CL3

(d) CL4

Figure A-1-1. Patterns of collection efficiency depended on characteristic length.

CL3, defined by CS-d_h is exactly the slack length between two holes. However, the slack length is not consistently uniform for the straight type of perforated sheet screen. Hence, a new definition of characteristic length, CL4, calculated on the basis of an imaginary wire screen corresponding to perforated-sheet, as illustrated in Figure A-1-2 was evolved. Based on the above definition, the general form of the equation for the characteristic length becomes

$$CL = CS - c \times d_h \tag{1}$$

Where the parameter, c, is a constant value estimated based on the actual geometrical parameters. Moreover, it can be seen from Figure A-1-1 (c and d) that efficiency curves plotted based on Stokes number estimates obtained based on group 2 definition of the

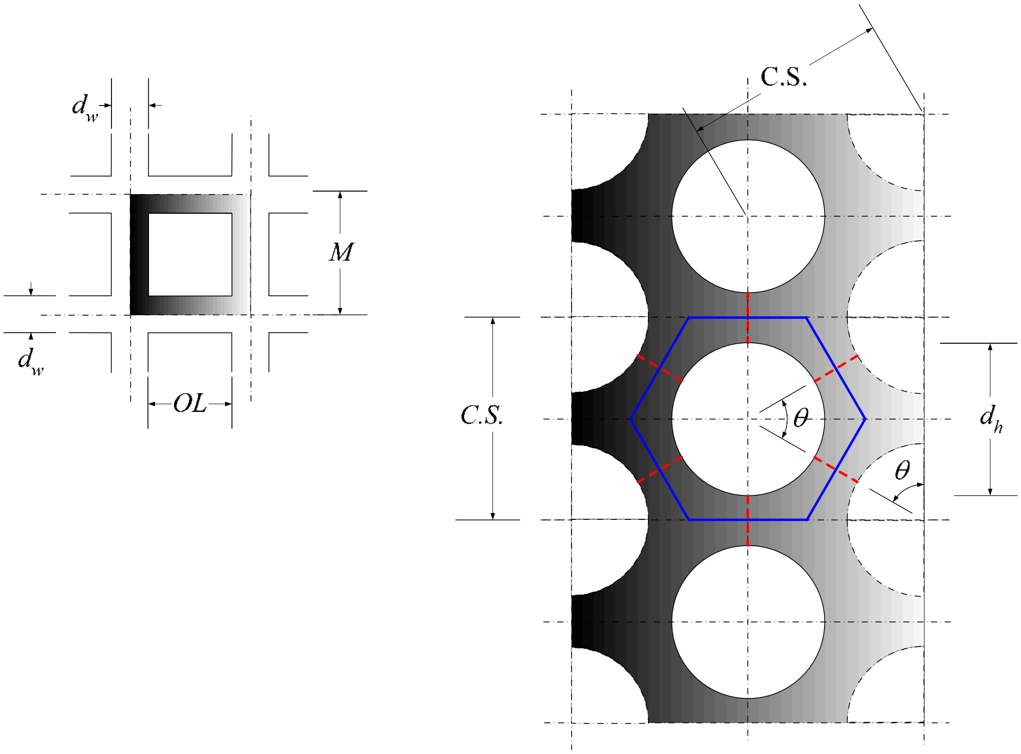

Figure A-1-2. Illustration for the calculation of characteristic length on perforated-sheet.

characteristic length is physically consistent. In the following demonstration, steps elaborating the detailed calculation method for the constant, accomplished based on Equation 3.1 is presented.

For example, consider that the two perforated-sheets, (a) fraction of open area of 0.21, and (b) fraction of open area of 0.51. Mesh size on perforated-sheets which refers to the number of openings per linear inch was used as the term, 1 over CS (Figure A-1-2). We work through the calculations to illustrate the methodology to compute the characteristic length.

STEP 0: Estimate the wire diameter (d_w) based on the initial data (fraction of open area and mesh size) as follows

$f_{OA} = (1 - d_w \times Mesh)^2$ defined by Equation (3.1)

(2)

(a) Given Initial data: fraction of open area (0.21), mesh size (1/0.031)

$$0.21 = (1 - d_w \times \frac{1}{0.031})^2 \tag{3}$$

$$\therefore d_w = 0.016794 \equiv CL \tag{4}$$

(b) Given Initial data: fraction of open area (0.51), mesh size (1/0.250)

$$0.51 = (1 - d_w \times \frac{1}{0.25})^2 \tag{5}$$

$$\therefore d_w = 0.071464 \equiv CL \tag{6}$$

STEP 1: Estimate a constant value, *c*, based on the above result as follows

$CL = CS - c \times d_h$ defined by Equation (4-6)

(a) Given above data in STEP 0 (a)

$$0.016794 = 0.031 - c \times 0.015 \tag{7}$$

$$\therefore c = 0.94706 \tag{8}$$

(b) Given above data in STEP 0 (b)

$$0.071464 = 0.25 - c \times 0.1875 \tag{9}$$

$$\therefore c = 0.95219 \tag{10}$$

The average of the results, (a) and (b)

$$c_{avg} = 0.95 \tag{11}$$

STEP 2: Define the final equation of characteristic length on perforated-sheet screen

$$CL = CS - 0.95 \times d_h \tag{12}$$

The characteristic length (Equation 12) is applied for perforated-sheet screen in this study. Additionally, the terms is defined as the effective slack length (l_{es}).

APPENDIX-2

TABLE OF CALCULATION OF COLLECTION EFFICIENCY ON A SCREEN

Table A-2-1 can be used as calculation table for actual efficiency (η_A) depended on screen types. If a certain Stokes number (*Stk*) is selected, standardized screen efficiency ($\eta_{SS,i}$) can be calculated provided correlation equation for each screen type and then unknown parameters (d_p, U_o, d_C, and α_A) will be obtained for correction factor (R and Re_C). Finally, actually efficiency can estimate.

Table A-2-1. Calculation table for standardized screen efficiency (η_{SS}) and actual efficiency (η_A) depended on screen types.

Screen Type	Standardized Screen Efficiency constants for $\eta_{SS,i}$†					Unknown parameters				Correction factor (H)			Actual efficiency η_A‡
						d_p (μm)	U_o (m/s)	d_C (μm)	Stk	$(1+R)^{\beta 1}$	$(1+\beta 2/Re_c^{\beta 3})$		
	x_0	x_1	x_2	x_3	Stk_{50}					$\beta 1$	$\beta 2$	$\beta 3$	
Electroformed	-0.71	1.78	0.46	0.85	1.83	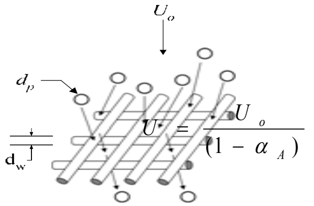				0.10	-0.03	0.01	
($0.1<\alpha_A<0.44$)	($0.5\le Stk\le 20$)									($0.025<R<0.57$)	($0.2<Re_c<30$)		
Woven	-0.09	1.16	0.96	0.96	0.91					0.10	-0.03	0.01	
($0.28<\alpha_A<0.56$)	($0.08\le Stk\le 12$)									($0.007<R<0.18$)	($1<Re_c<268$)		
Perforated	-0.90	1.86	0.33	0.91	0.48	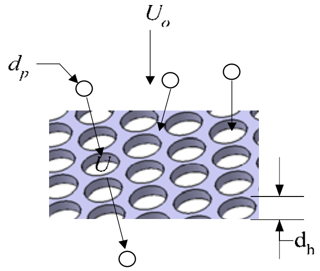				0.10	-0.03	0.01	
($0.49<\alpha_A<0.79$)	($0.15\le Stk\le 7$)									($0.003<R<0.047$)	($10<Re_c<575$)		

Note:

$$† \; \eta_{SS,i} = f(Stk)\times H = \left[x_o + \frac{x_1}{1+x_2\left(\frac{Stk_{50}}{Stk}\right)^{x_3}} \right] \times \left[(1+R)^{\beta 1} \times \left(1+\frac{\beta 2}{{Re_C}^{\beta 3}}\right) \right]$$

$$‡ \; \eta_A = \eta_{SS,i} \times \alpha_A$$

APPENDIX-3

SOFTWARE FOR THE DEPOSITION ON SCREENS

The screen deposition program v1.1 developed in Visual Studio has been modified based on the table of the calculation (Table A-2-1) for standardized screen and actual efficiencies (η_{SS} and η_A) depended on screen types. Figure A-3-1 is shown the captured figure of screen deposition software.

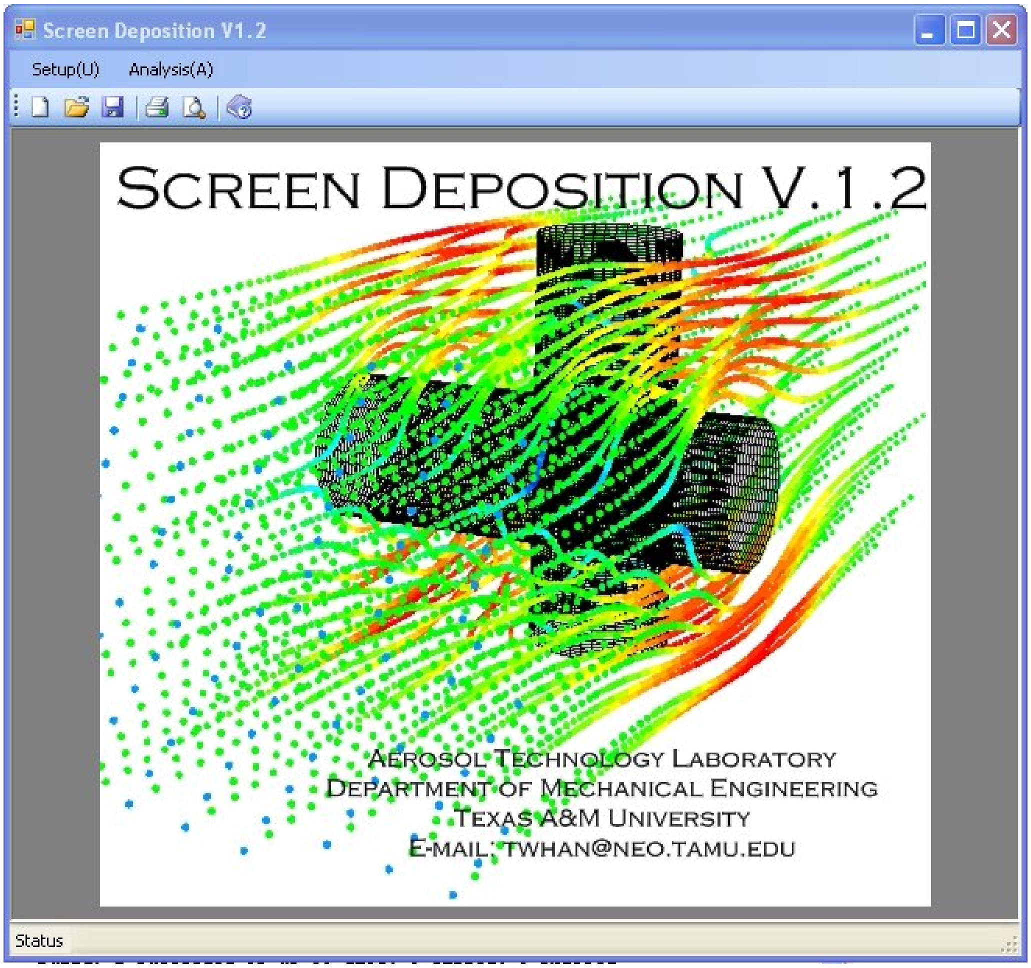

Figure A-3-1. A captured figure of screen deposition software.

VITA

Name: TAE WON HAN

Date & Place of Birth: October 5, 1970
Taegu, Korea.

Permanent Address: 1767-1 Shinam 4-Dong, Dong-gu,
Taegu, Korea, 701-014

Education: B.S., Mechanical Engineering (February 1997)
Keimyung University, Taegu, Korea

M.S., Mechanical Engineering (February 1999)
Keimyung University, Taegu, Korea

M.S., Mechanical Engineering (August 2003)
Texas A&M University, College Station, Texas

Ph.D., Mechanical Engineering (May 2007)
Texas A&M University, College Station, Texas